ENABLING INTEGRATED NANOPHOTONIC DEVICES IN HYBRID CMOS-COMPATIBLE MATERIAL PLATFORMS FOR OPTICAL INTERCONNECTION

A Dissertation
Presented to
The Academic Faculty

By

Majid Sodagar

In Partial Fulfillment
of the Requirements for the Degree
Doctor of Philosophy
in
Electrical and Computer Engineering

School of Electrical and Computer Engineering
Georgia Institute of Technology
August 2015

ENABLING INTEGRATED NANOPHOTONIC DEVICES IN HYBRID CMOS-COMPATIBLE MATERIAL PLATFORMS FOR OPTICAL INTERCONNECTION

Approved by:

Professor Ali Adibi, Advisor
School of Electrical and Computer Engineering
Georgia Institute of Technology

Professor Gee-Kung Chang
School of Electrical and Computer Engineering
Georgia Institute of Technology

Professor Stephen Ralph
School of Electrical and Computer Engineering
Georgia Institute of Technology

Professor Benjamin Klein
School of Electrical and Computer Engineering
Georgia Institute of Technology

Professor Joseph Perry
School of Chemistry and Biochemistry
Georgia Institute of Technology

Date Approved: 20 July 2015

To my parents:

Masoud and Zahra.

ACKNOWLEDGEMENTS

First and foremost I would like to thank my doctoral advisor, Prof. Ali Adibi, for giving me the opportunity to be part of the Photonic Research Group (PRG) at Georgia Tech, for his hospitable attitude toward his students, for his generous support and guidance over the course of my Ph.D., and finally for allowing me to pursue my ideas without restriction.

My special thanks goes to Prof. Stephen Ralph, who generously offered his knowledge, expertise, and time without which a key part of my work would not have been completed.

I wish to thank my reading committee, Prof. Stephen Ralph, Prof. Gee-Kung Chang, Prof. Benjamin Klein, and Prof. Joseph Perry for their dedication, time, and insightful guidance throughout the preparation of this dissertation.

In addition, I feel indebted to my senior colleagues, specially Dr. Reza Eftekhar, Dr. Ehsan Shahosseini, Dr. Amir Atabaki, Dr. Murtaza Askari, Dr. Payam Alipour, and Dr. Qing Li, who served as my mentors from the early stages of this journey. Their assistance brought me up to speed and enriched my insight.

I am profoundly grateful to many people who contributed to the progress of my research, including Reza Pourabolghasem, Mehdi Miri, Amir H. Hosseinnia, Pierre Isautier, and the IEN staff. My research endeavors would neither have been successful nor enjoyable without their constructive collaboration.

I appreciate the camaraderie of all of my friends in the PRG including Saeed Mohammadi, Maysam Chamanzar, Ali Behrooz, Farshid Ghasemi, Hossein Taheri, Razi Dehghannasiri, Ahmad Usman, Hossein Taghinejad, Mohammad Taghinejad, and Tianren Fan.

Last but not least, I would like to thank my family who invariably offered their sincere support, never-ending encouragement, and unconditional love. I shall always remain grateful to you for your kindness and care that have been beyond expectation in each and every stage of my life. Thank you.

TABLE OF CONTENTS

LIST OF TABLES

LIST OF FIGURES

SUMMARY

Recent impactful advances in integrated photonics undoubtedly owe much to silicon and its associated enabling platform (SOI). Although silicon has proved to be an indispensable element in many photonic systems yet it seems that it is not the ultimate solution to address all the challenges facing the photonics community. Therefore, integration of silicon with other optical materials featuring diverse properties is highly desirable. Such integration will be conducive to platforms which are naturally more capable and are suited for implementation of a wider range of optical devices and diverse functionalities. This dissertation is dedicated to design and implementation of integrated optical elements for hybrid material platforms. The basic theoretical foundation of integrated photonics is laid out in Chapter 2. In Chapter 3, an interlayer grating coupler for a specific hybrid material platform is designed, and demonstrated. Considering the fact that in almost all integrated photonic platforms, fabrication imperfections lead to an unpredictable shift in the wavelength of operation of individual devices, post fabrication tuning/trimming is inevitable. A number of widely used post fabrication trimming/tuning methods are briefly reviewed in Chapter 4 with special emphasis on a method based on electron beam exposure. In Chapter 5, an ultra-fast, low-power, and self-trimmable electro-optic modulator in demonstrated on a Si-based multilayer platform. Due to its remarkable optical and electronic properties, graphene has become a valuable material for opto-electronic applications. Integration of this novel 2D material with SOI platform is investigated in Chapter 6. Graphene-based electro-optic modulation through absorption and refractive-index change is successfully demonstrated using electrostatic gating mechanism. Chapter 7 is devoted to demonstration of a field-programmable 2 × 2 optical switch on a vertically stacked

Si/SiO$_2$/SOI platform. In Chapter 8, the peak-dragging phenomenon in a nanobeam photonic crystal cavity is studied. The optical bistability associated with this nonlinear phenomenon is of great interest for all-optical processing and sensing application. Future directions of this thesis are also discussed in the last Chapter.

CHAPTER I

INTRODUCTION

Advances in information technology (IT) and its consequent high growth rate in the generation of digital data have pushed for the emergence of new paradigms to store, process, and transfer large quantities of data in a cost-effective way. Over the past decade, IT has been struggling with issues such as resource availability, reliability, scalability, and cost. Concepts such as cloud computing, utility computing, and cloud storage have been introduced to address the abovementioned concerns. Recent adoption of such concepts, which are more than three decades old, has placed a good portion of data traffic and processing burden on the servers in data centers. As a matter of fact, the total data traffic within data centers was 1.9 Zettabyte in year 2012 and is predicted to reach to 5.8 Zettabyte in 2017 [1]. This data traffic volume comprises 76% of total data traffic (along with center-to-center and center-to-user data traffic) with a compound annual growth rate (CAGR) of 24% [1]. The past, present and predicted future growth trend of the data traffic for a six-year period are shown in Figure 1(a).This growth emphasizes the importance of short-reach (within data centers) interconnects for future development of the high-performance computing infrastructures.

Conventionally, electrical (mostly copper-based) interconnects have been deployed in long-, medium-, and short-reach links; benefiting from mature technology and consequent possibility of volume production in a rather cost-effective way. Nevertheless, this technology suffers from fundamental shortcomings. First, the power consumption and the delay of the electrical links increase with the length of the link. Although repeaters can be used to reduce the overall delay, this approach comes at the cost of an even more power consumption. Second problem with electrical interconnects is the signal integrity, which exists for all link length scales (mainly due to crosstalk through coupling capacitances). This issue can be dealt with pre- and post-emphasis circuits, which again requires extra power. Moreover, according to predictions provided by the international technology roadmap for semiconductors (ITRS) reports, the signal pin counts and bandwidth growth will be inadequate to keep up with the future communication needs [2].

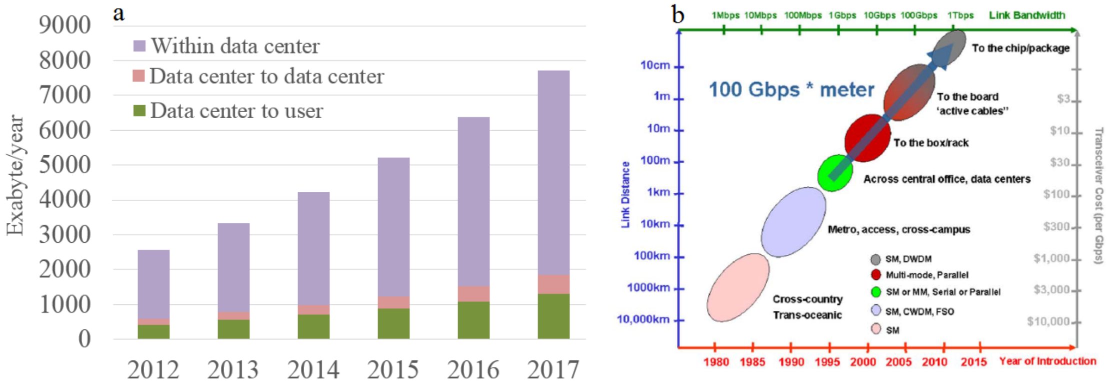

Figure 1: (a) Global data center traffic trend, data taken from [1]; (b) Historical trend for substitution of electrical links with optical interconnects over the past decades, image taken from [3].

In comparison, optical interconnects offer data transmission through channels (e.g., waveguides and fibers) with negligible propagation loss, and hence, most of the energy is consumed only at the transmitter/receiver terminals, where electrical-to-optical (E/O) and optical-to-electrical (O/E) conversions take place. Therefore, this technology can potentially provide length-independent power consumption solutions especially for length ranges less than 100 m. Besides, optical signals are relatively less prone to interference when compared with electrical signals. Also, optics in conjunction with wavelength-division multiplexing (WDM) technology offers immense bandwidth of operation that can be enhanced with the number of carrier wavelengths. However, optical interconnection technology still struggles with the manufacturing cost. Yet, driven by the notable advantages of optical interconnects over their electrical counterparts, we have witnessed a continual migration over time towards deployment of optical interconnects whenever such substitution was financially justified. This journey started by revamping transatlantic long-haul ($1000\ km - 10,000\ km$) communication cables in the mid 1980s and extended to cross-country and further across central office and data center links ($100\ m - 1\ km$) in the late 1990s. This 30-year-long trend in substitution of optical links suggests roughly an order of magnitude deeper penetration every five years [4]. This historic trend over time along with the associated cost and offered link bandwidth is shown in Figure 1(b). Following the same trend, advances in the photonics technology have resulted in the possible use of optical interconnections at all levels (e.g., board-to-board, chip-to-chip, and even on-chip) over the last decade.

For chip-to-chip and on-chip applications, optics can compete with electronics provided that the overall power consumption of the link remains low. The typical target values for power consumption are $2\ pJ/bit$ for communication from the core to a distant memory, $500\ fJ/bit$ for communication from the core to a short-distance memory (e.g., L3 cache), and ultimately $100\ fJ/bit$ for communication within the core [3]. Besides power consumption, a viable optical solution for chip-to-chip and on-chip interconnect should offer a high input/output (I/O) bandwidth density and a high integration yield with a cost as low as possible.

As mentioned earlier, the cost of optics has been high, i.e., $\approx$ \$1/Giga bit per second (*Gbps*), mostly due to its smaller market size and should be brought down (less than 10/*Gbps*) to be comparable with electronics. Capacitive proximity communication enables electronics to reach a potential bandwidth density of more than $1.25\ Pbps/cm^2$ (assuming an electrical pad pitch of $\approx 20\ \mu m$ and signal rates of $\approx 2.5 - 5$ *Gbps* per line [5]). An aggregate bandwidth density of $43\ Tbps/cm^2$ (with a power efficiency of 3.6 pJ/bit) is already demonstrated for chip-to-chip communication using the electrical proximity communication technology [6]. In comparison, adopting a similar approach in integrated optics in conjunction with WDM (assuming eight channels in a coarse WDM arrangement each at 12.5 $Gbps$ signaling rate) predicts an order of magnitude higher bandwidth density, amounting to more than 11 $Pbps/cm^2$, given that a typical optical coupler can have a footprint of smaller than 30 μm on each side.

Among various material platforms available for integrated optics (i.e., silica-on-silicon, silicon-on-insulator (SOI), lithium niobate, TriPlex, III-V materials, and polymers), SOI has become the center of attention for a number of different reasons. First of all, this material platform is cheap and allows for keeping the total direct material cost low. Also, the SOI platform permits the use of the existing complementary metal-oxide-semiconductor (CMOS) technology for the fabrication of photonic devices. Thanks to the maturity of the integrated circuit technology, CMOS compatibility significantly reduces the overall manufacturing cost. Furthermore, silicon (Si) is transparent over almost the entire optical telecommunication wavelength band ($1300\ nm - 1600\ nm$) and offers a high refractive index contrast ($n_{Si} \approx 3.48$) with respect to its surrounding material (usually silicon oxide (SiO_2) with $n \approx 1.45$ or air with $n = 1$). This property enables tight confinement of light, which in turn leads to the realization of ultra-compact photonic devices, reduced crosstalk and interference, and ultimately high integration densities. However, this very property renders Si-based photonic devices more vulnerable to fabrication imperfections (e.g., sidewall roughness). Moreover, Si exhibits a decent free-carrier dispersion, which is desirable for the realization of high-speed active optical devices.

Although Si has proven to be an indispensable element in many photonic systems, it is not the ultimate solution for all the challenges facing today's photonics industry due to its intrinsic shortcomings. For example, implementation of active functionalities such as lasing and detection in crystalline Si is difficult owing to its inherent indirect bandgap. Moreover, in contrast to silicon nitride (SiN), silicon carbide (SiC), and SiO_2; Si behaves nonlinearly once exposed to high intensity optical fields both due to the two-photon absorption process and its comparatively large third-order nonlinear optical coefficient (χ^3) [7, 8].

In addition, although Si has a rather large Kerr nonlinear coefficient ($n_2 \approx 3 \times 10^{-18}\ m^2/W$ [7, 8]) compared to higher bandgap materials (e.g., SiN with $n_2 \approx 2.4 \times 10^{-19}\ m^2/W$ [9], and SiO_2 with $n_2 \approx 2.5 \times 10^{-20}\ m^2/W$ [10]), it suffers from higher loss due to two-photon absorption ($\beta_{TPA} = 5{\times}10^{-12}\ m/W$) and free-carrier loss as compared to other CMOS-compatible materials such as SiN and SiO_2. This poor nonlinear figure of merit ($NFOM = n_2/(\lambda\beta_{TPA}) \approx 0.37$) in telecommunications band makes Si less appealing for certain nonlinear applications such as comb generation and high-speed all-optical processing. Due to these shortcomings, the best reported propagation loss in Si waveguides ($\approx 10\ dB/m$ [11, 12]) is an order of magnitude higher than that of SiN waveguides ($\approx 0.1 - 2\ dB/m$ [13]), and the best reported resonator quality factor (Q) achieved in planar Si platforms is an order of magnitude lower than that in SiN platforms($\approx 3 \times 10^6$ compared to $\approx 3 \times 10^7$, respectively) [12, 14] for similar microresonators.

One common approach to mitigate these shortcomings is to coherently integrate Si with other materials. In this thesis, I will partly focus on the development of photonic devices suited for high-speed optical communication applications on planar hybrid material platforms. The 3D schematic of my envisioned structure for realization of a broadband modulator for chip-to-chip and on-chip optical interconnects is shown in Figure 2. The structure can be fabricated on a hybrid material platform comprising a multilayer stack of SiN, SiO_2, and Si.

The rationale behind using such a hybrid platform is to from a semi-ideal material

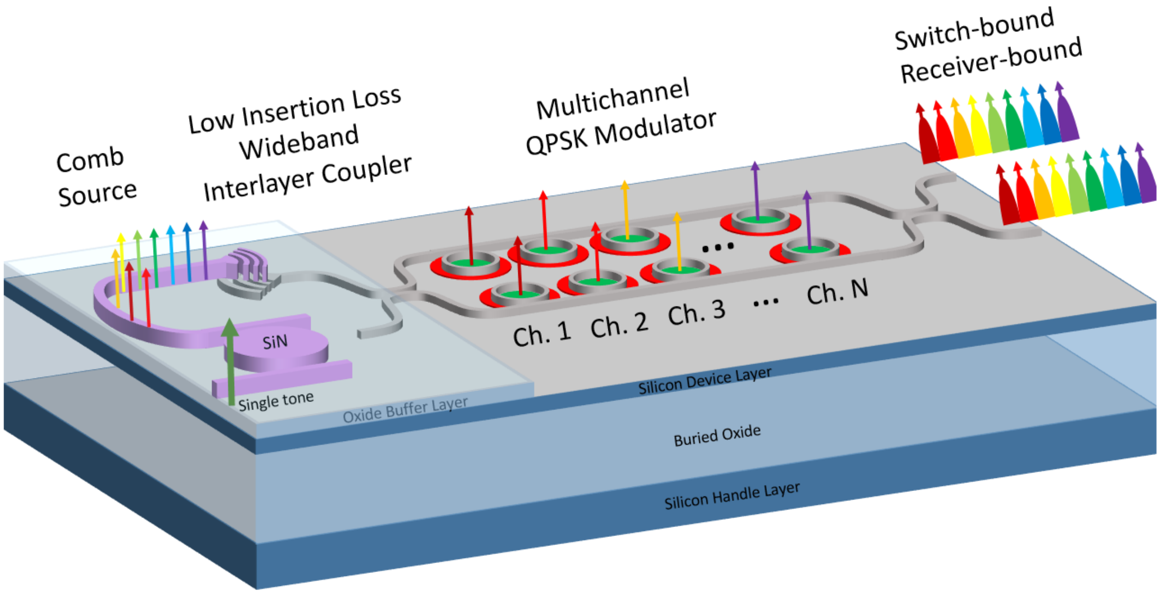

Figure 2: The envisioned architecture for a multichannel optical transmitter.

system for many desired optical functionalities by combining the unique features of each material (e.g., low loss of SiN and tunability of Si) while avoiding their respective shortcomings. In the proposed structure shown in Figure 2, an optical comb signal is generated in a high-Q resonator in the SiN layer once excited with a pump laser light via an adjacent waveguide. The possibility of optical comb generation in SiN microrings through the four-wave-mixing mechanism is already demonstrated in [15]. The multi-wavelength optical signal (i.e., the comb pulse train) is evanescently coupled to the drop waveguide on the SiN layer. Then the comb signal is diffractively coupled to the Si layer via an interlayer grating coupler. On the Si layer, each carrier wavelength is modulated separately by an appropriate electrical signal in a multi-channel electro-optic modulator structure. The resulting broadband signal is then directed through the switches and routers toward their intended destinations. The modulation can rely on the free-carrier dispersion effect in Si or alternatively can be achieved by taking advantage of other novel materials such as graphene or electro-optic polymers.

CHAPTER II

THEORETICAL FOUNDATION

2.1 Classical Electrodynamics

The goal of this section is to briefly introduce the background physics and mathematics used throughout this thesis required for accurate study of the behavior of simple building blocks of integrated photonic circuits, e.g., waveguides, resonators (also known as cavities), couplers, and etc. In general, Maxwell's equations provide an accurate mathematical tool to study the generation and propagation properties of electromagnetic (EM) waves in arbitrary media. Nearly all integrated photonic devices operate in rather low-energy radiation regimes, e.g., infra-red (IR) region ($\lambda \in [700\ nm, 100\ \mu m]$), visible region ($\lambda \in [400\ nm, 700\ nm]$), and occasionally in ultraviolet (UV) region ($\lambda \in [10\ nm, 380\ nm]$) of the electromagnetic spectrum. In such cases, the wavelength of operation is invariably much greater than atomic spacing of the optical medium (for solids and liquids atomic distances are around ≈ 2–3 Å and for gases are around ≈ 20-30 Å). Also in almost all occasions the basic operation of photonic devices relies on macroscopic observables (i.e., quantities averaged over length scales much longer than atomic distances) and the details of the EM field variations are generally irrelevant. The net effect of all small-scale EM sources (i.e., electric and magnetic charges associated with every single atom) can be encapsulated in material properties, namely, the electric permittivity $[\epsilon] = \epsilon_0[\epsilon_r]$ (or alternatively, the reflective index n) and the magnetic permeability $[\mu] = \mu_0[\mu_r]$ tensors. In general the elements of permittivity and permeability tensors can be nonlinear and non-local. The use of macroscopic variant of Maxwell's equations is common for describing EM waves in most materials (other than vacuum). This simplification is well justified as long as proper material properties are used in modeling the medium. The use of this approximation significantly relaxes the intractable complexities and computational burdens associated with modeling a myriad of EM sources.

The macroscopic Maxwell's equations in time domain are as follows [16]:

$$\begin{aligned} &\bigtriangledown \cdot \vec{D} = \rho, \\ &\bigtriangledown \times \vec{H} - \frac{\partial \vec{D}}{\partial t} = \vec{J}, \\ &\bigtriangledown \times \vec{E} + \frac{\partial \vec{B}}{\partial t} = 0, \\ &\bigtriangledown \cdot \vec{B} = 0. \end{aligned} \tag{1}$$

In the system of Equations 1, $\vec{E} = \vec{E}(\vec{r}, t)$, $\vec{B} = \vec{B}(\vec{r}, t)$, $\vec{D} = \vec{D}(\vec{r}, t)$, and $\vec{H} = \vec{H}(\vec{r}, t)$ denote the (macroscopic) electric field, the magnetic induction, the electric displacement, and the magnetic field, respectively. Also $\rho = \rho(\vec{r}, t)$ and $\vec{J} = \vec{J}(\vec{r}, t)$ represent the (macroscopic) free (as opposed to bound) electric charge and current densities, respectively. In general, the four field quantities as well as the two sources mentioned above can be functions of time (t) and space ($\vec{r}$).

For simplicity, the following discussion will be restricted to nonmagnetic, linear, and isotropic optical materials. As a result, the permittivity and permeability tensors are diagonal with identical diagonal entities and the electric field, the electric displacement, the magnetic induction and the magnetic field are co-related through the following constitutive relations.

$$\begin{aligned} &\vec{D} = \vec{D}\left(\vec{E}, \vec{B}\right) = \int d\vec{r'} \int dt' \epsilon_0 \epsilon_r \left(\vec{r'}, t'\right) \vec{E}\left(\vec{r} - \vec{r'}, t - t'\right), \\ &\vec{B} = \vec{B}\left(\vec{E}, \vec{H}\right) = \mu_0 \vec{H}. \end{aligned} \tag{2}$$

Note that the medium response, i.e., $\epsilon_r\left(\vec{r'}, t'\right)$, is usually localized around the origin and may be nonvanishing for some range far from $\vec{r'} = 0$ and $t' = 0$. In addition, the free current density in conducting media is related to the electric field through Ohm's law, i.e.,

$$\vec{J} = \sigma(\vec{r}, t) \vec{E}. \tag{3}$$

In Equation 3, σ is the conductivity of the medium. Knowledge of the sources, i.e., $\rho\left(\vec{r},t\right)$ and $\vec{J}\left(\vec{r},t\right)$, and the medium, i.e., $\epsilon_r\left(\vec{r},t\right)$, is sufficient to uniquely determine the macroscopic vector fields at any given point in space and time. Usually for visible, IR, or other EM radiations of longer wavelengths, the spatial non-locality (of the permitivity) can be ignored and the relation between the electric field and the electric displacement can be simplified as follows:

$$\vec{D} = \int dt' \epsilon_0 \epsilon_r\left(\vec{r},t'\right)\vec{E}\left(\vec{r},t-t'\right). \tag{4}$$

In most devices used for integrated photonic applications, there are no free electric charges and/or current sources. In addition,(oftentimes) the steady-state solutions of Maxwell's equations are of interest. Assuming solutions with a time-harmonic dependence, i.e., $e^{-i\omega t}$, for such cases, the Maxwell's equations and the constitutive relations can be combined and recast as:

$$\left(\bigtriangledown^2 + \mu_0\epsilon\left(\vec{r},\omega\right)\omega^2\right)\left\{\begin{array}{c}\vec{E}\left(\vec{r}\right)\\ \vec{B}\left(\vec{r}\right)\end{array}\right\} = 0. \tag{5}$$

Although analytic solutions to the Maxwell's equations exist for a few number of special structures, it is generally difficult (if not impossible) to obtain a closed-form expression for arbitrary geometries (including waveguides and resonators). Alternatively, numerical approaches based on the finite-element-method (FEM) and the finite-difference (FD) algorithms offer convenient means to deal with time-domain and frequency-domain Maxwell's equations. In the next section, FEM (available via comsol software package) in the frequency-domain is used to investigate the properties of two highly used planar photonic structures: optical waveguides and cavities.

2.2 Optical Waveguides

An optical waveguide is a device meant to carry the EM waves from one point to another with as lowest possible distortion. The simplest optical waveguide is formed using at least two dielectric materials with unequal refractive indices. The material with a higher refractive index is used as the core region and the material with a lower refractive index is used as the surrounding region. Since optical fields tend to reside in the material with high refractive index, most of the optical energy is usually confined in the core region. As an example, single-mode fibers (SMF), which are by far the most widely used optical waveguides, consist of a cylindrical core and a cladding material with refractive indices of $n_{core} \approx 1.45205$ and $n_{cladd} \approx 1.44681$, respectively. A typical planar waveguide for chip-scale integrated applications consists of a rectangular core (usually Si, SiN, and or other highly refractive materials) situated on top of a substrate (usually SiO_2). Often, this structure is capped with a cladding material (typically SiO_2) for passivation purposes. The picture shown in Figure 3(a) is a 3D schematic of a typical planar waveguide buried underneath a cladding material.

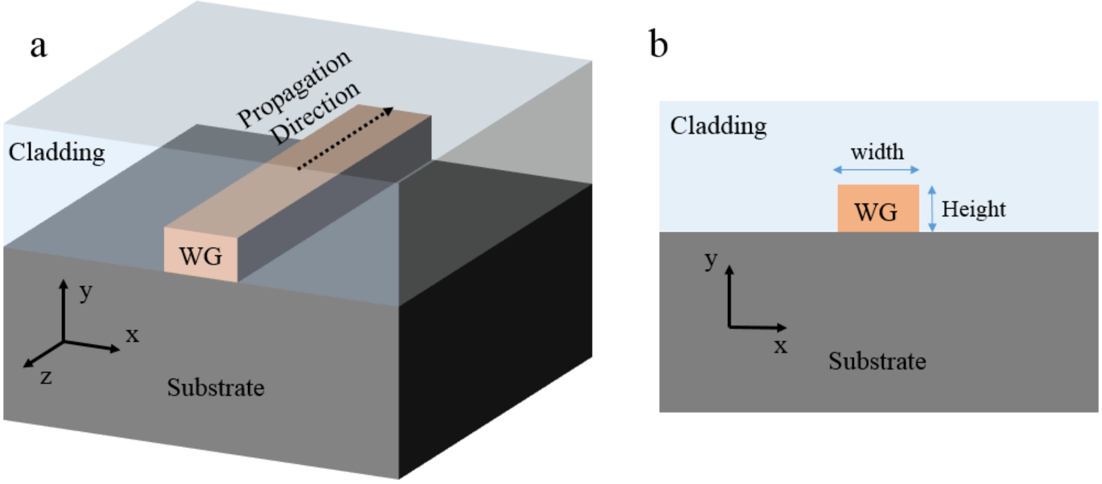

Figure 3: (a) The 3D schematic representation of a typical waveguide structure; (b) The cross-section view of the waveguide structure.

From a design point of view, propagation loss along the waveguide, phase and group velocities (or equivalency dispersion relation), and the spatial profiles of the propagating optical modes constitute the main characteristics of a waveguide. These properties are mainly determined by the dimensions of the waveguide, i.e., width and height, as well as the refractive indices of the core and the surrounding material. Since an ideal waveguide is considered to be homogeneous along the guiding direction and infinitely long, the knowledge of the waveguide's cross-sectional (see Figure 3(b)) geometry is sufficient to determine the above-mentioned features. As a result of the translational symmetry in the waveguide structure (here assumed to be along the z axis), it is possible to factor out the spatial variation of the fields in the z direction and assume the following forms for the electric field and the magnetic induction:

$$\begin{aligned} \vec{E}(x,y,z,t) &= \vec{E}(x,y)e^{\pm ikz-i\omega t}, \\ \vec{B}(x,y,z,t) &= \vec{B}(x,y)e^{\pm ikz-i\omega t}. \end{aligned} \tag{6}$$

The $-$ and $+$ signs in the exponents are associated with the forward and backward propagating waves, respectively. For an arbitrary cross-section geometry, the relationship between the wavenumber (k) and the frequency (ω) of the EM wave is not trivial. The $k(\omega)$ function is the so-called dispersion relation from which the phase velocity v_p (or alternatively effective refractive index $n_{eff} = c/v_p$) and the group velocity v_g (or alternatively group refractive index $n_g = c/v_g$) of the propagating EM wave can be calculated through $v_p = \omega/k(\omega)$ and $v_g = \partial\omega/\partial k(\omega)$. With the assumed z dependence of the fields in Equation 6, Equation 5 reduces to the following two-dimensional form:

$$\left(\triangledown_t^2 + \left(\mu_0\epsilon\left(x,y,\omega\right)\omega^2 - k^2\right)\right)\left\{\begin{array}{c} \vec{E}\left(x,y\right) \\ \vec{B}\left(x,y\right) \end{array}\right\} = 0. \tag{7}$$

In the system of Equations 7, $\triangledown_t^2$ is the transverse part of the Laplacian operator and $\vec{E}\left(x,y\right)$ and $\vec{B}\left(x,y\right)$ are the cross-sectional (transverse) field profiles. Based on the direction of the electric field (referred to as polarization), the mode profiles can be classified into two groups: transverse electric (TE) and transverse magnetic (TM) modes. For TE modes, the electric field $\vec{E}$ mainly lies in the plane of the waveguide, i.e., in the $x-z$ plane, whereas for the TM modes the magnetic-induction vector $\vec{B}$ is mainly in the $x-z$ plane. Many applications require single mode operation (i.e., only one TE/TM mode). This requirement can be ensured by choosing the cross-sectional dimensions, i.e., height h and width w, of the waveguide to be small compared to the EM wavelength. As an example, at the telecommunication wavelength ($\lambda \approx 1550$ nm), a single mode waveguide can be fabricated in an SOI platform with a typical cross-sectional dimensions of $h = 250$ nm and $w = 450$ nm. The norm of the electric field for the TE and TM modes of such a waveguide at $\lambda = 1550$ nm are obtained through FEM in the $x - y$ plane and shown in Figure 4 (the cladding material is assumed to be air).

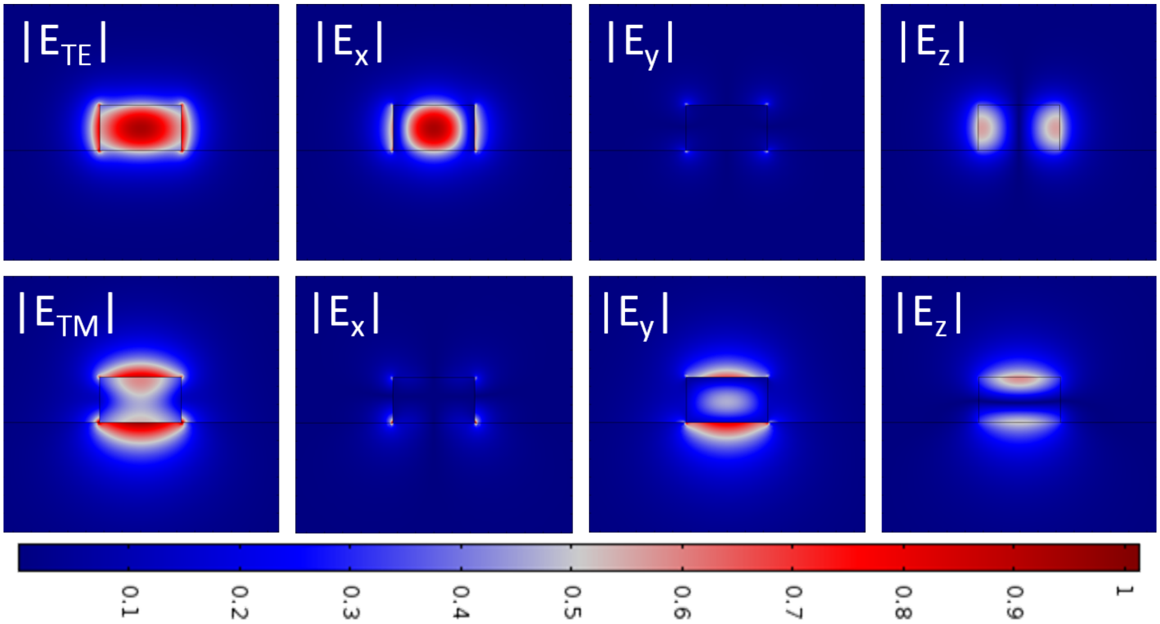

Figure 4: Spatial profiles of the components of the electric field for the TE and TM modes of a Si waveguide with $h = 250$ nm and $w = 450$ nm obtained at $\lambda = 1550$ nm.

In Figure 4, it is seen that the TE mode is more confined to the core region and hence undergoes a larger effective index, i.e., $n_{eff-TE} \approx 2.39$ compared to $n_{eff-TM} \approx 1.78$ in the TM mode. Note that in both cases the mode profiles extend to the low refractive surroundings. As a result, the effective refractive indices for both polarizations are less than the refractive index of the core material, i.e., $n_c \approx 3.48$. In addition, as explained in Section 2.2.1, the waveguide dispersion relation, i.e., $k(\omega)$, can be engineered by choosing a proper cross section.

2.2.1 Dispersion

In contrast to the propagation of an EM wave in free space with no confinement (plane wave), the relation between the wavenumber (k) and the frequency (ω) for an EM wave propagating in a confined medium no longer takes the simple form of $\omega = c/nk$. Depending on the geometrical shape of the propagation medium, i.e., $\epsilon(r,\omega)$, $k(\omega)$ can take an arbitrary form. The dispersion relation for confined media can be obtained by seeking solutions in the form of expressions in Equation 6 for Maxwell's equations. As an example, for an EM wave propagating in a Si waveguide with cross-sectional dimensions of $h = 250\ nm$ and $w = 450\ nm$, the dispersion relations for the supported TE and TM modes are plotted in Figure 5 ($\lambda = 2\pi/k$).

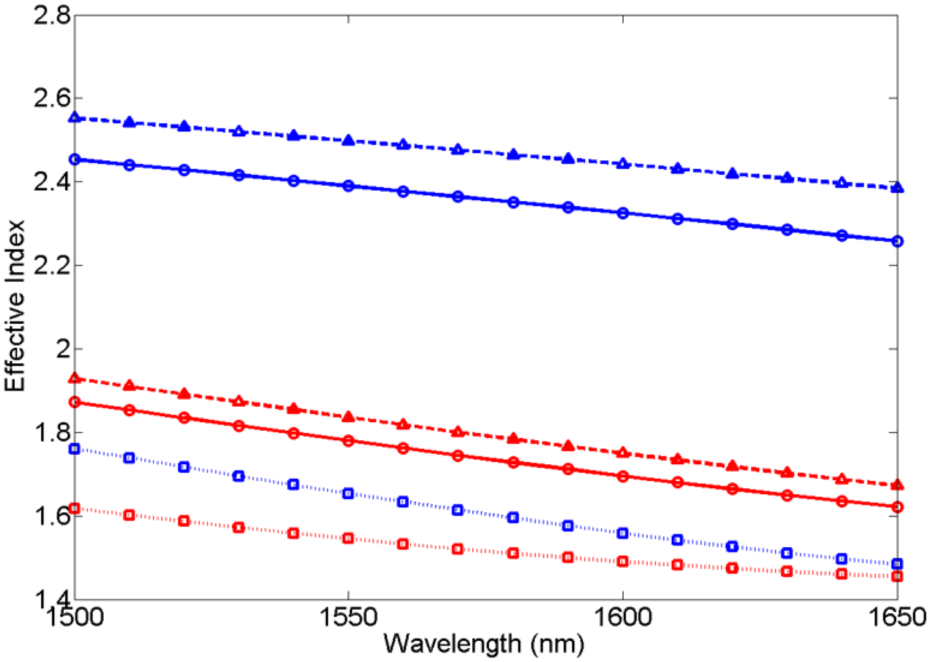

Figure 5: Dispersion plots of the TE and TM modes for Si waveguides with different widths. The red and blue plots correspond to the TM and TE modes, respectively. The corresponding dispersion plots for waveguides with $w = 300\ nm$, $w = 450\ nm$, and $w = 500\ nm$ are distinguished by the square, the circle, and the triangle markers, respectively.

The dispersion curves are obtained through FEM simulations assuming refractive indices of $n_{Si} = 3.48$ and $n_{SiO_2} = 1.45$ for the core and substrate regions. For comparison, the dispersion relation is also calculated for waveguides with two different widths of $w = 300\ nm$ and $w = 500\ nm$. It is seen that the width of the waveguide has a noticeable effect on the effective refractive index. In general, it is safe to conclude that the cross-sectional dimensions of a waveguide significantly affect its dispersion properties. The dispersion plots in Figure 5 suggest that although the effective refractive indices of the TE and TM modes changes substantially over the plotted wavelength range (i.e., from $\lambda = 1500\ nm$ to $\lambda = 1650\ nm$), the corresponding group velocities remain relatively constant judging from the negligible change in the slope of dispersion curves.

2.2.2 Propagation Loss

In an ideal waveguide, the total power of the EM wave (P_0) remains constant all along the waveguide (z direction). However, as a result of material absorption and scattering loss, the optical power in an actual waveguide drops according to $P_0 e^{-\alpha z}$ as the wave propagates in the waveguide. In this expression, $\alpha = \alpha_m + \alpha_s + \alpha_r$ encapsulates the collective effect of material loss α_m, scattering loss α_s, and possibly radiation loss α_r for non-straight waveguides. The material absorption is related to the extinction coefficient k, which is the imaginary part of the refractive index (not to be confused with the wavenumber) through $\alpha_m = (4\pi k)/\lambda$. In a straight waveguide the scattering loss mainly stems from the fabrication-induced sidewall roughness (see Figure 6). Typically the size of the rouphness ($1\ nm - 10\ nm$) is considerably smaller than the wavelength ($\lambda \approx 1550\ nm$). In Figure 6, roughness on the two sidewalls of a typical microring is shown. In contrast to curved waveguides, the radiation loss has negligible effect on power loss in straight waveguides. However, depending on the curvature and refractive index contrast of a waveguide, this loss mechanism can significantly contribute to the overall power loss.

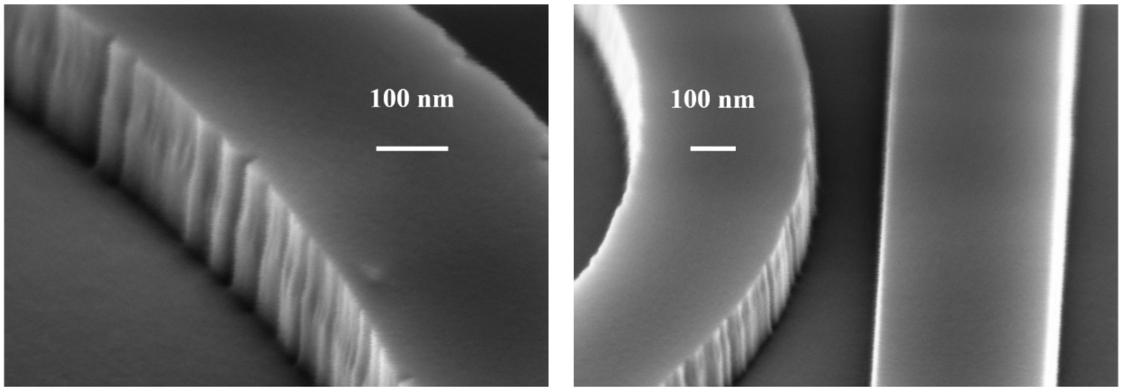

Figure 6: SEM images of the roughness observed on the inner and the outer sidewalls of a microring. The degree of roughness can be minimized by using better fabrication techniques which allow for higher precision.

For a waveguide with length l, the $e^{-\alpha l}$ is referred to as the total propagation loss or attenuation and is usually expressed in dB, which is $-10\log_{10}\left(e^{-\alpha l}\right) = 4.34 \times \alpha \times l$ dB. The attenuation parameter can be normalized to the length of the waveguide and expressed in dB/m, which is $4.34 \times \alpha$ dB/m. Note that with the above definition, the corresponding field amplitudes decay as $e^{-\frac{\alpha}{2}z}$.

2.3 Optical Microcavities

Optical microcavities, also referred to as optical microresonators, are generally used to store EM energy for extended periods of time in a small volumetric region and at specific frequencies. From a structural point of view, integrated microcavities can be classified into a number of distinct geometries including microspheres, microtoroids, microdisks, microdonuts, microrings, one-dimensional photonic crystal (PhC) cavities (also referred to as nanobeam cavities), two-dimensional PhC cavities, three-dimensional PhC cavities. For some of the abovementioned structures, representative SEM images are provided in Figure 7. To keep the discussion short, Only the properties of microdisk cavities will be explored in details. Similar concepts can readily be extended to other types of optical microcavities.

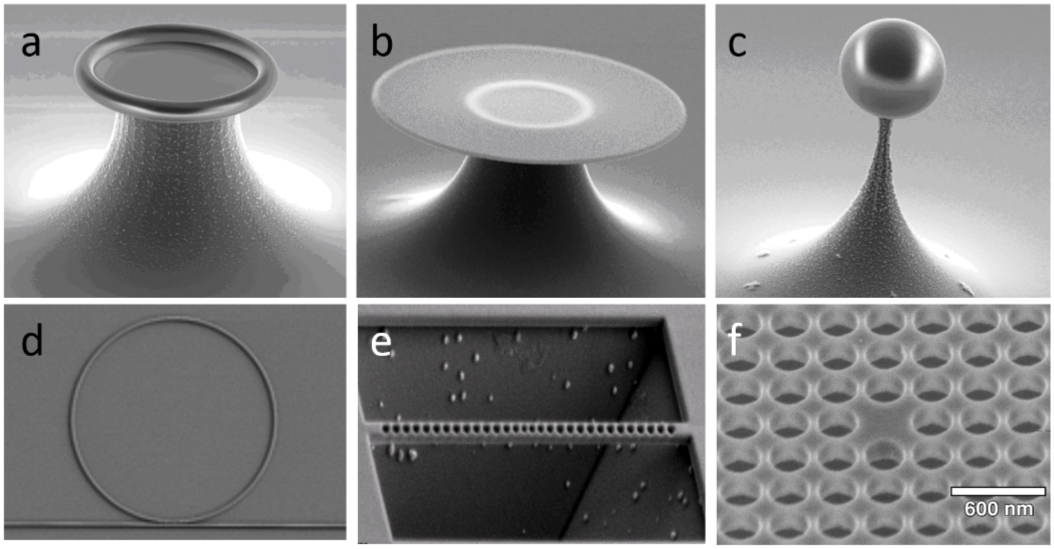

Figure 7: A representative subset of the family of optical micro-cavities. Scanning electron microscopy images of (a) a silica microtoroid on a Si-chip with a radius of 40 μm (from [17]), (b) a microdisk with a radius of 25 μm (from [17]), (c) a silica microsphere with a radius of 11.5 μm (from [17]), (e) a microring cavity on an SOI platform, (e) a Si_3N_4 nanobeam cavity (from [18]), and (f) a two-dimensional PhC cavity in a 175 nm GaAs slab with a single hole defect (from [19]).

A 3D schematic of a typical microdisk cavity is shown in Figure 8(a). As a result of circular symmetry in the geometry of the device, knowledge of the radial cross section (Figure 8(b)) of this device is sufficient to determine its optical properties. Similar to the waveguide model, it is possible to factor out the spatial variation of the fields in the ϕ direction and express the electric field and the magnetic induction in the following forms:

$$\begin{aligned} \vec{E}(r,z,\phi,t) &= \vec{E}(r,z)e^{\pm im\phi - i\omega t}, \\ \vec{B}(r,z,\phi,t) &= \vec{B}(r,z)e^{\pm im\phi - i\omega t}. \end{aligned} \tag{8}$$

In the above expressions, the + and - signs in the exponents are associated with the degenerate clockwise (CW) and counter-clockwise (CCW) traveling waves, respectively. In contrast to an ideal waveguide structure, which is infinitely long with the EM fields confined in only two dimensions, in an optical microcavity the EM fields are confined within the boundaries of the structure in three dimensions. As a consequence, the azimuthal mode number m can only assume discrete values (non-negative integers) in contrast to the wavenumber k which can assume any numerical value (in the range of real numbers).

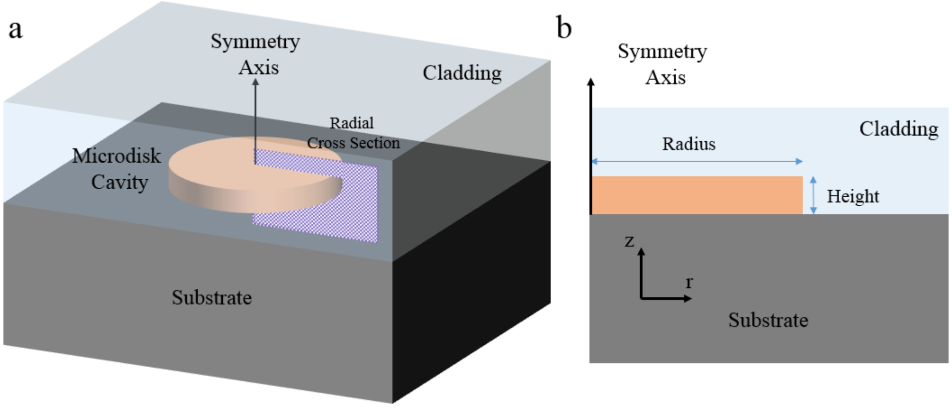

Figure 8: (a) A schematic of a microdisk cavity; (b) A cross-section view of the device taken at $\phi = 0$ in the $r - z$ plane.

The polarization of the supported modes are defined and determined similar to the waveguide model. For a typical microdisk cavity the thickness of the structure is chosen such that higher-order vertical (in z direction) modes are suppressed. However, a microdisk cavity with a large radius compared to the wavelength can support a number of radial modes. As an example, the first three TE radial modes of a Si-based microdisk cavity with a radius of 20 μm and a height of 250 nm are shown in Figure 9 (obtained through FEM simulations around $\lambda \approx 1550$ nm).

In certain applications, e.g., optical spectroscopy and sensing, it is highly desired to work with midrodisk cavities which support only one radial mode. It is possible to suppress the 2^{nd} and higher-order radial modes by reducing the radius of the microsdisk. This approach, however, compromises the quality factor of the structure. Alternatively, for a large-radius microdisk which supports multiple radial modes, the coupling scheme can be optimized (e.g., through the pulley coupling scheme [20]) such that only a specific radial mode is excited. Another approach is to use a microdonut

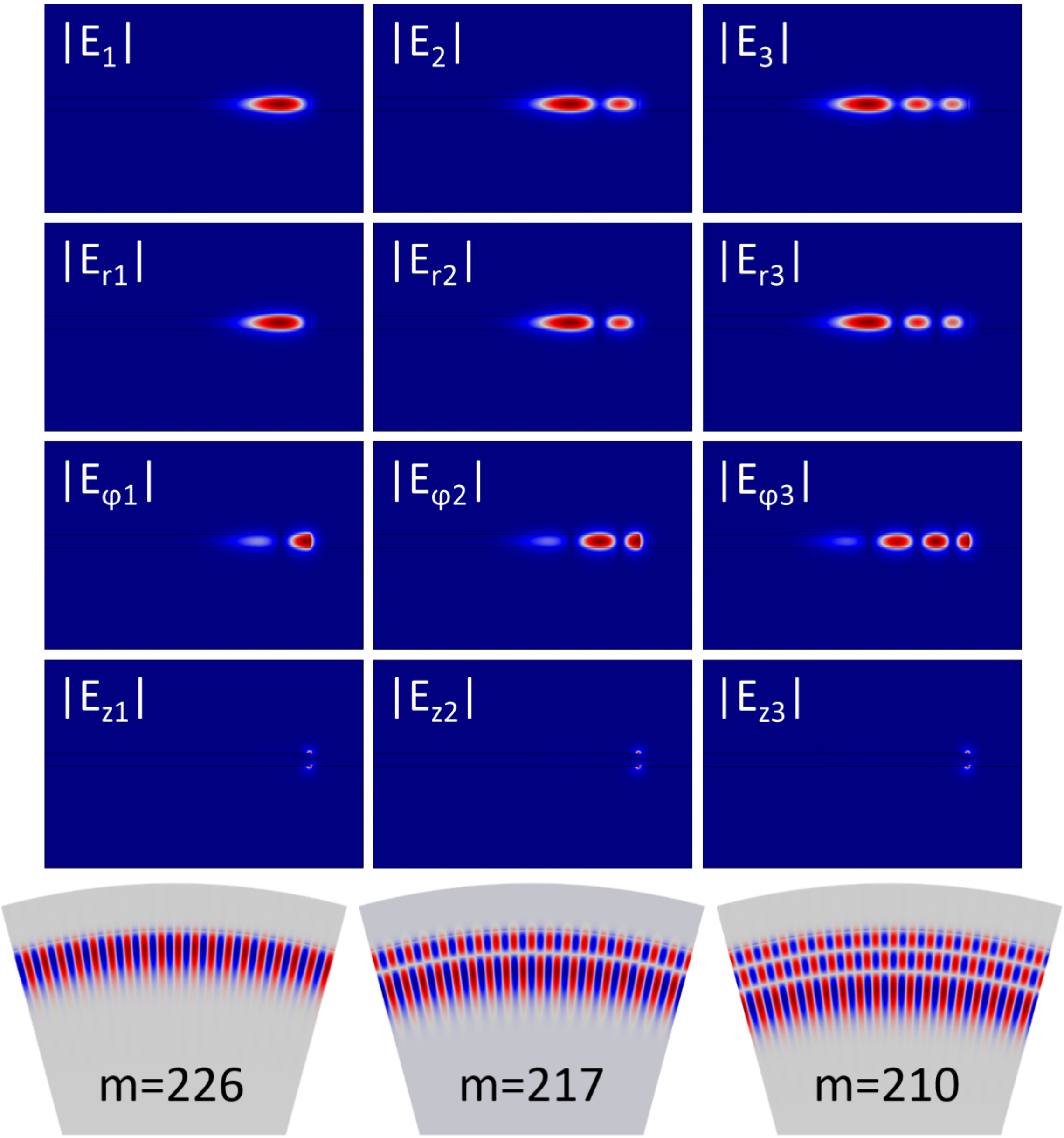

Figure 9: Spatial profiles of the electric-field components of the first (left column), the second (middle column), and the third (right column) radial modes of a 20 μm radius microdisk are shown. The m number for each radial mode is chosen such that the corresponding resonance wavelength is around 1550 nm. The computed resonance wavelengths are $\lambda_1 = 1549.7\ nm$, $\lambda_2 = 1552.7\ nm$, and $\lambda_3 = 1552.2\ nm$. In the bottom row, the top view of $\mathrm{Re}(E_r)$ for the three radial modes (from a 30-degree pie section) of the microdisk are shown.

or a microring geometry to ensure single-radial mode operation which comes at the cost of a lower quality factor.

2.3.1 Quality Factor

Basically, the quality factor (Q) parameter of a microcavity is a normalized measure of optical loss rate in the cavity region (alternatively, Q can be thought of as a measure for the frequency-domain sharpness of the device response to an external excitation). Mathematically, Q can be defined for each resonant mode as follows:

$$Q = \frac{2\pi f_0 U_C}{P_{Loss}} \tag{9}$$

In Equation 9, U_C is the optical energy stored in the cavity, $f_0 = 1/T$ is the temporal frequency of the resonant mode, and $P_{loss} = -dU_C/dt$ is the collective leaked and dissipated optical energy over one period of temporal oscillation, i.e., T. It is easy to see that in the absence of external sources, the initial stored energy (U_{C0}) in the cavity decays exponentially as:

$$U_C = U_{C0} e^{-2\pi f_0 t/Q}. \tag{10}$$

The corresponding damping effect in the oscillation of the field amplitudes F (F represents any of E, D, B and or H) in the cavity is as follows:

$$F(t) = F_0 e^{-2\pi f_0 t/(2Q)} e^{-i2\pi f_0 t}. \tag{11}$$

From Equation 10, it seems natural to define $\tau = Q/\left(2\pi f_0\right)$ as the photon lifetime in the cavity (alternatively, one can define decay rate of the cavity as $\gamma = 1/\tau$). Note that If Q is defined for the amplitude of the optical field rather than its energy, the photon lifetime expression will be $\tau = Q/\left(\pi f_0\right)$. In Equation 10, simple means is provided to experimentally estimate the Q parameter by conducting time-domain measurements (usually done for ultrahigh-Q devices). The Q parameter can also be estimated by frequency-domain measurements. It is easy to see that the damped oscillation of the fields given in the generic form of Equation 11 does not posses a single frequency but a spectrum spreading around f_0. A straightforward Fourier transform analysis results in the following Lorentzian expression for the spectral content of such oscillations.

$$F(\omega) = \frac{1}{(\omega - \omega_0)^2 + (\pi f_0/Q)}. \tag{12}$$

From a practical point of view, this expression allows to estimate the Q-factor by simply measuring the full-width (Γ) at half maximum of the resonance shape ($\Gamma = \omega_0/Q$). It is clear that high Q values correspond to sharper spectral lineshapes. Material loss, scattering loss, and radiation loss are the main loss mechanisms which collectively determine the intrinsic quality factor (Q_i) of a microcavity. It is possible to define a quality factor fpr each loss mechanism, i.e., Q_r for the radiation loss, Q_m for the material loss, and Q_s for the scattering loss. Although radiation loss (Q_r) can be minimized by optimizing the geometry of the cavity (e.g., by avoiding sharp bends), other loss mechanisms are less amenable to geometrical optimization. For example, the scattering loss (Q_s) which results from unavoidable fabrication imperfections, e.g., sidewall roughness (see Figure 6), is mainly dictated by the precision of the fabrication instruments. The intrinsic material loss (Q_m) is usually negligible compared to other loss mechanisms for medium-Q values. However, it can play a significant role in high field intensities through nonlinear absorption mechanisms. The intrinsic quality factor (Q_i) can be written in terms of other Qs as:

$$1/Q_i = 1/Q_s + 1/Q_m + 1/Q_r. \tag{13}$$

Values on the order of hundreds of thousands are common for Q_i in integrated optical microcavities.

2.3.2 Free Spectral Range and Finesse

In general, an optical cavity can support an infinite but countable number of resonant modes. The free spectral range (FSR) parameter is simply the relative distance, measured in frequency or wavelength, between successive resonant modes. The supported discrete modes of a cavity can be labeled by a collective index such as n and referred to by the corresponding resonance frequency, i.e., f_n (or equivalently their resonance wavelength, i.e., λ_n). In addition it is possible to sort the resonant modes such that $f_n < f_{n+1}$ (or equivalently $\lambda_n > \lambda_{n+1}$). Assuming that all modes are non-degenerate, i.e., $f_i \neq f_j$, the FSR parameter can be calculated as follows:

$$\begin{aligned} \mathrm{FSR} &= \delta f = f_{n+1} - f_n, \\ \mathrm{FSR} &= \delta\lambda = \lambda_n - \lambda_{n+1}. \end{aligned} \tag{14}$$

It is easy to show that for a cavity of length L and a group index of $n_g(\lambda)$, the FSR can be estimated through the following expression:

$$\mathrm{FSR} = \frac{\lambda_0^2}{n_g L}. \tag{15}$$

As mentioned in Section 2.3, a microdisk cavity can support several radial modes. The azimuthal modes (labeled by m) associated with each radial mode form a family of modes. For this class of optical microcavities, the FSR parameter usually refers to the wavelength (or frequency) separation for modes within one specified family (i.e., a specific radial mode). Oftentimes the FSR of a family differs significantly from those of other families. As an example, the FSR for the first, the second and the third radial modes (TE) of a microdisk with 20 μm radius (shown in Figure 9) are 5.39 nm, 5.47 nm, and 5.51 nm, respectively (calculated around 1550 nm). Difference in FSR allows for identification of resonant modes when required.

In Figure 10, the relative positions of resonant modes for an hypothetical miscrodisk cavity with (a) one radial mode, (b) two radial modes and (c) three radial modes are shown (assuming single polarization). As shown, FSR mode density increases with number of radial modes. However, all modes which belong to a specific family can be identified by detecting and tracking the related FSR. Note that in general, the TE and TM modes also exhibit distinct FSRs. For this reason, spectral characterization of a cavity with one radial mode can still contain modes which are separated according to two distinct FSRs.

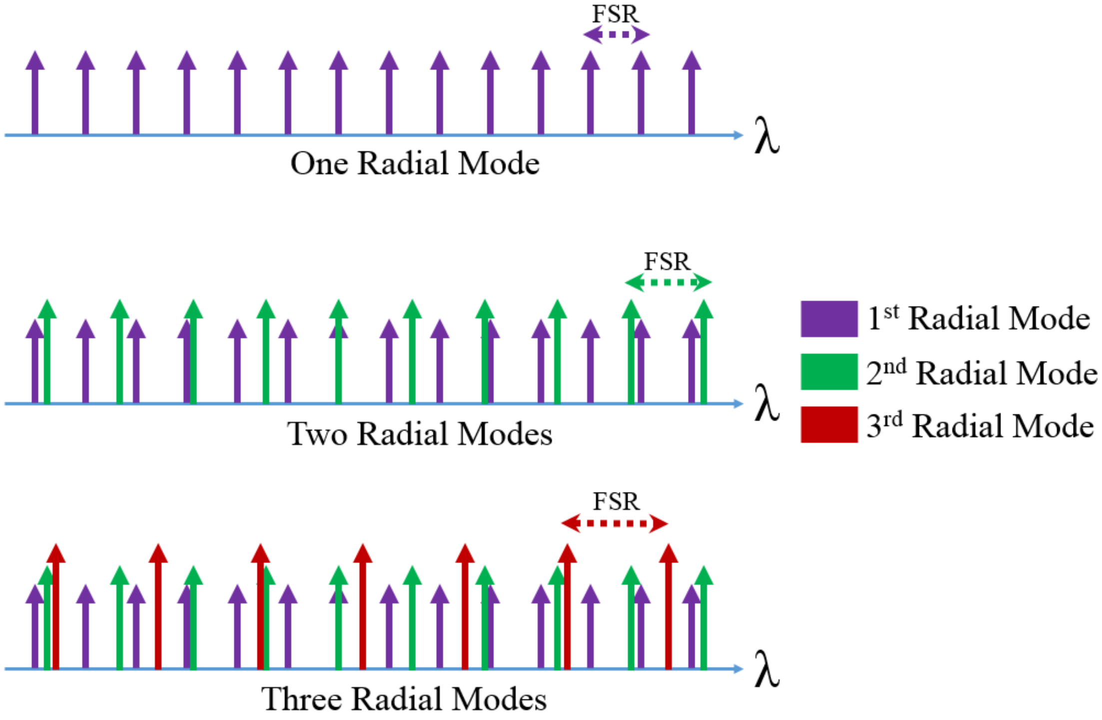

Figure 10: Typical spectral distribution of resonant modes of a single-polarization microdisk cavity supporting (a) one, (b) two, and (c) three radial modes. As shown, the FSR for each family differs from that of the rest.

Although the exact value of the FSR depends on the frequency (or wavelength), this dependence is very weak and often negligible. Resorting to numerical methods is a simple yet effective way for determining the value of FSR within each mode family. Another parameter closely related to the FSR is finesse. Finesse is defined as the ratio of the FSR to the 3-dB linewidth (i.e., the full-width at half-maximum Γ) of the resonant modes. This parameter can be written in terms of Q and resonance frequency (ω_0) as follows:

$$\text{Finesse} = \frac{\text{FSR}}{\Gamma} = \text{FSR}\frac{\omega_0}{Q}. \tag{16}$$

A high-finesse resonator is appealing for many applications including optical spectrum analysis (spectrometers), sensing, and cavity quantum electrodynamic (CQED). As will be discussed in the later part of Section 2.4, a high-finesse cavity can be used to enhance EM field amplitudes.

2.3.3 Mode Volume

As mentioned in Section 2.3, the resonant modes of optical microcavities are localized in space. The mode volume parameter is a measure of the spatial extent of the corresponding field profile. Depending on the application, the effective mode volume (V_{eff}) of a resonant mode can be defined in various ways. In general, smaller mode volumes indicate higher field intensities in a cavity for a fixed excitation. One particularity useful definition of mode volume is:

$$V_{\text{eff}} = \frac{\int dr^3 \epsilon\left(r\right) |\vec{E}\left(r\right)|^2}{\max\left[\epsilon\left(r\right) |\vec{E}\left(r\right)|^2\right]}. \tag{17}$$

In Equation 17, $\vec{E}(r)$ is the electric-field vector, and $\epsilon(r)$ is the dielectric constant (or permittivity).

2.4 Coupled-mode Theory for Coupled Waveguide-cavity Systems

Perfectly isolated (i.e., no interaction with other external entities) optical microcavities have limited practical use as it is not possible to optically excite them or access their stored optical energy. To benefit from all the features offered by microcavity structures, it is imperative to couple EM waves in and out of the microcavity by some means. A simple yet powerful way to access the resonant modes of a microcavity is through coupling of evanescent waves. This approach can be applied using a variety of techniques, e.g., by the use of an access waveguide (or a tapered optical fiber) which is located in the vicinity of the cavity. As shown in Figure 11, this maximum coupling between access waveguide and microcavity in this technique occurs at a single point/region where the waveguide is closest to the microcavity. For this reason, this technique is usually referred to as the point-coupling scheme.

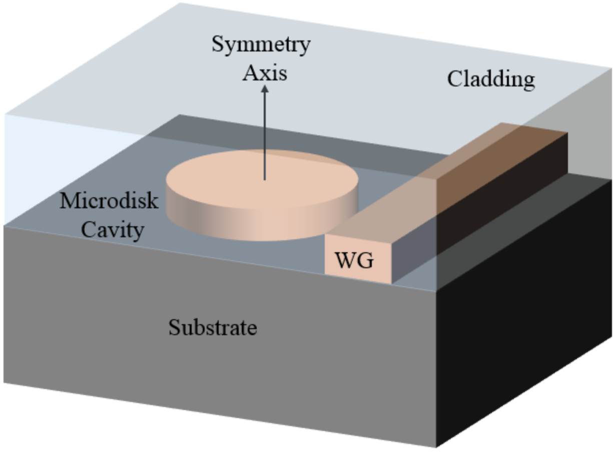

Figure 11: Schematic representation of a point-coupled access waveguide placed in proximity of a microdisk cavity.

Since the optical modes supported by both devices have exponentially decaying spatial profiles outside their physical boundaries, it is possible to choose the gap size of the coupling region to ensure a non-zero overlap between the corresponding optical modes. The nearby access waveguide provides a new leakage path for the optical energy stored in the cavity. This path constitute a new loss mechanism (referred to as the coupling loss) and can be modeled by a coupling-Q (Q_c) parameter. Note that in parallel to energy leakage from cavity, the access waveguide can provide a means to couple EM energy into the cavity. The overall effect of this coupling will be a drop in the total (as opposed to the intrinsic) quality factor estimated by the following expression:

$$1/Q_T = 1/Q_c + 1/Q_i. \tag{18}$$

The transmission characteristics of the access waveguide can be easily modeled by the steady-state coupled-mode theory (CMT), which models the behavior over time periods much longer than the time required for the EM energy to build up inside of the cavity. For a coupling region shown in Figure 11, the field transmission coefficient (τ) and the field coupling coefficient (κ) can be defined as $\tau = E_t/E_i$ and $\kappa = E_c/E_i$ (see Figure 12(a) for the corresponding illustrations of E_i, E_c, and E_t). Generally, κ

and τ are complex-valued quantities, and can be shown to satisfy $|\kappa|^2 + |\tau|^2 = 1$ that for a lossless coupling region. Note that by changing the gap size between the access waveguide and the microcavity, the numerical values for τ (and κ) can be controlled. As an example, if the gap size is chosen large compared to the spatial decay rates of the optical modes (i.e., vanishing overlap integral), the transmission coefficient will be close to 1, assuming a lossless coupler.

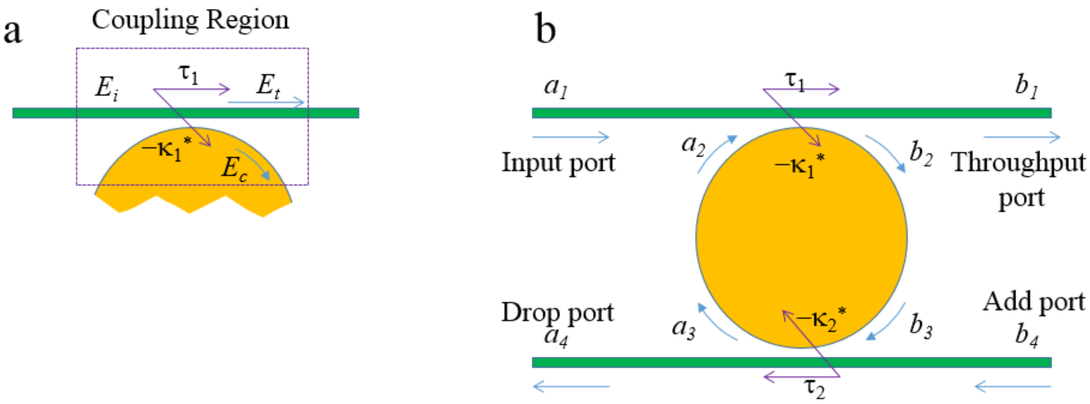

Figure 12: Coupling configurations of (a) single-waveguide and (b) double-waveguide are shown for a microdisk cavity.

In general, a microcavity can have more than one access point. As an example, in Figure 12(b) a system comprising a microcavity and two access waveguides is shown. In what follows, the CMT is applied to analyze this system. By inspecting the structure in Figure 12(b), it is easy to see that the following field relations hold:

$$\begin{aligned} b_1 &= \tau_1 a_1 + \kappa_1 a_2, \\ a_4 &= \tau_2 b_4 + \kappa_2 b_3. \end{aligned} \tag{19}$$

In Equation 19, a_1 and b_1 are the field amplitudes in the input and the throughput ports of the top waveguide, respectively. Similarly a_4 and b_4 are field amplitudes in the drop, and the add ports of the bottom waveguide. Moreover, a_2, a_3, b_2, and b_3 are the field amplitudes inside the microcavity as shown in Figure 12. $\kappa_{1,2}$ and $\tau_{1,2}$ are the coupling and transmission coefficients of the first and the second coupling regions, respectively. As discussed earlier, considering different intrinsic loss mechanisms, the EM fields in the resonator undergo attenuation as they travel around the circumference of the microdisk cavity. The total field attenuation in one trip around the microdisk (also referred to as the loss coefficient) is assumed to be α_i. Note that for a cavity of length L the field attenuation α_i can be expressed in terms of the intrinsic Q of the cavity (Q_i) through $Q_i = \frac{-2\pi n_{eff} L}{\lambda_0 \ln(\alpha_i/2)}$. In addition the EM wave picks up a geometrical phase (ϕ) as it propagates along the periphery of the microcavity. These phenomenon can be used to related the field at various points in the microcavity as follows:

$$\begin{aligned} b_3 &= \sqrt{\alpha_i} e^{-i\phi/2} b_2, \\ a_2 &= \sqrt{\alpha_i} e^{-i\phi/2} a_3, \\ a_3 &= \tau_2^* b_3 - \kappa_2^* b_4, \\ b_2 &= \tau_1^* a_2 - \kappa_1^* a_1. \end{aligned} \tag{20}$$

Note that the accumulated phase (ϕ) depends on the frequency (or equivalently wavelength) as well as the phase velocity (or effective refractive index) of the considered optical mode ($\phi(\omega)$). The intercavity field amplitudes in the system of Equations 20, i.e., b_3 and a_2, can be expressed in terms of the input field amplitudes, i.e., b_4 and a_1, as follows:

$$\begin{aligned} b_3 &= \frac{-\alpha_i \tau_1^* \kappa_2^* e^{-i\phi}}{1 - \alpha_i \tau_2^* \tau_1^* e^{-i\phi}} b_4 - \frac{\sqrt{\alpha_i} \kappa_1^* e^{-i\phi/2}}{1 - \alpha_i \tau_2^* \tau_1^* e^{-i\phi}} a_1, \\ a_2 &= \frac{-\alpha_i \tau_2^* \kappa_1^* e^{-i\phi}}{1 - \alpha_i \tau_2^* \tau_1^* e^{-i\phi}} a_1 - \frac{\sqrt{\alpha_i} \kappa_2^* e^{-i\phi/2}}{1 - \alpha_i \tau_2^* \tau_1^* e^{-i\phi}} b_4. \end{aligned} \tag{21}$$

In addition, by combining the system of Equations 19 and 21 the output field amplitudes, i.e., b_1 and a_4, can be written in terms of the input field amplitudes as follows:

$$\begin{aligned} b_1 &= \frac{\tau_1 - (|\tau|^2 + |\kappa|^2) \alpha_i \tau_2^* e^{-i\phi}}{1 - \alpha_i \tau_2^* \tau_1^* e^{-i\phi}} a_1 - \frac{\sqrt{\alpha_i} \kappa_1 \kappa_2^* e^{-i\phi/2}}{1 - \alpha_i \tau_2^* \tau_1^* e^{-i\phi}} b_4, \\ a_4 &= \frac{\tau_2 - (|\tau|^2 + |\kappa|^2) \alpha_i \tau_1^* e^{-i\phi}}{1 - \alpha_i \tau_2^* \tau_1^* e^{-i\phi}} b_4 - \frac{\sqrt{\alpha_i} \kappa_1^* \kappa_2 e^{-i\phi/2}}{1 - \alpha_i \tau_2^* \tau_1^* e^{-i\phi}} a_1. \end{aligned} \tag{22}$$

For a special case, where only one waveguide is present and the coupling region is lossless, Equations 19, 20, 21, and 22 can be simplified by setting $\kappa_2 = 0$, $\tau_2 = 1$, and $|\kappa|^2 + |\tau|^2 = 1$. In this case, Equation 22 is reduced to the following expression describing the waveguide transmission ($T(\phi)$):

$$T(\phi) = \frac{b_1}{a_1} = \frac{\tau_1 - \alpha_i e^{-i\phi}}{1 - \alpha_i \tau_1^* e^{-i\phi}}. \tag{23}$$

Note that the resonance condition is satisfied for specific frequencies (such as ω_r) where the accumulated phase in one round trip is an integer multiple of 2π, i.e., $\phi(\omega_r) = \pm 2\pi n$ ($n \in \mathbb{Z}$). Depending on the relative magnitudes of the transmission coefficient and the field attenuation, three distinct regimes of operation can be identified: (a) $\alpha_i > \tau_1$ which is referred to as the under-coupled regime, (b) $\alpha_i = \tau_1$ which is referred to as the critically coupled regime and (c) $\alpha_i < \tau_1$ which is referred to as the over-coupled regime. The fields intensities in the cavity can be much higher than that in the access waveguide. This can be seen by looking at the following field ratio for the case when the Add port is not excited (i.e, $b_4 = 0$):

$$B = |\frac{a_2}{a_1}|^2 = |\frac{-\alpha_i \tau_2^* \kappa_1^* e^{-j\phi}}{1 - \tau_1^* \tau_2^* \alpha_i e^{-j\phi}}|^2. \tag{24}$$

For a symmetric and low-loss microcavity (i.e., $\kappa_1 = \kappa_2 = \kappa << 1$, $\tau_1 = \tau_2 = \tau \approx 1$, and $\alpha_i \approx 1$) the enhancement factor (Equation 24) at resonance (i.e., $\phi = 0$) can be reduced to:

$$B = |\frac{a_2}{a_1}|^2 = |\frac{-\kappa^*}{1 - \tau^2}|^2 = |\frac{1}{\kappa}|^2. \tag{25}$$

It can be shown that the enhancement factor in this regime can be written in terms of finesse ($B = |1/\kappa|^2 = \text{finesse}/\pi$). This expression provides a practical way to estimate the field enhancement by measuring the spectral transmission response of the access waveguide. The field enhancement property of microcavities renders them appealing for nonlinear applications with low-power excitations. The transmission coefficient (τ) can also be converted to an equivalent Q-factor referred to as the waveguide-cavity coupling Q (Q_c) parameter. The phase and amplitude of the transmission for under-, over-, and critically-coupled regimes are plotted in Figure 13 for a microcavity featuring a fixed $Q_i = 10k$ (or equivalently $\alpha_i \approx 0.98$ for a 6 μm radius resonator).

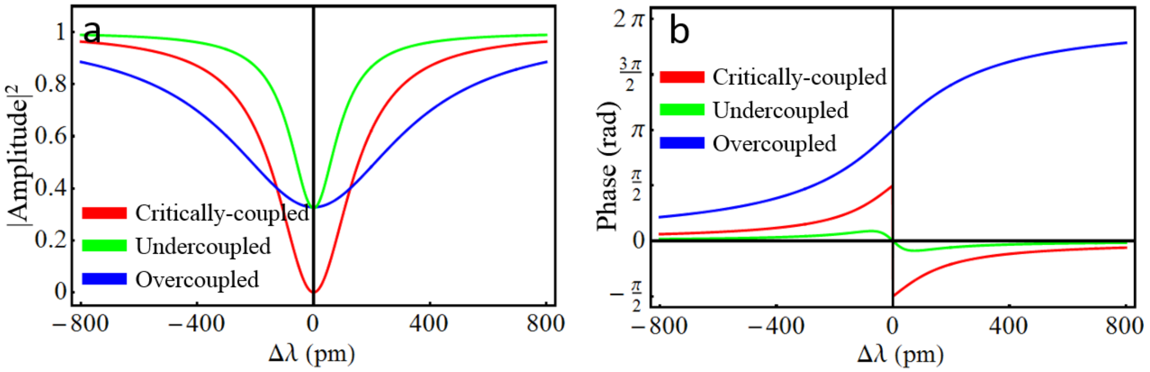

Figure 13: (a) Amplitude and (b) phase characteristics of a transmitted EM wave around the resonance wavelength of a waveguide-coupled microcavity for critically-coupled (red), undercoupled (green), and overcoupled (blue) regimes.

The plots in Figure 13 indicate that once the EM wave in the access waveguide passes through the coupling region its amplitude and phase can experience a dramatic change. In the over-coupled regime, the EM wave phase factor can gain up to 2π. However, in the critically-coupled regime this phase factor can only reach a maximum of π, and for the under-coupled case this phase factor is invariably less than π. Moreover, it is seen that depending on the coupling regime, the normalized field amplitude of the transmitted wave can vary significantly. In the over-coupled case, the resonance linewidth future broadens compared to the critically coupled case. In a heavily over-coupled regime, the sharp resonance feature disappears and the transmission curve flattens. This regime of operation can be used to design delay lines of very small footprints with low insertion loss. In the undercoupled case, the lineshape of the resonance remains sharp. However, as the waveguide-cavity coupling becomes weaker, the amplitude extinction at resonance decreases progressively. These observations allow for the implementation of simple optical modulation schemes, e.g., on-off keying (OOK) and binary phase shift keying (BPSK), using coupled waveguide-cavity units. Implementation of spectrally efficient high-order modulation formats, such as quadrature phase shift keying (QPSK), are also possible by combining waveguide-cavity units with Mach-Zehnder interferometers.

CHAPTER III

AN INTERLAYER GRATING COUPLER DESIGN FOR A SI/SIO$_2$/SIN HYBRID PLATFORM

3.1 Overview

As explained in the introduction chapter, no single-material platform offers all the required properties for the realization of complex optical systems in which power, speed, insertion loss, and device footprint are not traded off against each other. Hybrid material platforms, e.g., in the form of multi-layer structures with different materials in each layer offering the necessary optical properties (e.g., low loss, reconfigurability, nonlinear optical effects, gain) for functional integrated photonic devices, provide an attractive solution to this challenge. An example is a hybrid Si/SiN platform in which low-loss devices (e.g., high-Q resonators and low-loss optical delay lines) are fabricated in the SiN layer; and the tunable devices are fabricated in the Si layer. A major requirement in using such hybrid platforms is the ability to efficiently couple light between different layers to avoid high overall insertion loss. The transfer of optical power between layers can be achieved through either evanescent or propagating field coupling. In the case of evanescent field coupling, efficient coupling can take place in a reasonably small footprint, provided that the two coupled layers are stacked in the vicinity of each other with the buffer layer thickness (if any) not exceeding few hundreds of nanometers. Such a coupling scheme has already been demonstrated in Si/SiO$_2$/SiN platform featuring 0.4 ± 0.2 dB waveguide-to-waveguide insertion loss with a 3-dB bandwidth of 20 nm, and 0.8 ± 0.2 dB insertion loss with a 3-dB bandwidth of 100 nm [21]. Moreover, evanescent coupling from a Si waveguide in a lower layer to a high-Q (e.g., $Q = 10^6$) SiN resonator in the top layer has been demonstrated [22]. The shortcoming of this scheme is the limited ability to control (specifically suppress) the coupling level between the two layers at arbitrary locations on the chip. On one hand, a thin buffer layer between the two layers is desired to achieve reasonable coupling in short distances. On the other hand, a thin buffer layer can result in unwanted coupling (and consequently scattering/crosstalk) between the two layers at other locations (see Figure 14). This issue poses an extra constraint on the layout of the devices on both layers. Therefore, in applications where dense integration is of concern, excessive optical scattering loss and interference are to be compromised against on-chip real estate and are sometimes unavoidable.

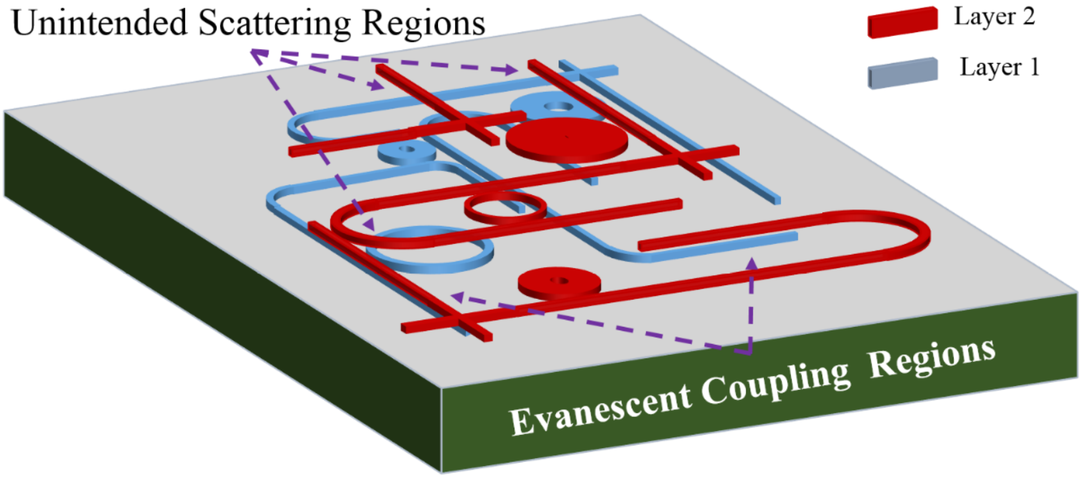

Figure 14: A hypothetical optical circuitry on a multilayer material platform with a thin buffer layer. Optical power is coupled through evanescent waves between the the top (red) and the bottom (blue) layers.

An alternative approach is to use a thicker buffer layer to alleviate the interference and scattering issue. The power transfer between the two layers in this scheme can be realized by the incorporation of diffractive elements such as grating couplers or angled refractive micro-mirrors. The latter approach entails non-vertical etching (usually done through wet etching by relying on the direction-dependent etch rate of the crystalline material), which makes the fabrication process more challenging for arbitrary substrates. Direct optical links have been demonstrated using angled micro-mirrors for chip-to-chip coupling on the Si platform; and a facet-to-facet insertion loss of 2.5 *dB* has been demonstrated [23, 24]. On the other hand, the diffractive grating-based optical proximity coupling can be realized through conventional vertical dry etching and hence is more applicable for a wider range of materials. The utilization of diffractive gratings for interlayer/chip-to-chip power transfer has been demonstrated by various groups in several material platforms such as Si/SiO_2/Si and Si/SiO_2/SU-8 stacks with the best reported insertion losses of around 1.5 *dB* and 6 *dB*, and 3-dB bandwidths of 51 *nm* and 41 *nm*, respectively [25, 26, 27, 28]. Interlayer grating couplers on hydrogenated amorphous Si layers have also been demonstrated with a high efficiency of 83% and a 3-dB bandwidth of more than 40 *nm* [29]. Despite the unique advantages of the Si/SiO_2/SiN platform for future three-dimensional (3D) integrated photonic structures, an efficient grating-based coupling scheme in this platform has not been reported yet. A versatile coupling scheme with a systematic design approach for this material platform is highly beneficial for the future integrated photonic systems. In this work, I report, for the first time, the design and implementation of single/double reflector-enhanced interlayer grating couplers for the Si/SiO_2/SiN platform with a rather thick buffer layer. My simulations predict unprecedented high coupling efficiencies of about 89% and 64% (0.5 *dB* and 1.9 *dB* insertion losses, respectively) along with 3-dB bandwidths of 40 *nm* and 50 *nm* for single- and double-mirror structures, respectively. The fabricated single-mirror device exhibits 2 *dB* insertion loss along with > 40 *nm* bandwidth. The proposed structure along with the design approach and simulation results are presented in Section 3.2. The fabrication process is reviewed in Section 3.3. Final conclusions and the experimental results are presented in Section 3.4.

3.2 Design Method

Figure 15 shows the schematic of the proposed coupling structure in a 3D Si/SiO_2/SiN hybrid material platform. In this structure light from a ridge waveguide in the (lower) Si device layer is coupled to a SiN microring resonator in the higher layer through a SiN waveguide. The coupling between the two layers is achieved by using two gratings in the Si and SiN layers (see Figure 15(b)). These two layers are separated by a relatively thick SiO_2 buffer layer to minimize the unwanted crosstalk coupling between the layers.

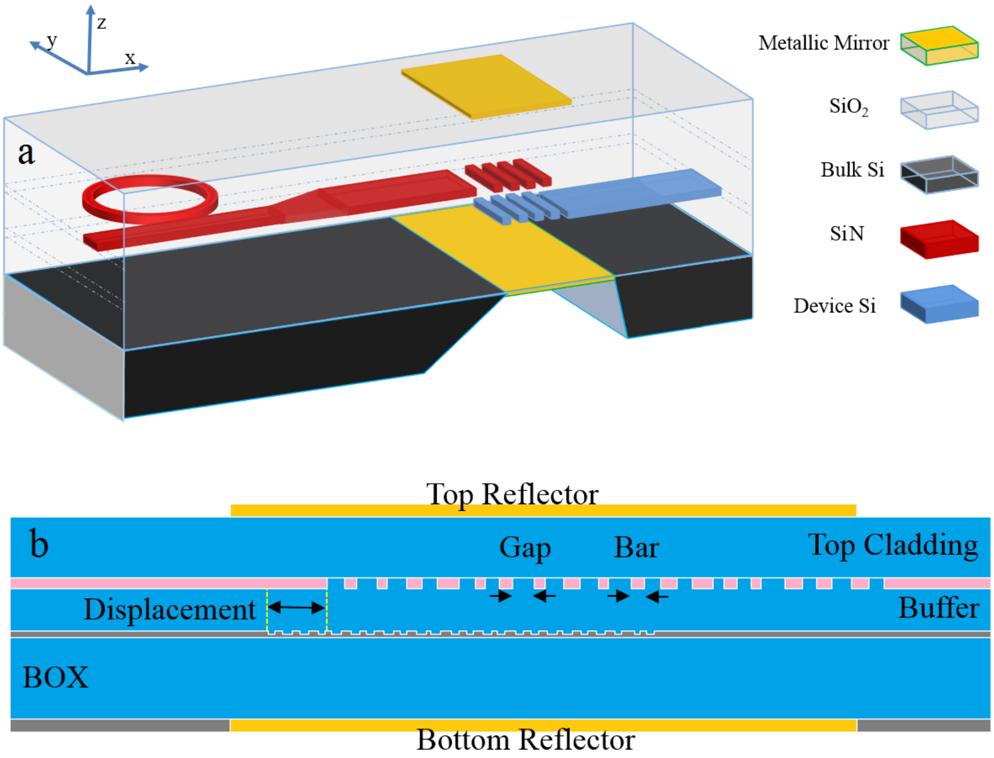

Figure 15: (a) A schematic of the interlayer grating coupler enhanced with top and backside metallic reflectors to couple light from a Si waveguide (lower layer) to a ring resonator coupled to the access waveguide on the SiN layer (top layer). (b) The detailed cross section of the device around interlayer grating coupler. Each grating period is divided into a material (i.e., Si or SiN) part (called 'bar') and a groove part (called 'gap'). The beginning of the top layer grating is displaced from that of the bottom layer grating by an amount referred to as 'displacement'. The gratings on the Si and SiN layers contain 18 and 24 grooves, respectively; and their widths and positions are found by the optimization process.

Several design parameters can be chosen to design and optimize the interlayer grating couplers in Figure 15(b). While the thicknesses of these layers (i.e., Si, SiO_2, and SiN) can be considered as design parameters, they are usually selected by practical considerations. For example, commercially available SOI wafers offer only a few options for the thicknesses of the SiO_2 buried oxide (BOX) and the Si device layers. In this design, a 3 μm-thick BOX layer and a 250 nm-thick Si device layer are assumed, to comply with practical requirements. Also, the thickness of the SiN layer is usually limited by its deposition technique. For higher quality SiN films, a low-pressure chemical vapor deposition (LPCVD) technique is desired. Thicker SiN films are desired for realizing more compact devices (e.g., resonators and waveguides) with a better field confinement. Yet, in light of the deposition process, there exists an upper bound, dictated by the stress of the layer, beyond which stress-induced cracks appear all over the sample and render it unfit for high-yield fabrication. This upper bound, depends on the substrate (e.g., SOI here) and its thickness, the SiO_2 buffer thickness, the SiN deposition temperature, and the involved gas ratios in the LPCVD process [30]. My initial tests proved that the combination of 400 nm SiN and 1.6 μm buffer oxide on 250 nm Si is immune to cracking. The top cladding layer (SiO_2) thickness is inconsequential and is simply chosen to be 2.25 μm. Fixed etch depths of 90 nm and 400 nm for the gratings on the Si and SiN layers are assumed, respectively, during the optimization. As shown in Figure 15(a), the top of the cladding and the bottom of the BOX layers are also coated with a thin reflective metal to enhance the efficiency of the power transfer between the two layers by containing the field in a vertical Fabry-Perot cavity, on the two sides of the interlayer grating coupler.

With layer thicknesses fixed, the problem of designing the efficient interlayer coupler reduces to finding optimal geometries for the two gratings in the Si and SiN layers. In this optimization, the bottom (Si) and the top (SiN) gratings are assumed to have 24 and 18 grooves (periods), respectively. The design parameters are the groove width (identified by 'gap' in Figure 15(b)) and the material width (identified by 'bar' in Figure 15(b)) in each period of each grating. This is an unconstrained global optimization problem with the reward function being the coupling efficiency.

Considering the high-dimensional search space (assuming the grating geometries are arbitrary), brute-force search approaches are not feasible due to the extremely high computational cost. Metaheuristic approaches such as genetic algorithm (GA) or particle swarm optimization (PSO) are highly effective in dealing with various classes of optimization problems. In my case, a GA code (in Matlab) is developed to perform geometrical optimization. Starting with an educated guess for the initial values of the parameters in GA can result in faster convergence. In my case, the initial designs for the gratings are periodic with periods (Λ_{Si} and Λ_{SiN} for Si and SiN gratings, respectively) chosen according to the Bragg condition for both gratings [31]:

$$k \sin(\alpha) + m\frac{2\pi}{\Gamma_{Si,SiN}} = \beta_{Si,SiN}. \tag{26}$$

First-order diffraction, i.e., $m = 1$, for both gratings is assumed. In Equation 26, $k = \frac{2\pi n_{Buffer}}{\lambda}$, $\beta_{Si} = \frac{2\pi n_{eff-Si}}{\lambda}$, and $\beta_{eff-SiN} = \frac{2\pi n_{SiN}}{\lambda}$ represent the diffracted/incident wavenumber in the buffer region, the propagation constants of the guided mode in the Si and SiN gratings, respectively. In addition, n_{Buffer}, n_{eff-Si}, and $n_{eff-SiN}$ are the refractive indices of the buffer layer, the effective index of Si grating, and SiN grating regions, respectively. α is the incident/diffracted angle in the buffer region which is assumed to be 8 ° for the initial guess to reduce the back-reflection into the waveguide caused by second-order reflection of the grating [32]. Considering the dimensions of the films and their corresponding effective refractive indices in the grating regions at free-space wavelength of $\lambda = 1550\ nm$ (i.e., $n_{eff-si} = 2.77$, and $n_{eff-SiN} = 1.58$), initial periods of $\Lambda_{Si} = 600\ nm$ and $\Lambda_{SiN} = 1200\ nm$ for Si and SiN gratings have been chosen, respectively, both with 50% duty cycle. The GA with a population size of 10 (for each generation) was exploited to achieve geometrical optimization for both gratings in initial steps. As the growth rate of the coupling efficiency is reduced (i.e., as we get closer to the optimum solution), the geometrical parameters of only one grating is changed in each step and alternated between the two gratings in subsequent steps. This approach divides the overall search space dimension (originally 84-dimensional space) into two separate 48- and 36-dimensional spaces, which in turn helps to reach convergence in a shorter time. The GA process is finalized when the growth rate in coupling efficiency becomes negligible (i.e., less than 0.01% per 20 generations).

Table 1: Optimized gap/bar dimensions (in *nm*) for the double-mirror interlayer grating coupler obtained through GA.

Cell	1	2	3	4	5	6	7	8	9	10	11	12	13	14	15	16	17	18	19	20	21	22	23	24
Si Layer Grating																								
Gap	299	209	239	333	261	344	391	288	272	303	297	252	267	352	336	277	348	273	333	361	260	322	336	266
Bar	236	476	341	320	313	207	299	298	384	209	370	281	424	186	360	230	391	240	329	257	354	290	284	1000
SiN Layer Grating																								
Gap	528	753	520	886	493	445	570	601	819	687	660	800	499	596	557	682	729	634	Displacement 2206 *nm*					
Bar	1000	714	497	657	401	45	1172	571	570	320	608	426	483	408	824	579	414	445						

Table 2: Optimized gap/bar dimensions (in *nm*) for the single-mirror interlayer grating coupler obtained through GA.

Cell	1	2	3	4	5	6	7	8	9	10	11	12	13	14	15	16	17	18	19	20	21	22	23	24
Si Layer Grating																								
Gap	338	223	257	359	283	323	407	302	256	292	327	185	239	306	299	286	268	308	353	308	252	304	328	301
Bar	225	417	351	264	319	249	297	260	384	200	387	386	479	172	339	308	360	260	367	242	354	351	222	1000
SiN Layer Grating																								
Gap	597	755	648	1046	634	371	651	605	786	664	660	780	485	637	562	725	733	727	Displacement 1192 *nm*					
Bar	1000	650	378	695	164	32	1229	406	413	524	606	470	531	420	728	571	304	435						

The reward function is estimated for all individuals in the population by invoking a two-dimensional (2D) electromagnetic solver implemented using the finite element method (FEM) for the structure in Figure 15(b). The Wave Optics module in COMSOL software is used for this purpose. To achieve adequate accuracy, a rather fine mesh size (maximum mesh size is set to 1/20th of the wavelength in each region) is incorporated to discretize the geometry. The input port waveguide on the Si layer is excited with a TE (i.e., electric field parallel to the plane of Si or SiN layer) electromagnetic field featuring a matched spatial profile with that of an unperturbed ridge waveguide. The outcoming optical power from the top SiN ridge waveguide was then monitored and the coupling efficiency was calculated simply by dividing the output power at the SiN terminal waveguide to the input power of the Si waveguide (see A and B in Figure 16(a), respectively). In FEM simulations, the refractive indices of 3.46, 2.00, and 1.44 for Si, SiN, and SiO_2 layers are assumed, respectively. The metallic reflectors were also modeled by assuming a complex refractive index of $0.55+11.5i$ associated with gold [33].

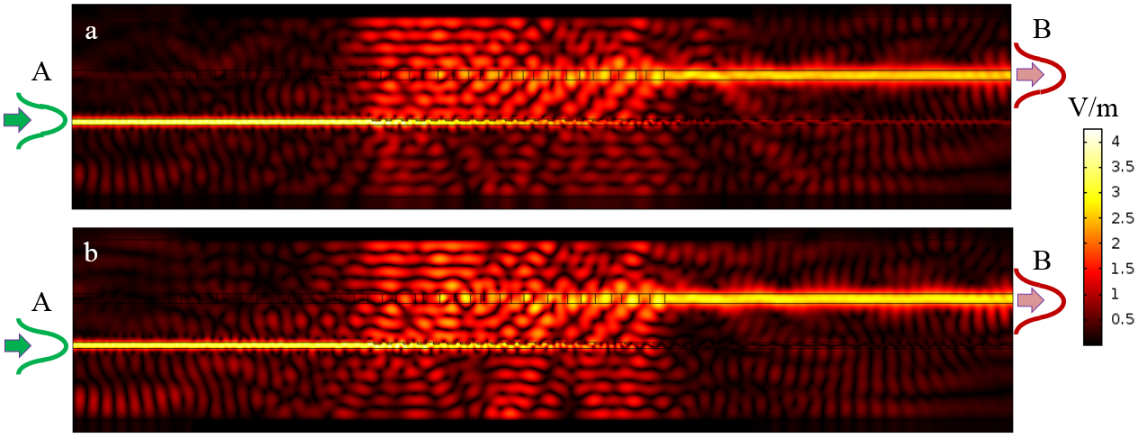

Figure 16: The magnitude of TE field in the optimized structure for (a) the single-mirror and (b) the double-mirror interlayer grating coupler obtained through 2D-FEM simulations at the telecommunication wavelength (1550 nm). The input terminal of the Si ridge waveguide (Point A) is excited by the TE mode of the waveguide, and the output power is calculated in the SiN waveguide after the grating (Point B). In the figure, brightness indicates relative magnitude.

The outputs of the GA, i.e., groove sizes (gap) and their relative positions with respect to the next groove (bar) are compiled in Tables 1 and 2 for structures comprising the double- and single- (i.e., top side) metallic reflectors, respectively. The single reflector structure has only one metallic plate on the top (i.e., the bottom metallic reflector in Figure 15(a) is not present). The relative displacement of the gratings in two layers (i.e., the edge of the leftmost grooves, see Figure 15(b)) is also provided in each case. These results are associated with peak coupling efficiencies of 89% (double-mirror) and 64% (single-mirror) for excitation wavelength of 1550 *nm*. The corresponding electric-field profiles for the single-mirror and double-mirror grating coupler are also shown in Figures 16(a) and 16(b), respectively.

Although the realization of structures featuring backside metallic reflectors entails more complexity in terms of fabrication, simulations suggest that the additional bottom reflector can significantly enhance the coupling efficiency, which is worthwhile in applications with tight constraints on the insertion loss. To estimate the bandwidth of the interlayer coupler, FEM simulations were performed for the optimized structure for wavelengths ranging from 1510 *nm* to 1590 *nm*. The frequency responses of the two structures are shown in Figure 17(a). This simulation predicts a 25% wider 3-dB bandwidth of 50 *nm* for single-mirror grating coupler as compared to the 40 *nm* bandwidth for the double-mirror grating coupler.

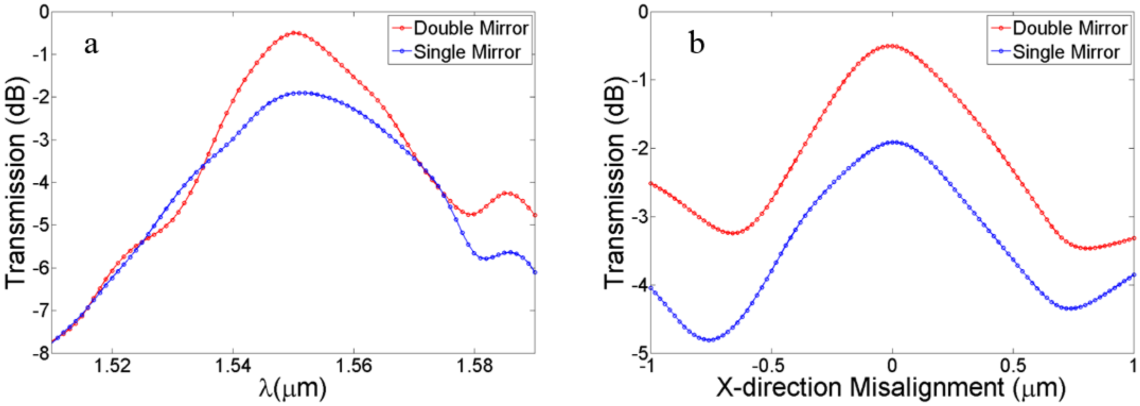

Figure 17: (a) Calculated frequency response of the optimized interlayer grating coupler with single/double metallic mirrors obtained through FEM simulations; (b) Effect of X-direction misalignment of the SiN grating on the insertion loss for the optimized single-/double-mirror grating couplers. The geometrical parameter of the two structures are those listed in Tables 1 and 2.

In practical situations, misalignment between different layers of the coupler is inevitable and depending on the used lithography technology, the misalignment can range from less than 10 *nm* (e.g., in electron-beam lithography) to 1-2 microns in worst cases (e.g., in photolithography). Results shown in Figure 17(b) predict a similar oscillatory behavior in the insertion loss for both structures as the misalignment varies, and indicate that a maximum penalty of about 3 dB can be imposed on the coupling efficiency for misalignments up to ±0.5 μm.

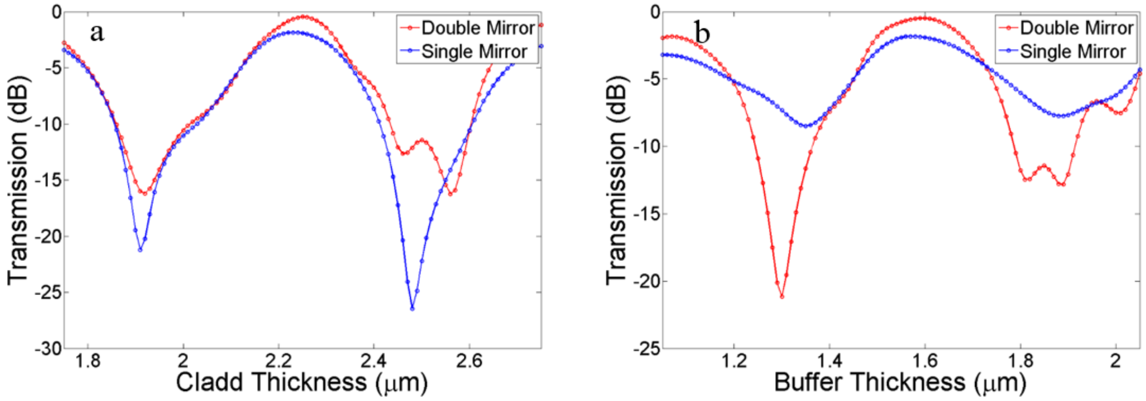

Figure 18: Variations of the insertion loss with respect to (a) the cladding layer thickness, and (b) the buffer layer thickness in Figure 15(b) calculated for 1550 nm wavelength. The parameters of the two structures are the same as those in Tables 1(a) and 1(b).

The effect of variations in the cladding and buffer thicknesses on the insertion loss are also investigated at 1550 nm wavelength and the results are shown in Figures 18(a) and 18(b), respectively. Oscillations seen in Figures 18(a) and 18(b) are attributed to the vertical Fabry-Perot resonator formed by stacked materials on top of each other with different refractive indices. The change in the total optical length of the vertical cavity can also lead to a shift in the peak transmission wavelength. Figure 18 shows that for operation in the efficient coupling regime, a thickness variation of about ±5% (i.e., ±0.1 μm) can be tolerated.

3.3 Fabrication Steps

The 3D structure in Figure 15(a) can be fabricated using two different approaches. The first approach is based on bonding (either flip chip or direct bonding) of the appropriate commercially available SOI (from SOITECH) and SiN on oxide (from Rogue Valley) wafers. In this process, lithography and etching are performed on the SOI and the SiN substrates separately, and the two substrates are then aligned and bonded together. The second approach is to start with an SOI wafer and fabricate the desired structures in Si. In the next step, the buffer oxide and SiN layers are stacked through deposition and the patterns are defined/etched on the SiN layer after careful alignment with the waveguide in the Si layer. In the last step, the cladding (SiO_2) layer is deposited on top of the SiN device layer. The top and the bottom metallic mirrors in both approaches can be readily realized through metallization/liftoff and backside etching/metallization of the device, respectively. In this work, the latter approach is used due to the higher yield, simplicity, and the better quality of the final 3D structure without requiring sophisticated processes. I also focus only on demonstration of single-mirror (top mirror) couplers. A brief pictorial representation of the fabrication process is shown in Figure 19. In the fabrication process, I start with a commercial SOI wafer (from SOITECH) with a 3 μm BOX layer and a 250 *nm*-thick device Si layer.

Since there exist a 160 *nm*-thick pedestal for the grating structure on the Si layer, fabrication of the waveguide, the resonator, and the grating structure on the Si layer requires two separate etch steps with different etch depths. The first step includes electron-beam lithography (EBL using a JEOL JBX-9300FS system) and inductively coupled plasma (ICP) etching with Cl_2 chemistry with an etch depth of 90 *nm* to partially form the waveguide and resonator and completely form the 90 *nm*-deep grating grooves. The electron-beam resist in this step is HSQ (6% from Dow Corning). In the second step, EBL with ma-N 2400 (Micro Resist Technology) as the resist is used to cover the grating and perform ICP etching using Cl_2 chemistry for another 160 *nm* to complete the fabrication of all Si-layer devices. In addition to the desired devices and gratings, alignment markers are fabricated in the Si layer (250 *nm* etch depth) to facilitate the alignment of the devices in the Si and SiN layers in subsequent steps.

Before depositing the buffer oxide layer, I had to planarize the surface of the chip

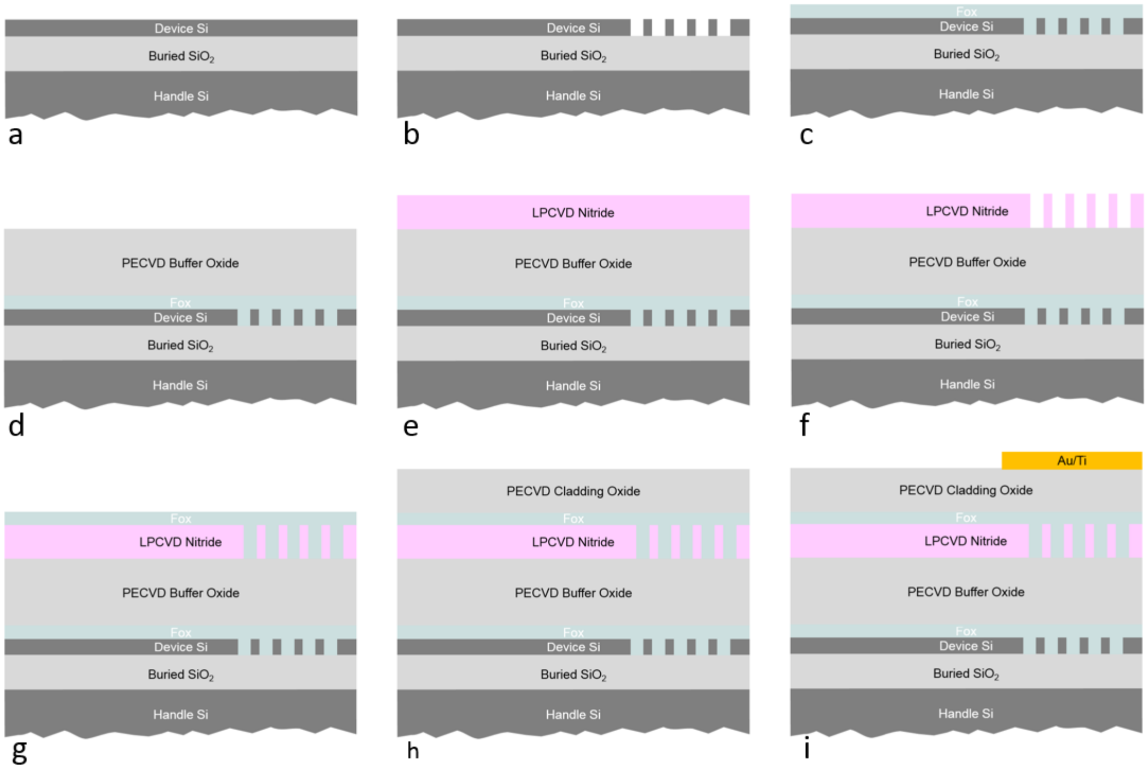

Figure 19: Pictorial summary of the fabrication flow of the interlayer grating coupler for the Si/SiO_2/SiN platform.

by spin-coating a 700 *nm*-thick flowable oxide (FOX 16% from Dow Corning) followed by a pre-bake at 300 °C for 3 minutes (on a hotplate) and anneal at 900 °C for 2 hours (in a furnace with oxygen environment). The high temperature annealing step shrinks the film thickness down to 550 *nm*. Afterward, plasma-enhanced chemical vapor deposition (PECVD) is used to deposit further SiO_2 to reach the buffer thickness 1600 *nm* measured from the top of the Si waveguide. In the next step, a 400 *nm* thick SiN layer is deposited in an LPCVD furnace at 800 °C (dichlorosilane to ammonia ratio of 0.35). The gas ratio is chosen to prevent the formation of stress-induced cracks in the SiN film. Note that the SiN deposition recipe is optimized for a fixed buffer SiO_2 thickness (i.e., 1.6 μm). In Figure 20, typical crack formation on the SiN layer is shown for three different SiO_2 thicknesses, i.e., 1.6 μm, 3 μm, and 5 μm. Three representative points on the sample are shown for each deposited film thickness. As seen in Figure 20, thicker SiO_2 layers result in crack formation as a consequence of higher stress levels on the SiN layer.

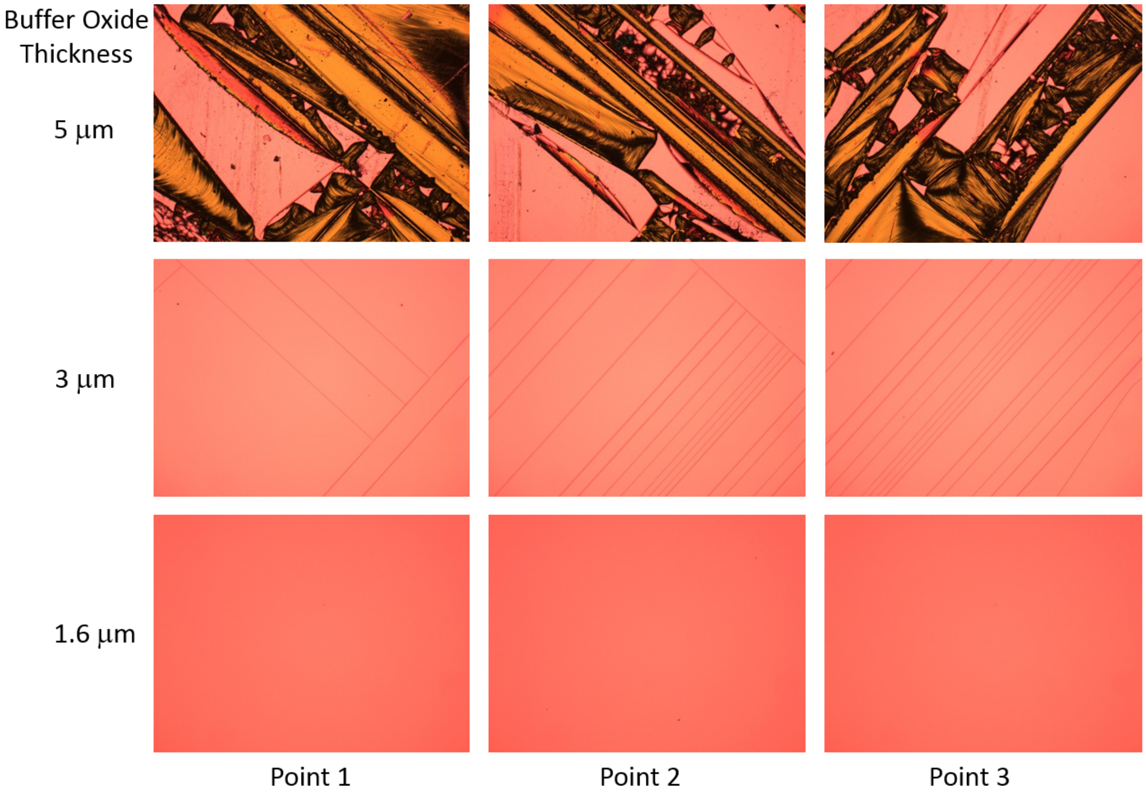

Figure 20: Typical crack formation (shown at three different points) on a 400 *nm*-thick SiN film deposited through LPCVD on a buffer layer of SiO_2 with three different thicknesses, i.e., 1.6 *μm*, 3 *μm*, and 5 *μm*.

The grating along with the waveguide/resonator masks on the SiN layer are defined through EBL using a 500 *nm* thick positive tone electron-beam resist (ZEP from ZEONREX Electronic Chemicals) featuring a good etch selectively (≈ 0.5) in CF_4/CHF_3 chemistry. To prevent misalignment due to the charge-up issue during EBL on such insulating layers, the sample is coated with an anti-charging water-soluble solution (ESPACER from Showa Denko). Also, the SiN and SiO_2 layers over the alignment marks are selectively etched to facilitate the alignment process. The sample is then etched in a reactive ion etching (RIE) chamber ($CF_4 = 50$ *sccm*, $CHF_3 = 5$ *sccm*) for 400 *nm* and cladded with a 2.25 micron PECVD SiO_2 layer after it was planarized in a similar way explained earlier.

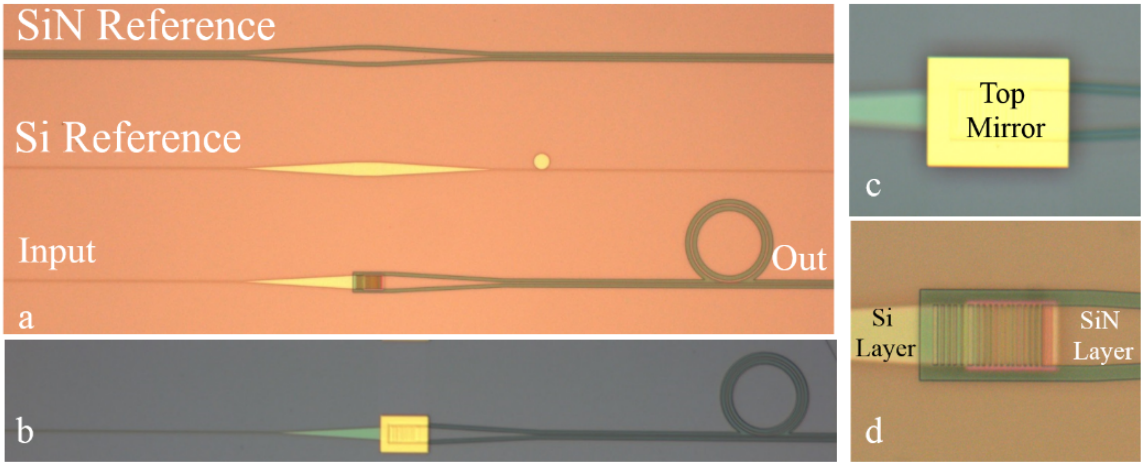

Figure 21: (a) Optical micrograph of the fabricated devices before metallization step including: (top) SiN reference waveguide, (middle) Si reference waveguides coupled to a microdisk, and (bottom) connected Si/SiN waveguides through an interlayer grating coupler. (b) Optical micrograph of the interlayer grating coupler with a top metallic mirror (10 *nm* Ti adhesion layer along with 100 *nm* gold).

Figure 21(a) shows the optical micrograph of the device after cladding deposition. In the final step, the top mirror is defined though metal evaporation (10 *nm* Ti, 100 *nm* Au) on top of a 600 *nm* patterned PMMA (from MICROCHEM) and the subsequent liftoff process. In my design, 12 μm wide gratings on Si and SiN layers are laterally connected to 500 *nm* and 1.3 μm wide waveguides, respectively, through 100 μm long linear tapers (see Figure 21). A similar back-to-back linear taper is included in the middle of reference waveguides on both the Si and the SiN layers. The dimensions of both waveguides are chosen to ensure single TE-mode operation. The waveguide on the SiN layer is point-coupled (500 *nm* gap) to a 2 μm wide microring with outer radius of 35 μm (the device is shown at the bottom of Figure 21(a)). Also a 7 μm-radius microdisk with both TE and TM modes was placed 180 *nm* away from the Si reference waveguide (the device is shown in the middle of Figure 21(a)). The transmission characteristics of this structure is used to adjust the input polarization to make sure the on-chip polarization is the desired one. Waveguides on both layers are extended at both sides for a few millimeters without tapering. Access to waveguide facets is made possible by cleaving the sample at both sides perpendicular to the waveguides.

3.4 Characterization Results

To characterize the device, the output light of a tunable laser (Agilent 81682A) is launched into a lensed single mode fiber through an in-line polarization controller. The fiber is mounted on a stage equipped with XYZ micro-positioners as well as a rotation/tilt compensator. The fiber is then aligned so that its outcoming light is focused on the input facet of the integrated waveguide in the desired (Si and SiN) layer. The output light from the chip is collected at the output facet with a similar lensed fiber and fed directly into a detector (Thorlabs PDB150C 800 $nm - 1700$ nm). The transmission spectrum of the device along with reference waveguides were then obtained by sweeping the laser wavelength from 1460 nm to 1530 nm. To adjust the state of polarization of the incoming laser light, fibers are first aligned with the Si reference waveguide facet; and the in-line polarization controller is adjusted so that the TM resonance modes of the microdisk in the Si layer are suppressed in the output (i.e., TM modes are not excited through the coupled Si waveguide). Once the TE polarization is set, the transmission spectrum of the desired devices on the chip are characterized by measuring the optical power in the output fiber for each device. To minimize the effect of fiber to waveguide coupling variation (caused by possible misalignment), the alignment is repeated several times to make sure maximum coupling is achieved at a fixed wavelength (i.e., 1470 nm). With the described measurement setup, the total fiber-to-fiber insertion loss comprises coupling losses of fibers and waveguide facets (at both input and output of the chip), waveguide scattering loss, reflection/scattering loss of the tapered regions, and interlayer grating couplers. Assuming similar fiber/facet alignment for all waveguides and the same propagation losses in the waveguides, the coupling efficiency at the grating coupler can be estimated by comparing its corresponding fiber-to-fiber insertion loss with that of the reference waveguide structures on the Si and SiN layers.

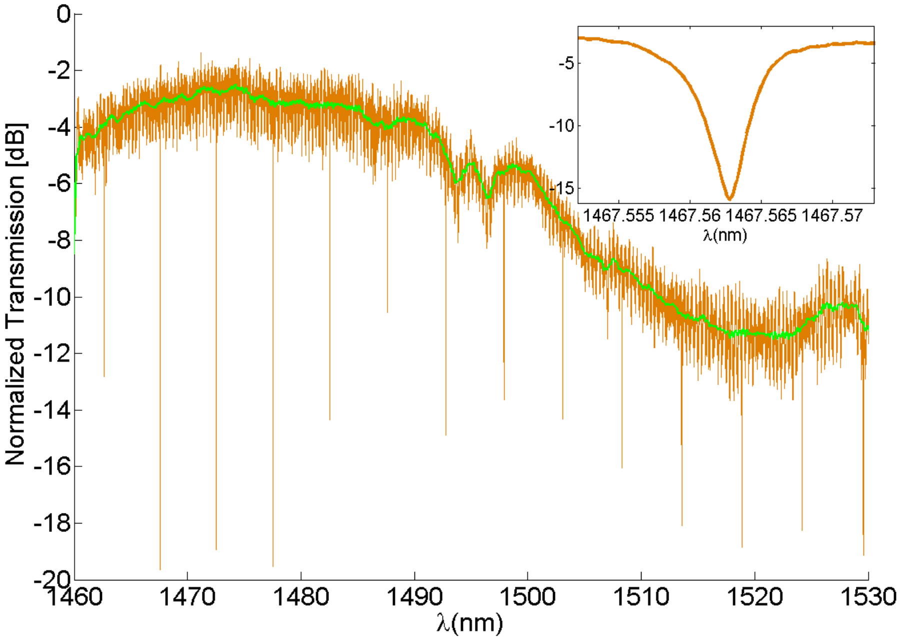

Figure 22: Normalized transmission spectrum of the interlayer grating coupler embedded at the intersection of the Si/SiN waveguides. Sharp resonances (loaded-Q of $150k$) are related to the coupled microring cavity on the SiN layer. The green curve is the averaged transmitted power.

Figure 22 shows the normalized TE transmission spectrum of the interlayer grating coupler. The observed shift (relative to the design value) on the peak transmission wavelength of the interlayer grating coupler response is believed to be due to both thickness variations of the deposited layers and the scaled dimensions of the grating grooves. While the former effect was observed during fabrication, the latter is probably due to non-optimized EBL dosage in defining the grating grooves in the Si and the SiN layers. Figure 22 clearly shows the wideband transmission spectrum of the interlayer grating coupler (3-dB bandwidth of at least 40 nm with peak transmission wavelength of around 1470 nm). The sharp resonance signatures in the transmission spectrum (Figure 22) are related to the coupled ring resonator on the SiN layer. The

Lorentzian lineshape of the resonance around 1467.5 nm (inset of Figure 22) shows a loaded-Q of around $150k$.

To estimate the coupling efficiency of the interlayer gating couplers at 1470 nm wavelength, I use the measured transmission of the Si reference waveguide, the SiN reference waveguide and the Si/SiN structure with the grating coupler, which are -27.78 dB, -14.77 dB, and -23.10 dB, respectively. The difference (≈ 13 dB) in the detected signal levels for the Si and SiN reference waveguides is attributed to the different facet dimensions (500 $nm \times 250$ nm for Si and 1.5 $\mu m \times 400$ nm for SiN) as well as the higher refractive-index mismatch for the Si waveguide, which is in agreement with the modal overlap calculations. Assuming the grating to be in the middle of the Si/SiN structure, the respective transmission from the Si and the SiN waveguide section in the structure can be estimated at $-27.78/2 = -13.89$ dB and $-14.77/2 = -7.38$ dB, respectively. Thus, the overall transmission of the waveguide section of this structure is $-13.89 + (-7.38) = -21.27$ dB. Comparing with the overall -23.10 dB transmission, -2.03 dB is attributed to the transmission of the single-mirror interlayer grating coupler. This corresponds to a coupling efficiency of $\approx 63\%$ that agrees well with the theoretical calculations (64%). Note that by adding the second mirror on the bottom layer, the efficiency is expected to increase to 89% in the optimized device. This is the highest coupling efficiency over a large bandwidth (> 40 nm) in a Si/SiN hybrid structure reported to date. The coupling structure reported here can facilitate the realization of functional devices in hybrid CMOS-compatible material platforms.

CHAPTER IV

TUNABLE INTEGRATED PHOTONIC DEVICES

4.1 Need for Tuning/Trimming

Despite all the shortcomings of Si in optics, silicon-on-insulator (SOI) seems to be the platform of choice for integrated applications. This is mainly due to the low mass-manufacturing cost promised by the CMOS technology that has already been developed around Si. Other high-refractive-index materials such as SiN (as detailed in Chapter 3), as well as III-V compound semiconductors have also been combined with silicon to enrich the functionalities of Si-based platforms. Compared to most electronic devices, the specifications of photonic devices heavily depend on the geometrical dimensions of the device structure. This sensitivity is even higher for devices that are fabricated on material platforms featuring high refractive index contrast.

In most integrated photonic applications (ranging from optical filters to lasers), optical resonators play a key role in meeting the goals of the overall system. However, optical characteristics of such elements, specifically their resonance wavelength, depend heavily on the optical path length and are hence vulnerable to fabrication tolerances. To study the sensitivity of a typical microcavity to fabrication imperfections, the shift in the resonance wavelength of a silicon-based microdsik cavity (3-μm radius) as a function of dimensional variations (in both radius and thickness) is obtained using FEM simulations.

As seen in Figure 23, this study indicates that ± 4 *nm* shift in the resonance wavelength should be expected for ± 10 *nm* deviations in the radius. Also, it is seen that similar deviations in the thickness of the microcavity will result in even larger shifts (by a factor of ≈ 3) in the resonance wavelength. This issue is more consequential in photonic systems featuring more than one optical microcavity, e.g., in high-order sharp optical filters, in which the proper functionality of the system relies on the precise control of each and every resonant mode and their relative spacings.

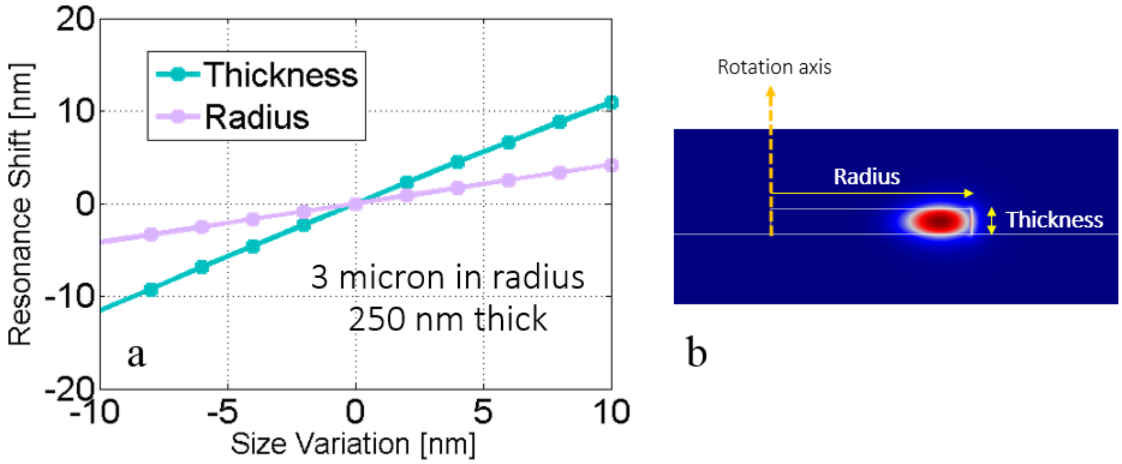

Figure 23: (a) Shift in resonance wavelength of a 3-micron radius microdisk cavity as a function of dimension variations due to fabrication imperfections. (b) The geometry of the microcavity superimposed by its optical mode.

For this very reason, in almost all practical cases, the use of a mechanism which accommodates either post-fabrication trimming or, alternatively, continuous tuning is highly desired and sometimes inevitable. This goal can be achieved by tuning the optical properties (in particular the refractive index) of the material in use. Such tuning capability is of immense engineering significance since it allows designing reconfigurable systems that can perform numerous functionalities. In Sections 4.2 and 4.3, the available mechanisms to achieve tuning and trimming in optical materials are briefly introduced.

4.2 Tuning and Trimming Mechanisms

The refractive-index tuning methods are based on either the thermo-optic effect (for almost all optical materials) or the carrier dispersion property of optical materials (mostly for Si). The refractive index of most optical materials is sensitive to the temperature. The strength of this temperature dependence is reflected in the so-called thermo-optic coefficient. As an example the thermo-optic coefficient of Si is roughly five times higher than that of SiN in telecommunication wavelengths ($1.86 \times 10^{-4} K^{-1}$ for Si versus $4 \times 10^{-5} K^{-1}$ for SiN). In integrated applications, micro-heaters are usually used to locally increase the operation temperature of photonic devices. This approach can easily increase the average temperature of the device by more than 100 °C. It is clear that the speed at which the device can be tuned depends on how fast the device can be heated up, which is governed by the heat transport equation. In solids, the main mechanism for heat flow is the heat conduction. It can be shown that the transient heat conduction in three-dimensional structures takes the following form:

$$\rho c \frac{\partial T}{\partial t} - q_s = \bigtriangledown \cdot (k \cdot \bigtriangledown T). \tag{27}$$

In Equation 27, q_s, k, c, and ρ are the heat density (generated by the source), the thermal conductivity of the material, the specific heat capacity and the mass density, respectively. Although the mass density of most optical materials is in the same range, their heat capacity and thermal conductivity can vary significantly. For example, the numerical values for three of the mostly-used optical materials (i.e., Si, SiO_2, and SiN) are tabulated in Table 3 (the values are for bulk material)[34, 35].[1] Although the optical device geometry and the microheater structure can be optimized for fast tuning, usually the rise and fall times for the thermal-based tuning approaches are in the μs range.

Table 3: Thermal properties of few optical materials

Material	$\rho (kg/m3)$	$c(J/kgK)$	$k(W/mK)$
Si	2330	703	163
PECVD SiO_2	2203	650	1
LPCDV SiN	2500	170	20

---

[1] Since the thickness of Si in most integrated optical devices is comparable to the mean free path of phonons, the effective thermal conductivity should be used.

As mentioned earlier in this section, the modification of the concentration of free carriers, i.e., the density of electrons and holes, in a semiconductor can alter the refractive index property of the material. Permanent extrinsic carriers can be introduced in semiconductors by implanting donor or acceptor species through ion implantation. Alternatively, one can use carrier injection or depletion in pn-junction structures, and accumulation in capacitive structures to alter the concentration of the carriers. This approach provides a much faster means to tune optical devices. The rise and fall times in the ns range is readily achievable. However, in addition to the refractive index change, the introduction of extrinsic free carries gives rise to a significant optical loss in the material through the free-carrier absorption mechanism. This loss is the main prohibitive factor that limits the capability of this method for achieving wide tuning ranges. In almost all practical cases the change in the refractive index as a result of carrier dispersion is much smaller than that achievable through thermal tuning. For this reason, carrier dispersion does not provide a practical way for cases where large tuning is desired.

4.3 Passive Trimming

Although the microheater-based tuning mechanism is reliable for most practical cases, it accounts for the largest share of power consumption (electrical) in integrated photonic devices. As an example, in a typical resonance-based EO modulator, the electrical power for actual modulation is an order of magnitude smaller than that required to tune the wavelength of operation. This considerable overhead in the power consumption is not desirable and needs to be reduced or totally eliminated. Passive post-fabrication trimming methods offer permanent solutions to adjust the parameters of the structure with no power penalty. The use of UV-sensitive as well as electron-beam-sensitive polymers in trimming of microring resonators has been demonstrated with a rather wide trimming range [36, 37]. However, due to their lack of compatibility with high-temperature processing and also short-time durability (aging), the use of such polymers is not possible for many applications. Fine tuning techniques based on controlled local oxidation, such as electric-field-driven oxidation or laser-assisted oxidation, have also been developed and demonstrated specifically for silicon-based devices. A similar approach is shown to be effective for silicon nitride substrates where trimming is accomplished by converting stoichiometric SiN to oxynitride through oxygen-plasma treatment [38, 39, 40]. Nevertheless, it seems that oxidation-based trimming usually comes at the expense of quality-factor degradation. Compaction through UV irradiation and electron-beam exposure for both silicon dioxide and silicon nitride has shown to be feasible and has been exploited for various applications, including waveguide formation, strain exertion, as well as trimming [41, 42, 43]. Although most post-fabrication trimming methods offer discrete trimming, they can still be used to reduce the unintended mismatch between the fabricated and the designed specification (usually the resonance wavelength) within their precision limit. The exact match can be reached by adding an active trimming mechanisms such as the thermal-based tuning method. In this scenario the required trimming power is much lower compared to the case for which only the thermo-optic effect is in use.

As briefly mentioned above, electron-beam exposure allows for passive trimming of photonic devices. The trimming effect due to electron-beam exposure results from two related mechanisms, i.e., compaction-induced and stress-induced refractive index change. Since SiO_2 is usually used as the cladding material for many integrated photonic devices, compaction-induced refractive index change in this material can be harnessed for trimming purposes. Aside from this effect, the compacted cladding layer exerts a new stress profile on the device layer. Depending on the details of the compacted layer, this stress profile could be tensile, compressive, shear, or a combination of all. This highly geometry-dependent stress can locally modify the refractive index of the device layer (e.g., Si) according to the stress-optic relations [44, 45].

In the following, the efficacy of the electron-beam exposure for post-fabrication trimming is studied. For this study, an array of microdisk resonators (6 μm in radius) are fabricated on a multilayer platform. The device layer of the platform comprises a 110 nm-thick Si, a 70 nm-thick SiO_2 layer, and a 110 nm-thick Si layers which are vertically stacked on top of each other. The device layer sits on top of a 3 μm-thick buried oxide. The resonators are covered by a 1 μm-thick layer of SiO_2 deposited through the plasma-enhanced chemical vapor deposition technique. The fabrication is done through standard electron-beam lithography and plasma etching steps. The devices are optically characterized in a thermally-stable environment (to suppress the thermo-optic effect) and the resonance wavelengths of each microdisk cavity are recorded.

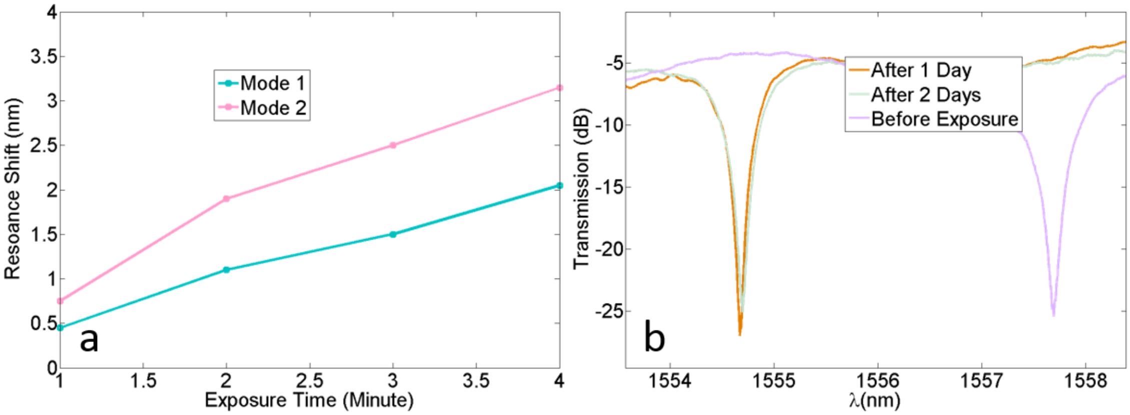

Figure 24: (a) Shift in resonance wavelength due to electron-beam exposure for for the first two radial modes of a 6 μm radius microdisk. (b) Transmission spectrum of the device before exposure (violet curve) to the electron beam, after one day of exposure (brown curve), and after two days of exposure (green curve).

In the next phase of the experiment, a scanning electron microscope (Zeiss Ultra60 FE-SEM) is used to expose the microresonators to a 118 pA electron-beam current (with extra high tension voltage set at 20 kV). The effect of electron-beam dosage is investigated by varying the exposure time from one minute to four minutes in one-minute steps. After exposure, the microresonators are characterized and the resonance wavelengths are compared with the corresponding pre-exposure values. In all cases, a blue shift is observed in the resonance wavelength. This is at odds with the previous reports in which red shifts in the resonance wavelength are observed [43]. As explained earlier, the exposure-induced stress profile is highly geometry dependent. This disparity likely stems from the geometrical differences in microrings (in the work reported by Schrauwen, et al. [43]) and microdisks (in my experiment). In Figure 24(a), the absolute wavelength shift for the first two radial modes of the resonator are shown. It is evident that longer exposure times result in larger shifts in the resonance wavelength for both modes. To ensure that the trimming effect of the electron-beam exposure is not ephemeral, the optical characterization is repeated one and two days after the exposure was carried out. In Figure 24(b), the collected transmission spectra of a representative device is shown. The plot in violet shows the transmission spectrum of the device before exposure. The plots in brown and green are the collected spectra after one and two days of exposure, respectively. As seen in figure 24(b), the drift in the resonance wavelength after 48 hours is negligible.

In summary, wavelength trimming up to 3 *nm* is shown to be readily achievable through electron-beam exposure for microdisk cavities fabricated on multilayer material platforms. This post-fabrication trimming method can be used in conjunction with microheater-based tuning approach to drastically reduce the overall power consumption of tunable photonic systems.

CHAPTER V

COMPACT HIGH-SPEED ELECTRO-OPTIC MODULATOR

5.1 Overview

The staggering growth rate of data traffic within datacenters has posed a serious challenge for conventional electrical interconnection systems. Over the past few years this challenge has been the main driving force behind the development of a more capable technology, which is suitable for such short-reach applications. Integrated photonics is the most promising candidate offering an unparalleled solution to tackle the electrical interconnect bandwidth inadequacy. One of the key elements (other than the laser source and the photoreceiver) in an integrated photonic transceiver is the electro-optic (EO) modulator, which determines the ultimate achievable data rate in the communication link. For this reason, extensive research has been aimed at developing reliable, compact, low-power, and high-speed EO modulators that can be deployed at a reasonable cost. The existing low-cost silicon (Si) manufacturing ecosystem and the potential for monolithic integration with electronic integrated circuits have been the prime motivations for directing most of such research efforts towards the Si photonic platform. Carrier dispersion offers a fast way to change the optical properties of Si, in particular its refractive index and optical absorption [46]. Carrier injection and depletion in a pn-junction device [47, 48] and carrier accumulation in a capacitive device [49, 50] are among the main mechanisms by which the carrier concentration in Si can be altered in a short time ($< 0.1\ ns$). In contrast to injection mechanism in which the lifetime (τ_c) of the excess (minority) carriers limits the speed of the process, the relaxation time of the electric circuit ($\tau = RC$) plays the deciding role in the charge dynamics in cases of depletion and accumulation mechanisms [51, 52]. Since it is rather easy to engineer the RC of the device such that $\tau << \tau_c$, most of the current studies for high-speed EO modulation applications are focused on the depletion mechanism in devices with a reverse-biased pn-junction [53]. In a typical reverse-biased pn-junction-based modulator (with an abrupt doping profile at the junction) the junction capacitance (C_j) and resistance (R) of the device are mainly controlled by the doping levels (N) on the p and n regions such that $R \propto N^{-1}$ and $C_j \propto N^{1/2}$. In comparison to the depletion mechanism, the carrier accumulation mechanism (which is implemented by forming a capacitor with two Si layers separated by a thin dielectric layer) is less explored. A particularly noteworthy feature of the accumulation-based devices compared to their depletion-based counterparts is that the capacitance-per-area ($C = \epsilon_r \epsilon_0 / t_o$, with ϵ_r and to being the relative permittivity and thickness of the dielectric layer of the capacitor) of the structure can be readily designed by choosing the dielectric material (i.e., ϵ_r) and thickness (t_o), which are independent from the doping levels of the two Si electrodes. The flexibility in the choice of C allows for designing structures featuring extremely low-voltage (i.e., by choosing a large C) and or extremely high-speed (i.e., by choosing a small C) operation performance. A few EO modulators based on the accumulation mechanism have been demonstrated in resonance and interferometric architectures featuring an embedded metal-oxide-semiconductor (MOS) capacitor and operation speed of up to $3Gb/s$ [49, 50]. In these structures, a doped poly-Si (p-Si) layer is used as the top gate-electrode and a crystalline Si layer (separated by a dielectric layer) serves as the second electrode. In general, the use of p-Si in integrated optical devices is not desirable, since the scattering loss from the p-Si grain boundaries significantly affects their performance. Most notably the scattering loss degrades the quality factor (Q) of compact resonance-based devices. In this work, a Si/SiO$_2$/Si multilayer material platform featuring crystalline Si layers is used to demonstrate a wideband (> 10 GHz) accumulation-based modulator. The crystalline Si layers allow us to achieve a compact and low-loss (i.e., high-Q) microdisk resonator as the main building block of the device [54]. My accumulation-based device platform can be extended to other optical materials in conjunction with Si in the form of a vertically-stacked heterogeneous structure to enhance the functionality of the overall integrated photonic structure. Such hybrid material platforms have been developed and exploited to demonstrate novel applications beyond the inherent capabilities of Si [22, 55, 56, 21]. In many practical applications, the operational wavelength of the photonic devices needs to be precisely controlled. Unfortunately, in almost all resonance-based devices integrated on high-index-contrast material platforms, the designed resonance wavelength deviates from the actual one due to the fabrication imperfections. The expected level of accuracy in resonance wavelength is invariably dictated by the precision of the fabrication technique in use. For example, the variation in resonance wavelength of a 4 μm-radius microdisk in the silicon-on-insulator (SOI) platform for operation around $\lambda = 1550$ nm can be as large as 0.5 nm [57]. To rectify this mismatch, both active and passive trimming techniques have been developed [58, 59, 42, 43]. Due to their limited precision, passive trimming techniques have limited use compared to active approaches. Most of the active trimming techniques rely on the thermo-optic effect, and despite offering continuous trimming (i.e., high precision), they impose a serious challenge in terms of the overall power consumption of the device. I have previously shown that the resonance wavelength of a fabricated microdisk resonator on the Si/SiO$_2$/Si multilayer platform can be trimmed (i.e., corrected) by up to 1 nm (which is adequate for almost all practical applications) by applying a dc voltage between the two Si layers [56, 60]. The unique self-trimming feature of this modulator is of great technological importance as it obviates the need for implementation of thermal-based trimming techniques; this in turn significantly reduces the overall power consumption of the device. In Section 5.2 the architecture of my high-speed EO device is introduced. In Section 5.3, details on the corresponding fabrication processes are provided. Characterziation results are discussed in Section 5.4. Finally, in Section 5.5, the possible extension of this work is briefly discussed to achieve higher data rates through spectral efficient modulation formats.

5.2 Design

The cross-section of the EO modulator device studied in this section is shown in Figure 25(a). The device comprises a small microdisk (radius $(r) = 3\ \mu m$) optical resonator, a 450 nm wide access waveguide, and two focusing grating couplers, which are fabricated on a multilayer Si/SiO$_2$/Si platform. The thickness of the top and bottom Si layers is 110 nm each, and the middle SiO_2 layer is 70 nm thick (t_o). The access waveguide is placed 150 nm away from the microdisk to achieve near-critical-coupling through evanescent excitation. A 50 nm thick Si pedestal underneath the device provides access to the bottom Si layer for adding electrodes. The top and bottom Si layers are moderately doped ($\approx 10^{18}\ cm^{-3}$) to reduce their electrical resistivity. Regions underneath the electrical contacts are heavily doped ($\approx 10^{20}$ cm^{-3}) to achieve low contact resistance with Si. The cross section of the doping profile on the microdisk and the pedestal is shown in Figure 25(b). The electrodes are deliberately placed far from the first radial whispering gallery mode of the microdisk to ensure negligible propagation loss due to metallization (see Figure 25(b) and 25(c)). The electric-field profile of the first radial TE mode of the microdisk (shown in Figure 25(c)) is obtained numerically using a commercially available finite-element-method (FEM) software package (COMSOL). The two Si layers and the sandwiched SiO$_2$ layer in between form a capacitor, which extends all over the microdisk area ($A = \pi r^2$). Application of a positive voltage (V) between the two metallic electrodes (and thus, between the two Si layers) results in the accumulation of oppositely charged carries on the top and bottom Si layers ($q = C \times V$). As seen in Figure 25(c), the optical intensity of the mode of interest is mainly concentrated within a distance of $d \approx 700$ nm from the periphery of the microdisk and has negligible extent in the central part of the structure. Therefore, accumulated charges on the central part of the capacitor has negligible interaction with the optical mode. To distinguish between these two regions on the microdisk, the total capacitance of the structure (C) can be expressed as the sum of two parallel capacitances, i.e., $C = C_p + C_m$. Here, C_p and C_m denote the parasitic capacitance (central region of the microdisk resonator) and the functional capacitance (region near the periphery of the microdisk with non-negligible optical field), respectively (see Figure 25(b)).

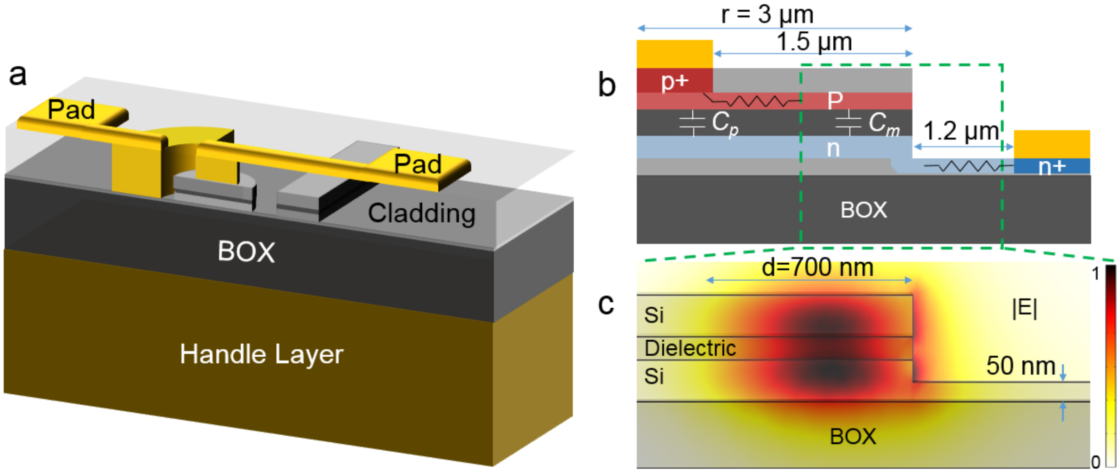

Figure 25: (a) 3D schematic of the cross section of the accumulation-based EO modulator on a multilayer platform. Two focusing grating couplers are connected to the terminating ends of the access waveguide (not shown) to facilitate the input/output light coupling during characterization (b) Cross section view of the designed doping profile on different layers of the device. (c) The corresponding mode profile (magnitude of the electric field) of the first radial transverse electric (TE, electric field parallel to the Si layers) mode of the microdisk resonator obtained around $\lambda \approx 1560$ nm.

The accumulated electrons (ΔN) and holes (ΔP) on the two Si layers around the optical mode (i.e., on the C_m capacitor) shorten the optical path length of the microdisk resonator through carrier dispersion property of Si ($\Delta n = -(8.8 \times 10^{-22} \times \Delta N + 8.5 \times 10^{-18} \times \Delta P^{0.8})$), which ultimately results in a blue shift in the resonance wavelength of the microdisk [46]. The total operation bandwidth (f_{cutoff}) of the EO modulator is determined by the electrical relaxation time constant (i.e., τ_c) of the structure as well as the lifetime of photons in the microdisk resonator (i.e., τ_o) approximately through $(1/f_{\text{cutoff}})^2 \approx (2\pi\tau_c)^2 + (2\pi\tau_o)^2$ relation [61, 62]. If the total electrical resistance of the Si layers, ohmic contacts, and the electrical interconnects are modeled by a lumped series resistor (R), the electrical relaxation time constant will be given by $\tau_c = R \times C$. The lifetime of photons can readily be estimated through the Q of the resonant mode ($\tau_o = Q/\omega$, ω is the optical resonance frequency). Assuming that the switch times of the logic levels in the driving signal are much faster than the electrical response time of the structure (i.e., τ_c), the average power consumption of the device subject to a random bit sequence drive (i.e., equal likely 1-0, 1-1, 0-1, and 0-0 transitions) can simply be estimated through $P = 1/4 \times C \times V^2$ [63, 64]. Note that the elimination of C_p can improve the electrical bandwidth as well as the power consumption of the device by a factor of $r^2/(r^2 - (r - d)^2)$. In the device with the aforementioned dimensions, this factor is approximately 2.42. With the designed dimensions of the microdisk resonator shown in Figure 25, the total capacitance of the structure is estimated to be $\approx 13.9\ fF$ (capacitance per unit area of the multilayer Si/SiO$_2$/Si platform is approximately 0.49 $fF/\mu m^2$ with $\epsilon_r \approx 3.9$). Assuming that the total pad-to-pad resistance (i.e., R) of the structure is dominated by the resistance of the doped Si layers for the microdisk geometry, R can be approximated to be 760 ohm resulting in an estimated τ_c of $\approx 10.6\ ps$ or equivalently an electrical bandwidth of $\approx 15\ GHz$. In comparison, the doping levels in the depletion-based structures are set around 1 2 $\times 10^{18}\ cm^{-3}$ to minimize the free-carrier optical loss associated with the dopants while achieving a decent carrier dispersion effect and low resistance. This choice would result in a junction capacitance of $C_j \approx 2\ fF/\mu m^2$ (assuming an abrupt junction profile) in such structures.

5.3 Fabrication Steps

The designed structure shown in Figure 25(a) is fabricated on a multilayer platform prepared through direct (fusion) bonding [65] of two SOI wafers. In the first step, a thin layer of oxide (with targeted thickness of 35 *nm*) is thermally grown on the device layer of two commercially available Si-on-insulator (SOI) wafers with a 3 μm thick buried oxide (BOX) layer. In the next step the two SOI wafers are bonded together on the thermal oxide side and then the handle layer as well as the buried oxide layer of the top wafer is removed using a dry etching process. The details of this bonding process is explained in Ref. [66] and are not repeated here. The initial thickness of the device layer is chosen such that after oxidation and bonding, the total thickness of the sandwiched oxide is around 70 *nm*, and the thickness of each device Si layer is 110 *nm*. The microdisk resonator, the access waveguide, and the input/output focusing grating couplers are patterned by electron-beam lithography (EBL using a JEOL JBX-9300FS system) with a 190 *nm* thick spin-coated hydrogen silsesquioxane (HSQ) layer (6% from Dow Corning) as the resist. The Si and the oxide layers are then dry-etched in an inductively coupled plasma (ICP) chamber (with Cl_2 chemistry) and a reactive ion etching (RIE) chamber (with Ar and CHF_3 chemistry), respectively. A 55 *nm* thick pedestal is selectively left un-etched around the microdisk on the bottom Si layer through another EBL step using ma-N 2400 (Micro Resist Technology) electron-beam resist. In Figure 26(a), the scanning electron microscope (SEM) image of the access waveguide and part of the microdisk is shown (tilt angle is 45 °. In this image the (false-colored) blue and pink shaded regions correspond to the Si and SiO_2 layers, respectively.

The sample is then conformally coated with a thin (i.e., 10 *nm*) layer of blanket oxide using atomic layer deposition (ALD) to prevent ion channeling in the following ion implantation steps. Five rounds of ion implantation are carried out successively for 1.25×10^{13} cm^{-2} of 75As+ at 380 keV, 0.87×10^{13} cm^{-2} of BF2+ at 110 keV, 1.25×10^{13} cm^{-2} of 75As+ at 50 keV, 5×10^{15} cm^{-2} of P+ at 40 keV, and 3.5×10^{15} cm^{-2} of BF2+ at 35 keV. EBL-patterned PMMA (from MICROCHEM) layers are used in all implantation steps as the masking material. The SRIM software is used to estimate the required implantation energy for the chosen dopant species such that the resulting doping profile resembles the one shown in Figure 25(b). Rapid thermal annealing at 950 °C for 10 minutes is used to electrically activate the implanted dopants. The sample is then cladded under 1 μm of SiO_2 deposited by plasma-enhanced chemical vapor deposition (PECVD). Two via holes are patterned using an EBL step and dry-etched with Cr as a hard mask to reach the bottom Si layer (on the pedestal) as well as the top Si layer on top of the microdisk. In the last step, Ti/Cu metals are sputtered and lifted off on a $3-\mu m$ thick layer of patterned PMMA with the aid of sonication bath. In Figure 26(b), the SEM image of the device after metallization step is shown.

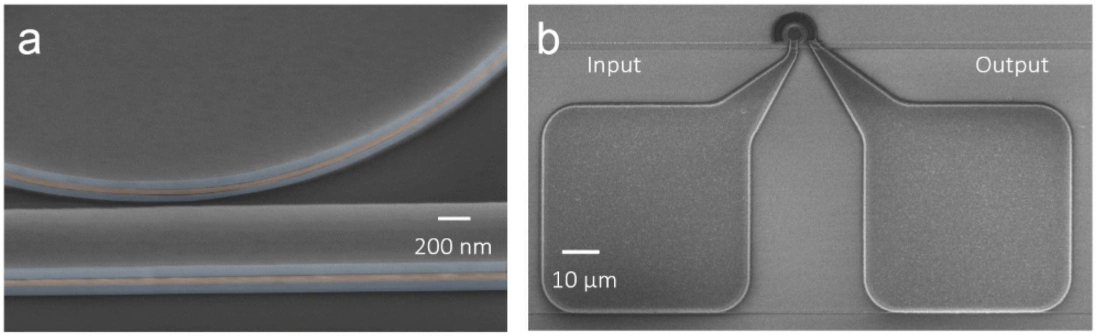

Figure 26: (a) Tilted SEM image of the gap region between the access waveguide and the microdisk resonator. False colors are used to accentuate the stacked Si (blue) and SiO_2 (pink) layers (b) Top view SEM image of the cladded device after metallization step showing the input/output waveguide, microdisk, and RF electronic pads. Pads are placed close to the microdisk (< 50 μm) to ensure electrically short connections to the device for $f \leqslant 50$ GHz.

5.4 High-speed Measurement Results

For both the dc and ac (or RF) characterization steps, the chip is mounted on a thermally controlled stage and fixed using a conductive double-sided adhesive tape. Two flat-cleaved single mode fibers (SMF) are used to couple light in and out of the chip with the aid of focusing grating couplers. The insertion losses of the two grating couplers and the propagation loss of the access waveguide are collectively measured to be 20 dB at 1560 nm. Since the goal of this work is the demonstration of the modulation technique in the multi-layer structure, a detailed optimization of the input/output coupler has not been performed. SMF fibers are mounted on a stage equipped with manual XYZ translation as well as tilt and rotation adjustments.

A tunable laser source (Agilent 8164A) is used to launch continuous-wave (CW) light into the input SMF fiber. In order to adjust the state of polarization of the incident light on the input grating coupler, a 3-paddle polarization rotator is placed on the input fiber. The output light is then coupled to the access waveguide on chip through the input grating coupler. After coupling to the microdisk resonator the light in the access waveguide is coupled out of the chip and into the output SMF by the output grating coupler. In the dc characterization case, the output fiber is directly connected to a photoreceiver (PDB150C from Thorlabs) with 10^4 (V/A) transimpedance gain. In this experiment, the laser wavelength is slowly swept (i.e., 5 nm/s) from 1550 nm to 1570 nm, and the corresponding detected voltage recorded using a data acquisition card (DAQ from National Instrument) and PC.

Figure 27(a) shows the measured normalized transmission spectrum for different applied dc voltages. The polarity of the dc voltage is chosen such that electrons and holes are accumulated on the n-type and p-type doped Si layers, respectively (referred to as positive polarity hereafter). As seen in Figure 27(a) the linewidth of the resonance feature in the transmission spectrum is ≈ 0.45 nm (i.e., loaded $Q \approx 3500$) for no applied dc voltage ($V_{dc} = 0$). The resonance wavelength and its associated extinction change V_{dc} increases from 0 V to 20 V.

The observed blue shift in the resonance wavelength and the change in the transmission extinction are attributed to the free-carrier plasma dispersion property of Si [46]. The accumulated free carriers slightly reduce the refractive index of Si, which in turn decreases the resonance wavelength. Moreover, the introduced free-carrier absorption (FCA) associated with the accumulated charges ($\Delta\alpha = 8.5 \times 10^{-18} \times \Delta N + 6 \times 10^{-18} \times \Delta P$) [46]) gives rise to an increase in the total internal loss of the microdisk resonator. Thus, the observed increase in the resonance linewidth (or decrease in the Q) in the transmission plots for $V_{dc} > 0$ is a direct consequence of FCA. Note that the waveguide-microdisk coupling-Q (Q_c) is designed such that the resonance mode under study is initially under-coupled at $V_{dc} = 0$. As the applied voltage increases, the intrinsic Q (Q_i) gradually matches Q_c, and the waveguide-resonator structure is pushed toward the critical coupling regime. This effect is clearly reflected in higher on-resonance extinctions in the corresponding transmission spectrum at higher V_{dc} as shown in Figure 27(a).

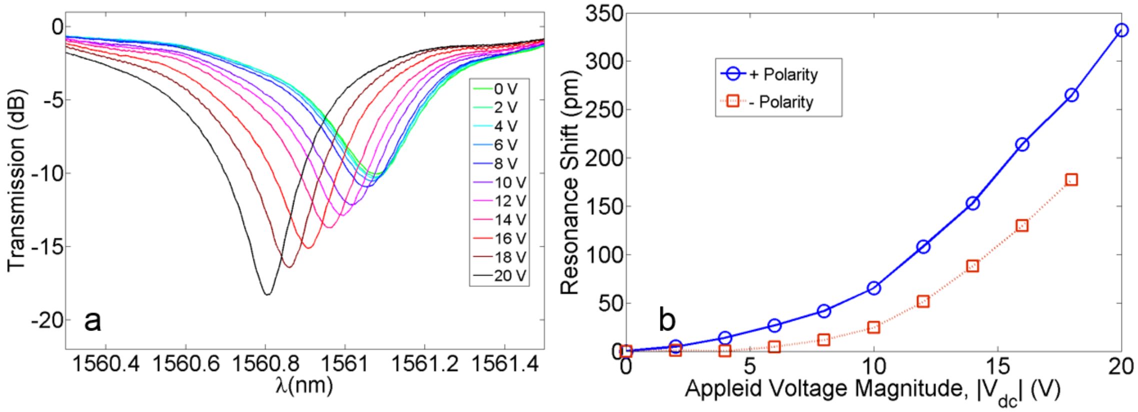

Figure 27: (a) Transmission spectrum of the device in Figure 26 for different applied dc voltages with positive polarity. (b) Measured shift in the resonance wavelength with respect to the applied dc voltage for positive (solid-blue curve) and negative (dashed-red curve) polarities.

The blue and red plots in Figure 27(b) show the measured shift in resonance wavelength as a function of V_{dc} with positive and negative polarities, respectively. Although the shifts for negative polarity V_{dc} follows the same trend as that with the positive polarity, the measured absolute resonance shifts are smaller in the former case. The lag in charge accumulation in this case can be readily explained by noting that the Si layers should first be depleted from the oppositely charged carries due to their initial doping (see Figure 25(b)), which requires higher levels of applied voltage in the negative polarity case. This situation is comparable to the inversion condition in a MOS capacitor [67]. In addition, it is seen that for V_{dc} more than $\approx 12\ V$, the resonance wavelength changes linearly at $\approx 25\ pm/V$, which is in accordance with the numerical predictions. For V_{dc} less than $\approx 12\ V$ the observed resonance shifts are smaller than what is predicated by a linear capacitor model. This disparity is attributed to a non-zero flat band voltage (possibly due to the introduction of charged ions, and etc. during the fabrication process).

Figure 28 depicts the setup used for the high-speed ac characterization. The optical power collected from the device is boosted using an erbium-doped fiber amplifier (EDFA) (VG2020 from ADVA with a total fixed gain of 21 dB) to compensate for the losses, primarily coupling losses. A high speed photoreceiver (PT-40G from Picometrix) with a cutoff frequency of 36 GHz is used at the receiving end of the output fiber. The optical amplification together with a variable optical attenuator (Agilent 8156A) ensures that the signal to noise (primarily receiver thermal noise) ratio is maximized while maintaining a linear response of photoreceiver. A programmable bandpass filter (Nistica Wavelength Selective Switch) with a 50 GHz passband is placed after the EDFA to suppress out-of-band amplified spontaneous emission (ASE) and associated noise (i.e., signal-ASE and ASE-ASE beat noise). To detect and correct for any drift in the fiber/grating alignments during the experiment, the output optical power was constantly monitored via a 10/90 directional coupler. The aggregate physical length of the output fiber from the EO modulator to the photoreceiver (apart from the EDFA) is approximately $10m$. The output voltage of the photoreceiver is monitored both in the time domain and the frequency domain using a wideband oscilloscope (Agilent DCA-X 86100D) and an electrical spectrum analyzer (Agilent 8564EC).

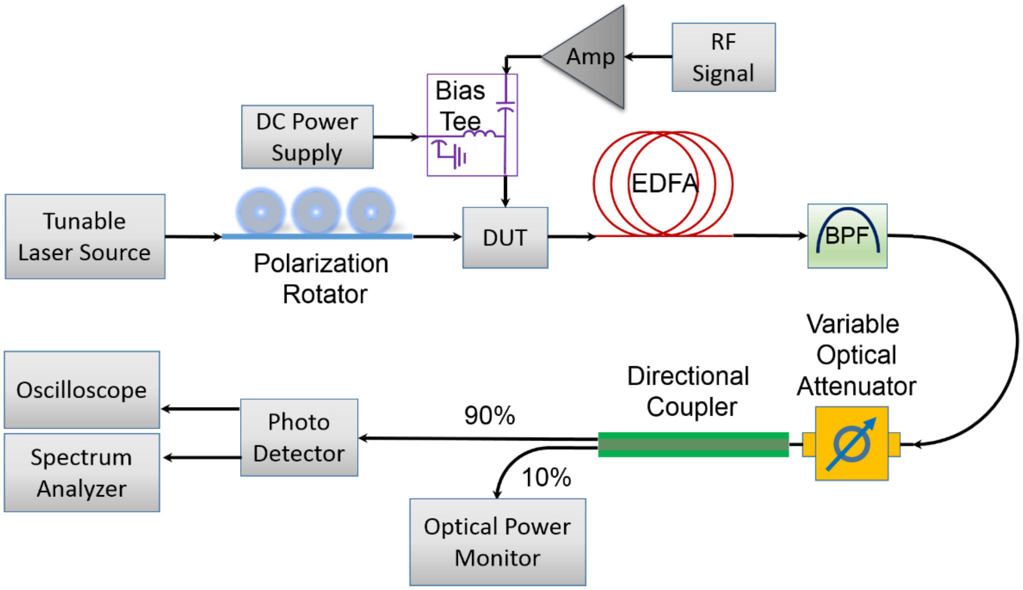

Figure 28: Schematic of the experimental setup for the high-speed ac measurement. DUT: device under test, BPF: band-pass filter.

In order to find the upper 3-dB cutoff frequency of the EO response of the modulator, I measure the frequency response of the device to a sinusoidal excitation with its frequency manually swept in 500 MHz steps in the range of 0.5 GHz to 15 GHz. The voltage excitation is generated by an RF signal generator (HP 83650B). An electrical amplifier (SHF 806E, bandwidth 38 GHz) with a nominal power gain of 26 dB is used to boost the electrical RF power. To deliver the electrical signal to the pads in Figure 26(b), a high-bandwidth probe (Cascade Microtech, Inc.) is used at the output of a bias tee, which combines the RF signal with a dc voltage signal. High-speed SMA cables and connectors are used to connect the lumped electrical elements. A $14V$ dc voltage is applied to bias the device in the linear regime (see Figure 27(b)). The output RF power of the signal generator is calibrated such that the delivered

RF power at the probe remains constant, i.e., 16 dBm, as the frequency is manually swept.

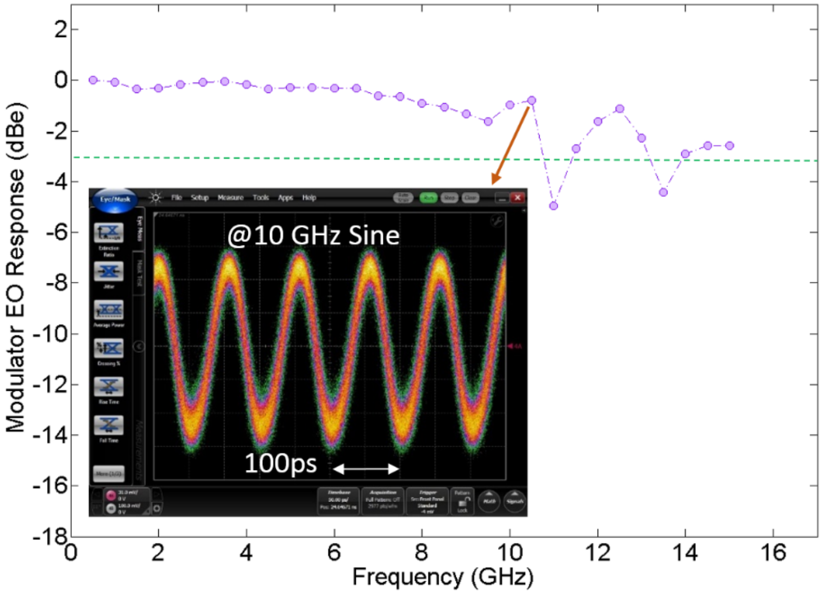

Figure 29: The measured frequency response of the accumulation mode modulator demonstrating a 3-dB bandwidth greater than 10 GHz. The inset shows the detected signal with a sinusoidal drive at 10 GHz.

Figure 29 shows the measured EO frequency response of the device in the range of 0.5 GHz to 15 GHz. The 3-dB upper cutoff frequency of more than 10 GHz is clearly observed in this experiment. The eye-diagram of the detected signal at 10 GHz is also provided in the inset of Figure 29. The observed EO response rolls off slowly and generally follows the estimations of Section 5.2 with a 3-dB frequency of more than 15 GHz. However, I also observe variations in the higher EO frequency response as shown by two unexpected decreases in the response above 10 GHz. The origin of these drops is not clear but likely stem from impedance mismatches between the probe and device. I also studied the response of the device to a pseudo-random bit sequence (PRBS) at 10 Gb/s and 15 Gb/s. The PRBS signal is generated via an SHF pattern generator and the SHF amplifier producing a peak to peak voltage ≈ 4 V. The corresponding measured eye-diagrams are shown in Figures 30(a) and 30(b).

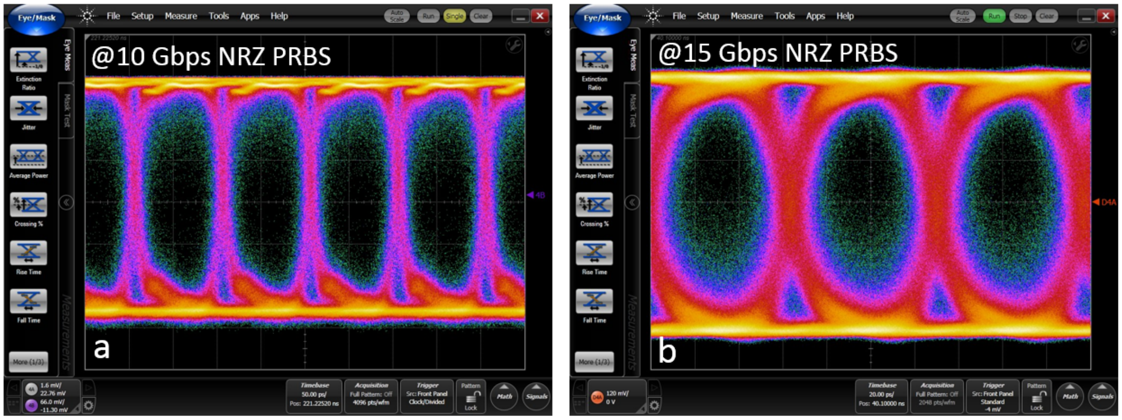

Figure 30: Measured eye-diagram of the modulator at (a) 10 Gb/s, and (b) 15 Gb/s with a $2^{15}-1$ long NRZ pseudorandom binary sequence (PRBS).

The modulation depth (MD) of $\approx$ 10 dB and insertion loss (IR) of $\approx$ 5 dB are estimated from the prior dc characterization experiment (laser wavelength is set around 1560.8 nm). Note that by tuning the laser wavelength around the resonance wavelength, less IR can be achieved at the expense of lower MD. The wide open eyes and sharp rise times seen in Figure 30 clearly indicates that data rates of more than 15 Gb/s are achievable. The source of the jitter noise observed on the rise time and fall time transitions (see the eye-diagram in Figure 30) again believed to be attributed to impedance mismatch. The rise and fall times evident in Figure 30 are consistent with device that is capable of handling data rates of up to 30Gb/s. While the performance of the modulator structure presented here is on a par with the best integrated photonic EO modulators, its clear advantages are the self-trimming, and compactness. As explained in the device architecture section, the performance of the device can be significantly enhanced by optimizing the doping profiles on the device as well as increasing the optical Q of the resonator by rearranging the electrical electrodes such that the need for the Si pedestal region around the microdisk is eliminated. None of these optimizations were performed in the results reported here.

My calculations show that the speed of the device can be enhanced by a factor of more than 2 by eliminating the parasitic capacitance (C_p) of the device. This can be achieved simply by containing the n-doping profile on the lower Si layer only around the optical mode (see Figure 25(b)). Elimination of the parasitic capacitance will also result in a reduction in power consumption by a factor of more than 2. In addition, optimization can be done on the position of electrodes to reduce the ohmic resistance (R) of the device. Thus, I have demonstrated a compact device architecture that is capable of modulation speeds in excess of 60 Gb/s with proper optimization.

In summary, a small-footprint ($\approx 30\ \mu m^2$) high-speed ($> 15\ Gb/s$) electro-optic modulator is demonstrated in this chapter. The modulation mechanism is based on carrier dispersion in Si through the accumulation mechanism in a Si/SiO_2/Si material platform. The estimated power consumption of the device is 55 fJ/bit. The operation wavelength of the device can be trimmed by up to 1 nm by a dc voltage without increasing the overall power consumption. Speeds more than 60 Gb/s and power consumptions less than 27 fJ/bit can be expected in future only by optimizing the doping profile of the device and improved instrumentation. Moreover, enhancement of Q of the microdisk through material platform/geometry optimization can improve the IR and MD figures of merit. The unique flexibility in controlling the device capacitance allows for device designs benefiting from a very low-voltage or a very high-bandwidth operation. The device performance is quite promising for future generation of short-reach optical interconnects and networks.

5.5 Spectrally Efficient Modulation Formats

The simple device introduced in this chapter provides us with a building block capable of performing high-speed modulation with on/off keying or binary phase shift keying formats. This device can be used in more complex optical architectures to achieve other optical modulation formats. As an example, it is possible to to implement quadrature phase shift keying (QPSK) modulation format by combining two of such building blocks.

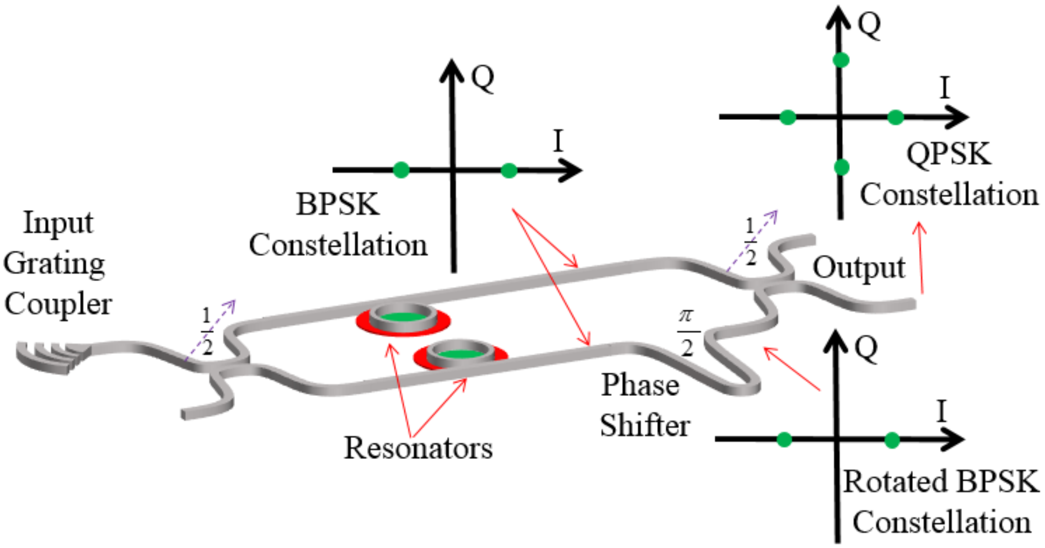

Figure 31: Schematic diagram of an optical QPSK modulator constructed with the aid of two identical resonance-based modulators featuring BPSK modulation format.

As seen in Figure 31, in the input of the system the power of the input laser is divided using a directional coupler between the upper and the lower waveguides. The data are imparted on the laser carriers with BPSK format through the micro-resonators. The constellation diagram of the two BPSK signals are shown in Figure 31. On the lower waveguide the phase shifter imposes a 90-degree phase on the optical signal which effectively rotates the corresponding constellation diagram. At the output another 3-dB directional coupler combines the two BPSK signals into one with QPSK modulation format. This architecture can be extended through nested Mach-Zehnder interferometers to generate 16-PSK or higher-order PSK modulation formats.

CHAPTER VI

ELECTRO-OPTIC MODULATION BASED ON NOVEL 2D MATERIALS

6.1 Overview

The emergence of two-dimensional materials combined with reliable growth and processing techniques, offer a promising solution to the looming problems facing CMOS technology as device dimensions continue to scale down to the size of a few atoms. Graphene, in particular, owing to its electronic dispersion properties, exhibits near-ballistic transport and high mobility ($\approx 200 \times 10^3\ cm^2V^{-1}s^{-1}$ for suspended samples and $\approx 40 \times 10^3\ cm^2V^{-1}s^{-1}$ for samples sitting on SiO_2 substrates) at room temperature [68, 69, 70]. This property allows for realization of high-speed switches, and transistors. Moreover, graphene is capable of remarkable interaction with optical waves (e.g., $\approx 2.3\%$ absorption of normal incident light for unbiased samples [71, 72]). Therefore, if integrated with Si, graphene can considerably enhance the functionalities of conventional CMOS devices by adding new capabilities such as photo-detection and optical modulation. Graphene in combination with other 2D materials has great potential for numerous applications including but not limited to wearable electronics, water desalination, bioelectric sensory devices, photovoltaics, and energy storage.

Recently, a monolayer of graphene sheet has been integrated with photonic crystal (PhC) microcavities in which the optical properties of the sheet were modulated by electrochemical approaches, i.e., gating through electrolytes such as ion gels [73, 74]. However, demand for high-speed devices prevents the use of such materials at their current stage since their response time is far slower than that of the state-of-the-art modulators. Therefore, an alternative to the electrochemical gating scheme that features fast tunability (e.g., thorough a dielectric layer) seems to be more relevant for high-frequency applications. In addition, integrated photonic devices with smaller footprints (e.g., microring and microdisk resonators) are generally preferred over PhC-based devices when dense-integration is considered.

The goal of this chapter is to demonstrate electrical gating of a monolayer graphene sheet through a thin dielectric layer embraced by the graphene sheet (as the top electrode) and a Si device layer (for the bottom electrode). In my design, a Si-based ultra-compact microdisk serves as the optical cavity where light-matter interaction takes place between the carriers in the graphene sheet (on top of the microdisk) and the optical field of the microdisk cavity. It will be shown that this interaction significantly perturbs the resonance characteristics of the microcavity as the optical conductivity of graphene is tuned by changing the gate voltage. Thus, this platform can be used for designing ultra-fast and ultra-compact integrated photonic modulators that can be highly useful for various applications including optical signal processing, optical communications, and optical interconnection.

6.2 Device Schematics

The cross-section of the envisioned device is shown in Figure 32. A microdisk resonator of small footprint (radius = 3 μm) fabricated in an SOI platform is at the heart of the device. The finesse of the resonator is designed such that the optical field intensity in the resonator is much higher than that in the feeding access waveguide. To provide electrical connection, the microdisk resonator is placed on top of a 50 nm-thick pedestal layer which is connected to an electrode on the other side of the waveguide. To form the gate dielectric layer, the chip is covered by a thin layer of insulating material. A monolayer of graphene sheet is overlaid on top of the microdisk resonator and is connected to the second electrode.

In the configuration shown in Figure 32, the application of a voltage between the two electrodes results in the accumulation of electrons/holes on the graphene sheet. This way, the Fermi level in the graphene sheet can be tuned quite easily by varying the applied external voltage in a rather wide range ($\approx \pm 1eV$).[1]

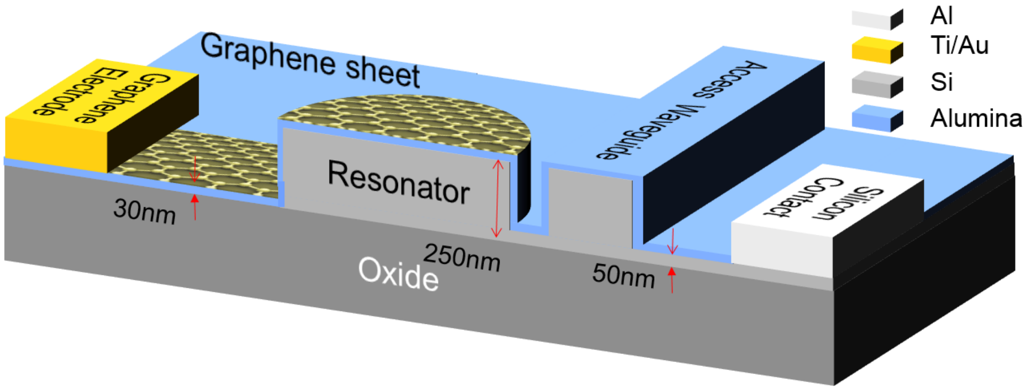

Figure 32: A 3D schematic representation of the graphene-based modulator. The graphene sheet is patterned such that it covers only the microdisk resonator and extends underneath the gold electrode. Alumina is used as the dielectric material in this design.

The electrical conductivity of the graphene sheet at optical frequencies (referred to as the optical conductivity) is crucially affected by the inter- and intra-band electronic transition rates, which in turn can be modified via filling or depleting the available electronic states (i.e., by accumulation of carriers) on the graphene sheet (see Figure 33(a)). For a single-layer graphene sheet, the optical conductivity can be modeled by a complex-valued function given by Kubo formula [75]:

$$\sigma(\omega) = \sigma_0 \frac{\mathrm{i}E_F}{\omega + \mathrm{i}\tau^{-1}} + \sigma_0 \left[\theta(\hbar\omega - 2E_F) + \frac{\mathrm{i}}{\pi} \log \left| \frac{\hbar(\omega + \mathrm{i}\tau^{-1}) - 2E_F}{\hbar(\omega + \mathrm{i}\tau^{-1}) + 2E_F} \right| \right]. \tag{28}$$

In Equation 28, $\sigma_0 = e^2/\pi\hbar^2 \approx 60\ \mu S$ is the minimum conductivity set by two fundamental physical constants, i.e., the electron charge e, and the reduced Plancks constant $\hbar$. In addition, θ is the step function, ω is the frequency of light, E_F is the Fermi level, and τ is the scattering rate which models the effect of carrier scattering

---

[1] Compared to bulk, i.e., 3D, semiconductors, 2D materials have fewer electronic states and hence the Fermi level in such materials is more sensitive to extrinsic carriers.

phenomena due to various sources such as intrinsic ripples on graphene or flexural phonons [76, 77, 78], adsorbed molecules [79, 80], point defects [81], charge impurities and cluster formation [82, 83, 84], resonant scatterers [85, 86] and bilayer regions [87]. Arguably, coulomb centers, ripples and resonant impurities seem to play the major role in the carrier scattering on a graphene sheet.

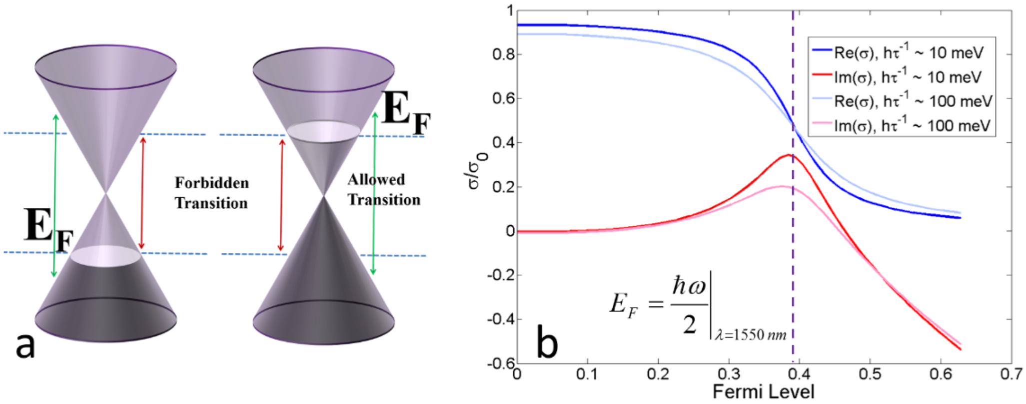

Figure 33: (a) The band structure of a monolayer graphene with the Fermi level below (left) or above (right) the Dirac point. Forbidden and allowed inter-band transitions are shown in red and green arrows, respectively. (b) The real and imaginary parts of the optical conductivity of graphene at $\lambda = 1550\ nm$ for two representative carrier scattering rates.

In Figure 33(b), the normalized (with respect to σ_0) optical conductivity of a graphane layer is shown (obtained for an optical excitation of $\lambda = 1550\ nm$). It is seen that both the real and the imaginary parts of the optical conductivity undergo a significant change as the Fermi level reaches half the photon energy, i.e., $E_F = \hbar\omega/2$. Since beyond this Fermi energy level inter-band transitions are prohibited (due to Pauli exclusion principle), a notable change in the optical conductivity is explicable. The carrier scattering phenomena induce a broadening effect which smooth out the sharp transition around the $E_F = \omega\hbar/2$ point as seen in Figure 33(b).

6.3 Device Fabrication and Characterization

The device is fabricated on a commercially available SOI wafer with a 3 μm BOX layer and a 250 nm Si device layer. The passive microdisk resonator and the access waveguide are defined on the device layer through a standard electron-beam lithography (EBL) step, in which a 110 nm-thick spin-coated HSQ layer is used as the mask and subsequently etched in an inductively coupled plasma (ICP) chamber. A 50 nm-thick Si pedestal is selectivity left unetched around the resonator device for electrical connection; and the sample is mildly doped (p-type) in a diffusion furnace afterwards. Then, through a conventional single-layer lift-off processes, 800 nm of aluminum is placed on the pedestal region, which provides electrical connection to the Si layer. Subsequently, using atomic layer deposition (ALD), a thin (i.e., 30 nm) layer of Al_2O_3 was deposited all over the sample to form the dielectric layer. In the next step, through a wet transfer process, a sheet of monolayer graphene is placed on top of the chip. The used graphene sheet is grown on a copper foil and is coated with PMMA (from ACS Material-Advanced Chemicals Supplier) [88]. Before the transfer step, the copper layer is removed through a wet-etch process and the top PMMA is dissolved in acetone after the graphene sheet is transferred on the chip. In the next step, the chip is annealed at 300 °C in vacuum to ensure good adhesion. The graphene layer is patterned through an EBL step with an 800 nm-thick spin-coated PMMA layer as the mask. Second electrical pad (10 nm titanium/50 nm gold) is then lifted off on the graphene region.

An optical micrograph of the fabricated device is shown in Figure 34(a). The yellow square (with rounded edges) on top of the resonator is the gold contact. The white square below the waveguide is the aluminum contact behind which the pedestal layer is extended (the square with sharp edges). The dark spots on top of the aluminum pad are the remnants of the graphene layer which are peeled and curled up.

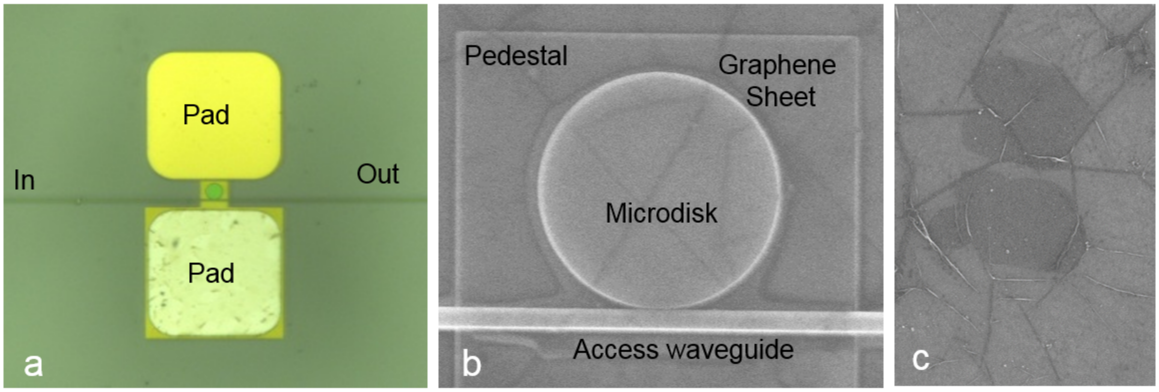

Figure 34: (a) An optical micrograph of the device illustrating the Au and Al pads on the graphene sheet and the Si pedestal. (b) An SEM image of the microdisk showing the transferred graphene layer on the device. (c) An SEM image from the transferred graphene sheet on a flat area.

Since the graphene layer is only one atom thick, it induces an imperceptible contrast against its surroundings on a Si substrate. To make sure that the graphene layer is in good condition, an SEM image is taken from the device. As seen in Figure 34(b), the graphene sheet is connected and exists on the resonator area which confirms the quality of the transfer.

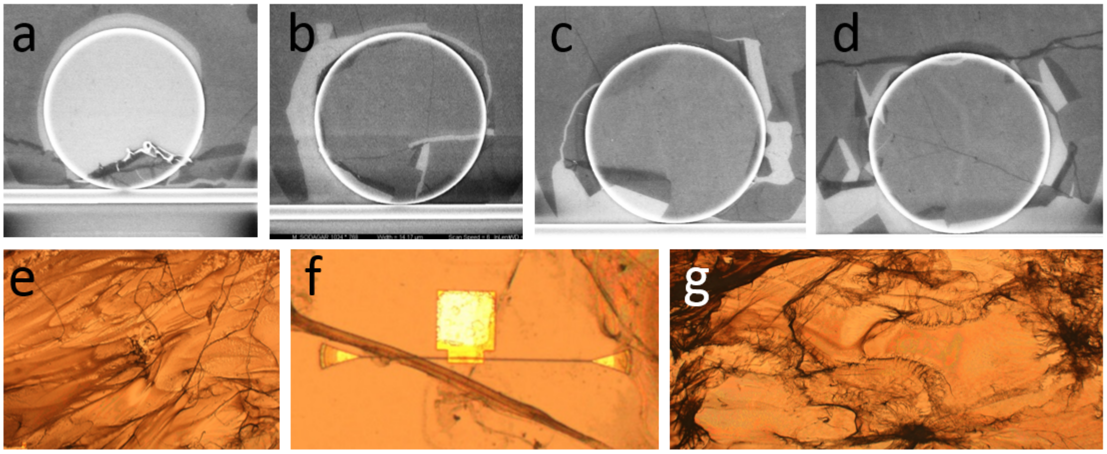

Figure 35: (a-d) SEM images of the graphene sheet transferred on microdisk resonators. It is seen that the graphene sheet is torn apart at the periphery of the microdisk where the surface of the chip is not flat. (e-g) Optical micrographs of the showing the curls and wrinkles on the graphene sheet after the transfer process.

Note that the transferred sheet is prone to wrinkle formation and large-scale tearing during wet transfer process. The grain boundaries of the graphene sheet as well as wrinkles on the sheet are visible in Figure 34(c). Moreover, transfer on non-flat surfaces applies strain on graphene sheet and tears the layer over the step regions. This issue significantly reduces the yield of this process. In Figures 35(a-d), the occurrence of such small-scale tears is shown. Optical micrographs of large-scale wrinkles are also shown in Figures 35(e-g). Although the contrast (on either optical or electron microscope images) of the transferred sheet can be a good indicator of the number of actual layers in the transferred sheet, a more accurate means to count the total number of layers is to use Raman spectroscopy.

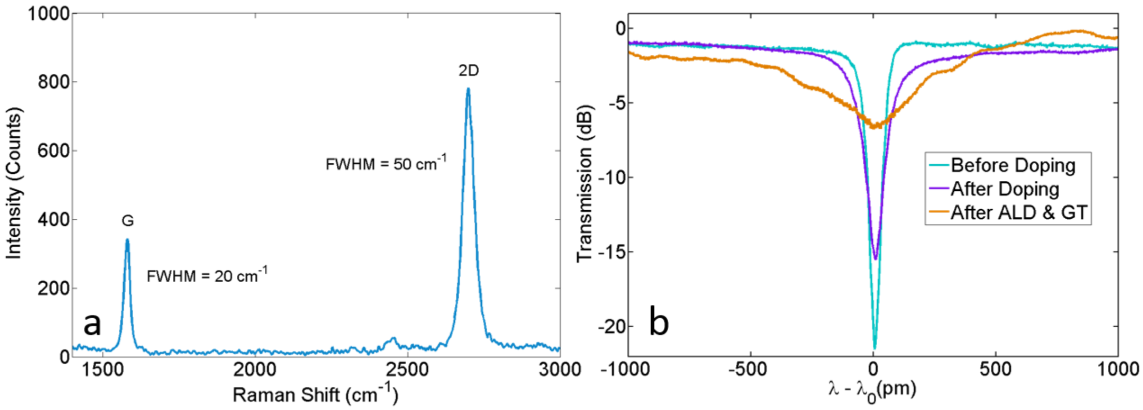

Figure 36: (a) The Raman spectrum of the graphene sheet transferred on the Si substrate. (b) Optical transmission spectra of the device collected after etching the passive device, after doping the sample, and after the ALD/graphene transfer (GT) step. Plots are superimposed such that the linewidth of the resonances can be compared.

In a typical Raman analysis, two main peaks are expected in the spectrum collected form a graphene sheet. The first peak is usually labeled as G (at $\approx 1580\ cm^{-1}$) which is due to the primary in-plane vibrational mode, and the second peak is usually labeled as 2D (at $\approx 2690\ cm^{-1}$) which is due to the second-order overtone of another in-plane vibrational mode, i.e., D at $\approx 1350\ cm^{-1}$. It can be shown that the ratio of the corresponding peak intensities, i.e., I_{2D}/I_G, as well as the exact position and linewidth of these peaks are related to the actual number of layers [89, 90, 91, 92]. The Raman characterization of the transferred graphene sheet in my device (see Figure 36(a)) suggests that the transferred sheet is mostly single-layer with a rather low defect density.

The device is optically characterized at different stages of the fabrication process, i.e., (a) after the etching steps, (b) after the doping step, and (c) after the graphene transfer step. Characterization of the device is done by launching laser light (from a tunable laser source) into a single-mode fiber (SMF) and delivering it to the access waveguide with the aid of a grating coupler. A polarization rotator is used to excite the TE mode in the access waveguide. At the output the transmitted light is collected in the output SMF and is fed to a photodetetor. To compare the effect of doping, and graphene layer on the Q of the microdisk resonator, the collected transmission spectra around the resonance wavelength of the microcavity are superimposed and shown in Figure 36(b). It is seen that the loaded-Q slightly decreases from $\approx 13K$ to $\approx 9K$ after doping, which is due to the free-carrier absorption effect in Si. The loaded-Q further reduces to $\approx 4K$ after deposition of the alumina layer and graphene transfer (see Figure 36(b)). This lower loaded-Q is attributed to the excessive loss due to the graphene sheet and also possible residues of PMMA left on the sheet.

Once the fabrication steps are completed, I study the effect of electrostatic gating (of the graphene sheet) on the transmission characteristics of the access waveguide. To gate the graphene sheet, a voltage signal (peak-to-peak amplitude of $V_{pp} = 10V$) is applied between the two pads (i.e., the gate and the substrate electrodes). The applied voltage is changed in discrete steps such that it follows a triangular pulse train (see Figure 37(a)). The transmission spectrum of the device is monitored and recorded for each and every step. In Figure 37(b), a representative subset of such transmission spectra are shown. Also the resonance wavelength of the first two radial modes of the microdisk resonators are plotted versus time in Figure 37(a). As is clear from the plots, the resonance wavelength of the microdisk cavity drifts toward shorter wavelengths over time as the voltage signal varies.

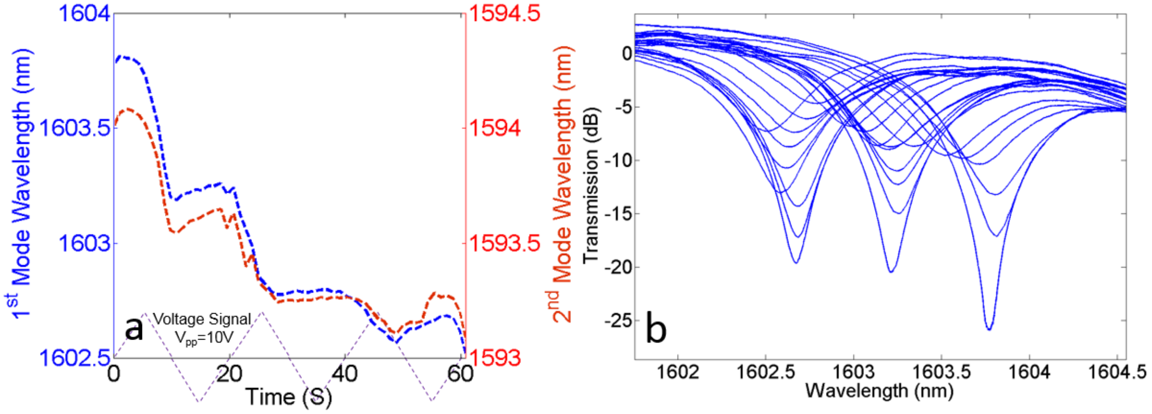

Figure 37: (a) Drift in the resonance wavelength of the first and the second radial modes of the microdisk resonator. The applied voltage is a triangular pulse train with a period of $T = 20\ s$. (b) A few representative transmission spectra recorded at different points in time.

This undesirable behavior cannot be explained only by considering the optical conductivity of the graphene layer. Since the experiment is done in an uncontrolled ambient conditions, the drift in resonance wavelength is proposed to be due to the adsorbates (such as H_2O molecules) coming from the ambient air [93]. To prevent substance adsorption by the graphene layer, a thin ($10\ nm$) layer of alumina is deposited on the sample through atomic layer deposition. This protective layer proved to be helpful in terms of eliminating the drift issue. After passivation step, the characterization process of the protected sample is repeated with the same pulse train but higher voltage swing (i.e., $V_{pp} = 30\ V$). In this experiment, the resonance wavelength of the microdisk cavity along with its extinction is monitored as the gate voltage swings at a low frequency (i.e., period of $T = 20\ s$) for five consecutive cycles.

In Figure 38, the average (i.e., over five cycles) resonance wavelength and extinction at resonance are plotted in blue and violet colors, respectively. As seen in both plots, there is no noticeable ambient-induced drift. Although the blue shift in the resonance wavelength is predicted by FEM simulation results, the observed hysteresis in both extinction and shift is not corroborated by the used simple model (i.e., the Kubo formula). This behavior is suspected to have its origin in trapped charges both at the graphene/alumina as well as the alumina/Si interfaces and possibly on the graphene defect sites [94].

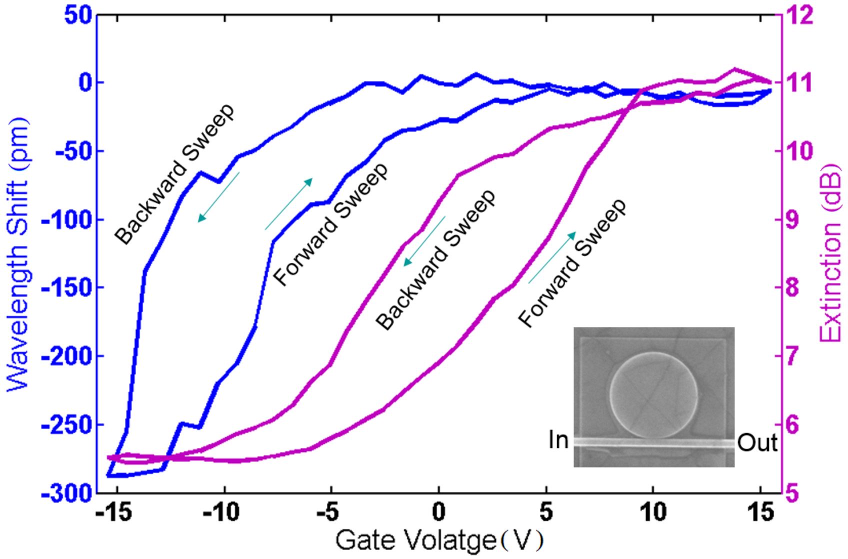

Figure 38: Transmission spectrum of device after passivation. The laser wavelength is matched with the resonance wavelength of the microdisk resonator.

In summary, a monolayer of graphene sheet is integrated on top of a small footprint microdisk cavity, which is fabricated in an SOI platform. The strong electro-optic interaction between graphene and whispering gallery modes of the microcavity is studied and demonstrated. Although the hysteresis issue still needs to be addressed, the overall results presented in this chapter are quite promising for high-speed EO modulation applications.

CHAPTER VII

COMPACT FIELD-PROGRAMMABLE PHOTONIC DEVICES

7.1 Overview

The realization of low-power optical devices for scalable optical interconnects has been of great interest lately. Among essential building blocks for interconnects, optical switches have received special attention due to their unique role in routing data in complex optical networks. Of particular interest is the development of optical switches that can be configured by the end user (similar to the field-programmable gate arrays (FPGAs) in digital electronics).

Silicon (Si) has been the most highly used material for the implementation of on-chip optical switches due to the low cost, the ease of fabrication, and the possibility of integration with electronics. In fact, photonics community has witnessed a rapid growth in research on active and passive integrated photonic devices in Si during the past decade. The reconfiguration (or tuning) of Si-based devices has been based mainly on free-carrier dispersion [95] and thermo-optic effect [96]. The former is the technology of choice for making high-speed switches due to its fast dynamics. Optical comb switch functionality mediated by either free-carrier generation through photon absorption or carrier injection/depletion has already been demonstrated on Si-on-insulator platform and successfully incorporated in optical networks for data routing featuring extensive data rates of up to 250 $Gbps$ [97]. In such designs, high-Q resonators serve as the building blocks of the system, offering short transition time (< 1 ns), low insertion loss, and sufficient extinction ratio (> 10 dB) [97, 98, 99, 100]. Despite unique features of resonance-based optical devices in Si, a simple approach for forming field-programmable optical devices (e.g., switches) in Si is still missing. In this work, I demonstrate the first field-programmable optical unit based on irreversible electrical breakdown of a layer of silicon oxide (SiO_2) embedded in a high-Q optical microresonator. In comparison to electronics, this unit nearly mimics the functionality of a simple one-time field-programmable electrical switch for routing optical signals.

7.2 Theory and Fabrication

The fundamental device that forms the building block for the field-programmable structure is composed of a microdisk resonator (radius $\approx 3\ \mu m$) coupled to an adjacent waveguide (width of 450 nm) formed by electron-beam lithography (EBL) and inductively-coupled plasma (ICP) etching. The material platform used in this work is a high-quality multilayer structure formed by vertically stacked layers of Si, SiO_2, and Si. This multilayer platform is prepared by direct bonding of two SOI wafers (from Soitec). First, a thin oxide layer (30 nm) is thermally grown on the two SOI wafers. This step leaves 110 nm Si on the device layer on each wafer. After bonding the two wafers and backside etching, the $Si/SiO_2/Si$ stack with 110 nm, 60 nm, and 110 nm thicknesses, respectively, is ready. In the next step, the optical devices (i.e., a microdisk with 3 μm radius in proximity of an access waveguide along with the grating couplers at the input/output terminals) are defined through EBL, and dry-etched with Cl_2 chemistry in an ICP chamber. A thin (50 nm) pedestal in the bottom Si layer is left unetched and later selectively etched away. Then, the device is cladded under 1.2 μm of SiO_2 through plasma-enhanced chemical vapor deposition (PECVD). Two via holes are opened on top of the disk and on the pedestal; both 1 μm away from the resonator periphery to access the top and bottom Si layers of the disk without interfering with the optical mode of the resonator. Afterward, contacts and pads are defined at these vias through a metallization/ liftoff process.

Figure 39(a) shows the scanning electron micrograph (SEM) of a ridge waveguide fabricated in this hybrid Si/SiO$_2$/Si material platform. Figure 39(b) and 39(c) depict the SEM of the overall coupled waveguide-cavity device and the micrograph of the metallic pads on the fabricated structure, respectively. The operation of the device in Figure 39(b) is based on coupling the input light (e.g. from an optical fiber) to the waveguide and monitor the output transmission after the resonator as shown in Figure 39(b). This transmission characteristic can be altered by applying an electronic signal (i.e., a voltage) between the two electrodes in Figure 39(e).

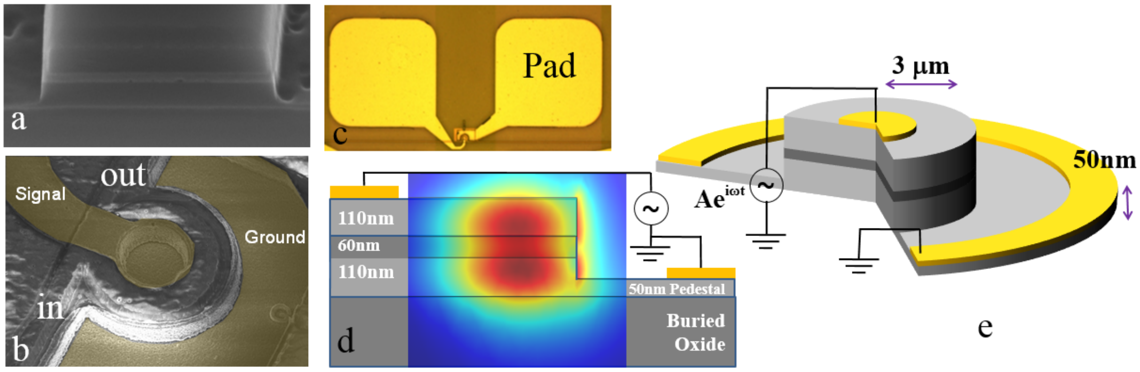

Figure 39: (a) Cross section of a fabricated waveguide in the multilayer bonded platform; (b) tilted SEM image and (c) optical micrograph of the fabricated device; (d-e) 3D schematic along with the cross section of the device superimposed with the TE-polarized optical mode obtained through finite element method (FEM) simulation at 1540 nm.

As discussed in Section 2.4, assuming the CMT, the transmission spectrum of an access waveguide coupled to a travelling wave optical resonator can readily be obtained as [101]:

$$T_{Through}(\lambda) = \frac{\sqrt{1-\kappa^2} - \alpha e^{-i\phi(\lambda)}}{1 - \sqrt{1-\kappa^2}\alpha e^{-i\phi(\lambda)}}, \tag{29}$$

where κ and α are the waveguide-resonator coupling coefficient and the resonator roundtrip transmission (considering both radiation and material losses), respectively. ϕ is the accumulated phase shift observed by the optical field (at wavelength λ) after one complete rotation around the resonator. In a typical high-Q resonator, the loss factor and the coupling coefficient are usually small (i.e., $\alpha \approx 1$, and $\kappa \approx 0$); and the waveguide transmission features a rather sharp Lorentzian lineshape at the resonance wavelength of the resonator with zero transmission in the critical coupling regime [101]. In a cavity with high optical loss (i.e., $\alpha << 1$), the optical field will not build up; and the resonance signatures fade away. Equation 29 suggests that at very high resonator loss (i.e., $\alpha \rightarrow 0$), the transmission amplitude approaches unity for all wavelengths (i.e., $T_{Through} = \sqrt{1-\kappa^2} \approx 1$). Therefore, by using a mechanism to permanently convert a low-loss cavity to a high-loss one, a one-time configurable on/off switch can be formed for operation in the resonance bandwidth of the cavity. I use dielectric breakdown in the SiO_2 layer [102, 103] sandwiched between the two Si layers for this purpose as shown in Figure 39(d).

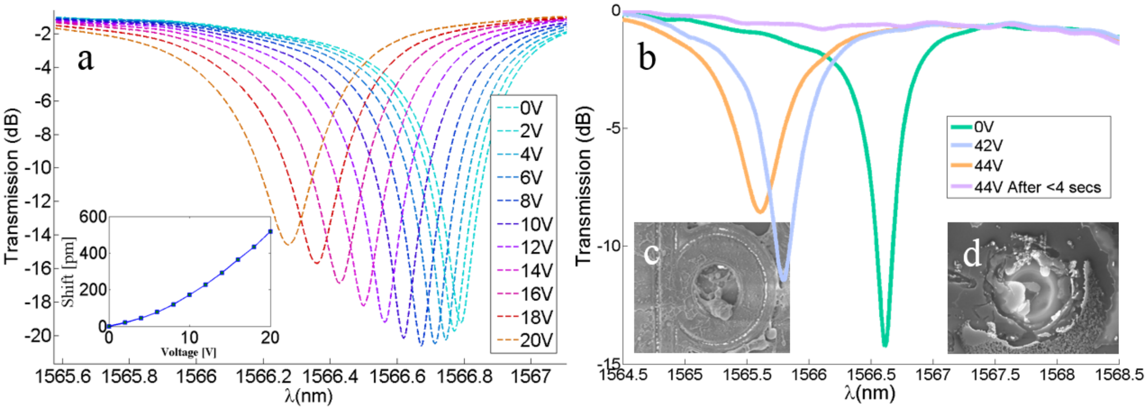

Figure 40: (a) Transmission spectrum of the device in Figure 39 under different voltages; (b) demonstration of resonance elimination through irreversible oxide breakdown; (c,d) SEM images of the structure after breakdown; (c) device metallization is melted after breakdown; (d) view after removing the metallization, the cladding layer, and the top Si layer showing the damaged bottom Si layer.

In this structure, the application of the voltage V between the two electrodes results in the accumulation of positive and negative charges on the two sides of the SiO_2 layer (in the two Si layers) similar to a conventional parallel plate capacitor. The electric field (E) inside SiO_2 layer is $E = V/d$, with d being the thickness of the SiO_2 layer (60 nm in this case). Considering the breakdown field of SiO_2 ($E_{bd} \approx 10$ MV/cm [104]), the application of a voltage around $V = 60$ V can result in the breakdown of the SiO_2 layer; resulting in a very high loss (and thus very low Q) in the resonator and negligible effect of the resonator on the transmission spectrum in the adjacent waveguide. The optical profile of the transverse electric (TE) mode (i.e., electric field in the plane of resonator) of the resonator shown in Figure 39(d) indicates a reasonable extent of the field in the SiO_2 layer.

To study the response of the device described in Figure 39, the transmission spectrum of the access waveguide is monitored for different applied voltages by launching the output light of a tunable laser (Agilent 81682A) into the access waveguide and collecting light out of it through a pair of grating couplers. The plotted data in Figure 40(a) clearly show the modulation of the resonance wavelength of the resonator by the application of the voltage. The reason for this modulation is the accumulation of positive and negative charges on the two Si layers that results in a change in the index of refraction through the charge-induced plasma dispersion effect [103]. Also it can be seen from Figure 40(a) that the resonance linewidth progressively widens from 400 pm to 500 pm as the applied voltage increases. This is due to the added free-carrier loss caused by the accumulated charge in Si [46].

The effect of the applied voltage in excess of $40V$ is shown in Figure 40(b) indicating that wavelength shifts up to ≈ 1 nm (from ≈ 1566.6 nm down to ≈ 1565.7 nm) is possible by accumulating enough charges on the Si layers. The required voltage for this shift can be drastically reduced by using a much thinner (compared to 60 nm) high-k dielectric material instead of SiO_2 between the two Si layers provided that the dielectric layer can withstand the mechanical stress. Moreover, as expected, the dielectric layer starts to leak after being exposed to a high-magnitude electric field, and eventually undergoes a permanent physical damage exhibiting excessive optical loss, which in turn renders the cavity optically inactive. The purple plot in Figure 40(b) shows that the resonance features disappear when $V = 44$ V is applied. Comparing the transmission spectrum of this damaged device with that of the original one clearly shows the field-configuration possibility of this device.

An SEM image from the top surface of the device is shown in Figure 40(c). It is seen that the metallic layer is completely melted and spilled all over the cladding on the resonator and waveguide. This could be explained by considering the relatively high thermal power dissipation on the electrodes via Joule-heating process during breakdown. During this high current transition, the Si and SiO_2 layers also undergo an irreversible destructive physical damage, which is considered the primary source of optical loss. Figure 40(d) shows the top view of the device where a hole through the Si layer is visible. This image is taken after dissolving the metal remnants (see Figure 40(c)) in a wet copper etchant and pirahna solution and removing the cladding (oxide) in buffered oxide etch (BOE). The top Si layer was also etched away in the ICP chamber. Figure 40(d) clearly shows the permanent damage of the SiO_2 and the bottom Si layers, which is responsible for the effective removal of the spectral features of the corresponding resonator from the device characteristics. Similar devices can be fabricated in other conventional substrates (such as SOI) featuring a vertical thin slot. On such a platform, the electrically-induced breakdown scheme presented here can also be adopted for other integrated photonic structures (e.g., slot waveguides). In such settings atomic layer deposition can be used to infiltrate the slot with an appropriate dielectric material.

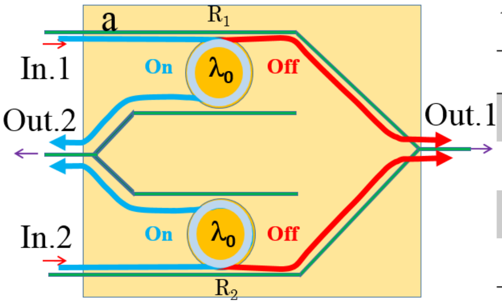

b Operation Table

Input	R_1/R_2	Output
In.1	Off/X	Out.1
In.2	X/Off	Out.1
In.1	On/X	Out.2
In.2	X/On	Out.2

Figure 41: (a) Schematic of the 2×2 switch describing the on/off behavior of the device with the resonators in and out of operation; (b) operation table for the resonator states (the X sign indicates that the resonator can be either on or off).

The simple programmable unit in Figure 39 can be used as the building block in more complex field-programmable systems. As an example, Figure 41(a) shows the schematic of a 2×2 programmable switch composed of two programmable optical resonators with matched resonance wavelengths, each coupled to an additional drop waveguide. The governing equation for the transmission spectrum of the access waveguide in such add/drop configuration is similar to Equation 29. However, the energy loss due to the additional (drop) waveguide contributes to the total resonator loss as well. As seen in Section 2.4, the spectral response of the drop waveguide can be readily expressed as [101]:

$$T_{Drop}(\lambda) = \frac{\sqrt{\alpha}\kappa_1^* \kappa_2 e^{-i\phi(\lambda)/2}}{1 - \sqrt{(1-\kappa_1^2)(1-\kappa_2^2)}\alpha e^{-i\phi(\lambda)}}, \tag{30}$$

where κ_1 and κ_2 are the coupling coefficients of the resonator to the access and drop waveguides, respectively. Also, α and ϕ have the same definition as those in Equation 29. It can be seen that as the resonator loss becomes very high (or equivalently, as $\alpha \to 0$), the drop port transmission is effectively suppressed at all wavelengths. Thus, the state (burnt/not burnt) of each resonator can be configured so that either of the two input ports can be independently routed to any of the two output ports as shown by the operation table in Figure 41(b).

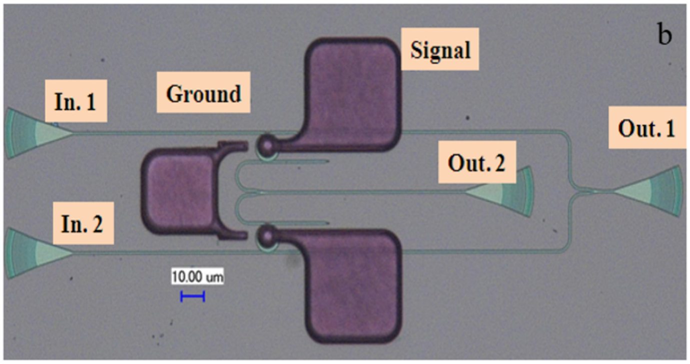

Figure 42: Optical image of the actual fabricated device.

The optical micrograph and SEM of the device is shown in Figure 42 and in the inset of Figure 43, which is fabricated on a similar platform following the same steps mentioned earlier. However, for this device the 50 *nm*-thick pedestal was not etched away, so the blanket pedestal extends over the whole chip. Also, a common ground electrode has been envisioned for both resonators to keep the device footprint small. In this design, resonators (6 μm in radius) are placed 180 *nm* and 200 *nm* away from the 450 *nm* wide add and drop waveguides, respectively. Focusing grating couplers with peak transmission wavelength around 1570 *nm* were also incorporated at the terminal of all input/output waveguides. The spacing between input/output couplers was chosen according to my measurement setup constraints and no attempt has been made to minimize the overall footprint of the device (currently around 0.2 mm^2).

7.3 Characterization

Figure 43 shows the normalized transmission spectrum of the device in Figure 41 at different stages of characterization. The data are normalized to the response of the input/output grating coupler on the device such that the coupling loss of the grating couplers, the propagation loss of the waveguides, and the scattering loss of the Y-junction are eliminated. Although, the two resonators were designed to have similar resonance wavelengths, post-fabrication characterization revealed that their resonance wavelengths differ by ≈ 1 *nm* due to fabrication imperfections (see Figure 43).

To correct this fabrication-induced deviation, I used a scanning electron-beam microscope (Zeiss Ultra60 FE-SEM) and exposed the cladding of the red-shifted resonator to 118 *pA* electron-beam current (with extra high tension (EHT) voltage set at 20 *kV*) in four separate stages for 210 seconds in total. As can be seen in Figure 43, the resonance wavelength originally located at 1567.5 *nm* (dashed pale blue curve) was progressively reduced and successfully positioned within 10 *pm* of the other one at 1566.4 *nm* (solid blue and pink curves). After this post-fabrication trimming process, the drop port of the device (Out.2) was characterized. Figure 43 shows the collected spectrum at the Out.2 port with input fibers positioned at the In.1 and In.2 ports (dark violet and dark green curves, respectively). Similarly, the pale violate and pale green curves refer to same measurements after their respective resonator is burnt. As can be seen in Figure 43, both routes exhibit an on/off extinction ratio of more than 20 *dB*.

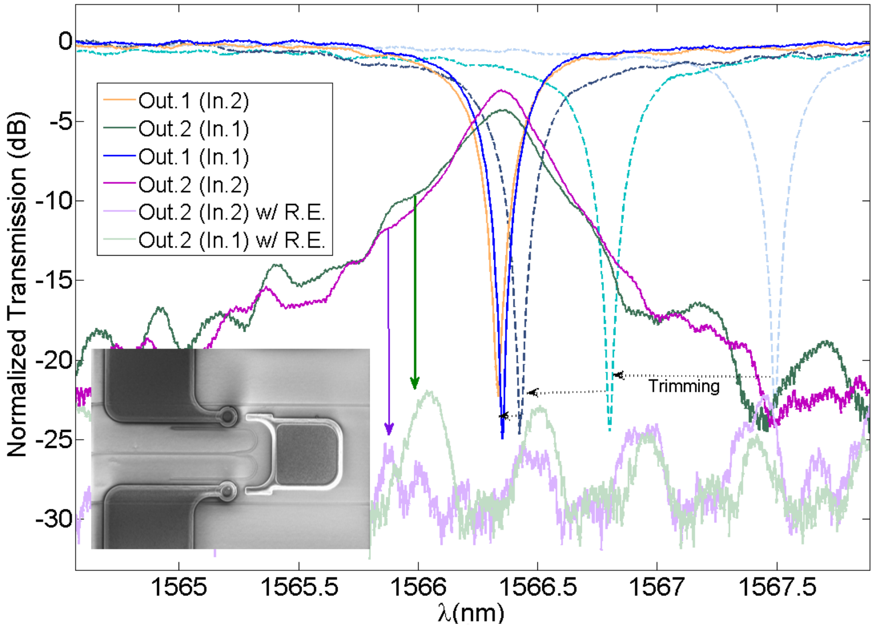

Figure 43: Normalized spectrum of the through port (Out.1) of the 2 × 2 switch in Figure 41 during resonance trimming (dashed curves colored with shades of blue); the solid blue curve is the trimmed top cavity resonance, which sits 10 *pm* away from the bottom cavity resonance (pink curve). Solid green and violet curves are the transmission spectra collected at the Out.2 port with the laser light launched in In.1 and In.2, respectively. The corresponding spectrum after resonance elimination are drawn in pale green and pale violet. The operation is in accordance with the operation table in Figure 41(b). The inset shows an SEM image of the fabricated device.

Characteristics shown in Figure 43 are in good agreement with the operation table in Figure 41(b), and they clearly demonstrate the device functionality as a field-programmable 2 × 2 switch. A similar approach, in conjunction with post-fabrication trimming, can readily be adapted for demonstration of more intricate optical architectures with system-level functionalities including field-programmable

$N \times N$ optical switching, optical FGPA, passive spectrometers, field-programmable optical filters, etc.

CHAPTER VIII

OPTICAL BISTABILITY IN INTEGRATED OPTICAL CAVITIES

8.1 Viewpoint

Use of nonlinear properties of optical materials is inevitable for all-optical signal processing applications [105]. In general, nonlinear optical coefficients such as the third order nonlinear susceptibility (χ^3), in common integrated photonic materials, i.e., silicon (Si) and silicon nitride (Si_3N_4), are relatively weak and can be neglected in low field intensity limits [106, 107]. Nevertheless, in high-Q microresonators with small effective mode volumes, the field intensity (and optical power density) can reach a rather high level such that nonlinear effects become significant even at modest input powers. Optical bistability in passive optical resonators, as one manifestation of nonlinear effects, has long been of interest as a simple mechanism to manipulate light with light. This phenomenon has been observed and carefully studied in various material platforms and different types of integrated resonators including one/two-dimensional PhC resonators, microdisk, and microring resonators [108, 109, 110, 111, 112, 113, 114, 115]. It has been shown that the interplay between the heat generation due to optical absorption at resonance wavelength and the shift in the resonance wavelength of the resonator caused by the thermo-optic effect of the resonator material can result in a hysteretic behavior and a positive feedback process which can lead to optical bistability. Thermal bistability is especially important in Si photonics due to the widespread use of Si on the device layer for integrated photonic structures. In most of the reported Si photonic devices to-date, thermal bistability relies on the nonlinear optical absorption processes, i.e., two-photon absorption (TPA) and the subsequent free-carrier absorption (FCA). Thermal-bistability can also be achieved through linear absorption in optical resonators [116]. However, in both cases of thermal-bistability, the threshold field density in the resonator is very high. This severely limits the use of optical bistability to form practical nonlinear integrated photonic devices in Si. In this work, I propose and demonstrate low-power thermal-bistability in Si photonic resonators with moderate Qs (e.g., $10k$) based on amplification of the heat generated by linear absorption using Joule-heating [117]. In the designed device, a reverse-biased pn-junction is integrated with a nanobeam PhC resonator. The illumination of the depletion region of the pn-junction by the incident light results in photo-generated carriers through linear absorption in Si. These carriers are swept by the electric field (due to the reverse bias) and are collected at the two sides of the pn-junction device [118, 119, 120, 121]. Such photocurrent, though small, once accompanied by a large reverse bias can considerably increase the heat generated per absorbed photon via Joule-heating to substantially reduce the optical power threshold for achieving optical bistability. My experimental studies show that the photocarriers are induced mainly by the linear optical absorption in the device. The proposed approach can be exploited to design ultralow power optical transistors, optical memory elements, and ultrasensitive sensors [122, 123, 124, 125]. In addition to its contribution to heat generation, the photocurrent can be monitored in an external electronic circuit to generate a negative feedback signal (i.e., adjusting the reverse bias voltage) to stabilize the bistable features against the random variations of the environmental conditions (e.g., temperature).

8.2 Photonic Crystal Nanobeam Cavity Design

The PhC nanobeam resonator used in this study is designed and fabricated in a silicon-on-insulator (SOI) substrate with a 250 nm-thick Si layer on a 3 μm buried oxide layer. The resonator comprises a symmetric resonant region sandwiched between two symmetric PhC mirrors. The resonant region and the PhC mirrors consist of a number of air holes with their centers located in a one-dimensional (1D) periodic lattice with lattice constant a (see Figure 44(a)). These air holes are etched in a Si rib waveguide with a width of w sitting on a 50 nm-thick pedestal. The radii of the air holes in the mirror regions are equal to r_m, while the radii of the air holes in the resonant region are different from each other and they are optimally engineered to maximize the quality factor. The overall structure is symmetric around its center. The resonant region has 15 pairs of air holes while each mirror section contains five air holes. The number of air holes for the two mirrors is chosen to ensure a decent coupling Q (Q_w) between the resonator and the inline waveguide at the two terminals of the device.

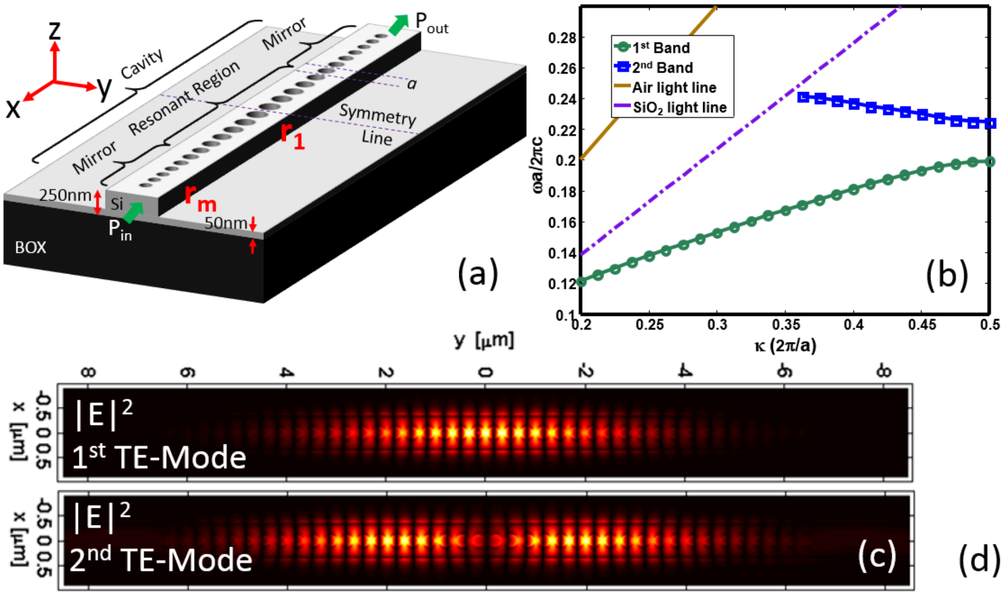

(d)

R	(nm)
r_1	130
r_2	129.8
r_3	129.4
r_4	128.7
r_5	127.7
r_6	126.4
r_7	124.8
r_8	123
r_9	120.7
r_{10}	118.3
r_{11}	115.5
r_{12}	112.5
r_{13}	109.2
r_{14}	105.6
r_{15}	101.7

Figure 44: (a) A 3D schematic of the nanobeam PhC resonator; (b) Normalized band diagram of the periodic mirror regions showing a photonic band gap in the range 181 $THz < f < 204$ THz (for $a = 330$ nm, the corresponding wavelength range is 1469 $nm < \lambda < 1656$ nm); (c) The field profiles of the first ($\lambda_1 = 1579.71$ nm) and the second ($\lambda_2 = 1609.95$ nm) TE resonant modes of the device in (a) with mode volumes of $0.97(\lambda_1/n_{si})^3$ and $1.36(\lambda_2/n_{si})^3$ respectively;(d) Tabulated air-hole radii calculated via the TL technique for the resonant region in part (a).

Given the geometrical dimensions of the substrate, the width of the waveguide is chosen at $w = 700\ nm$ to support a propagating mode in the desired wavelength range (i.e., $1469\ nm < \lambda_0 < 1656\ nm$) well below the light lines. The lattice constant is set to be $a = 330\ nm$. This choice will place the edge of the Brillouin zone (i.e., $\kappa = \pi/a$, where κ is the normalized propagation constant) far from the edge of the radiation zone (i.e., $2\pi/\lambda_0$) to reduce the radiation loss [126]. The photonic bandgap of the PhC in the mirror section is adjusted by setting the air hole radius to $r_m = 100\ nm$ to place the desired resonance wavelength at the center of the photonic gap (see Figure 44(b)). In order to maximize the radiation Q (Q_r) of the resonant region (i.e., minimize the radiation loss), the transmission line (TL) technique (detailed in [127]) is used to design the air holes in the resonant region such that the spatial profile of the resonant mode (see Figure 44(c)) meets all the requirements for low radiation loss explained in [128]. The calculated air hole radii for the resonant region are tabulated in Figure 44(d). A commercially available finite-difference-time-domain (FDTD)-based software package (i.e., Lumerical) is used to obtain the actual mode profiles as well as the estimates of the optical Qs of the resonant modes of the device shown in Figure 44(a). Figure 44(c) shows the magnitude of the electric field for the first and the second TE (electric field in the $x-y$ plane in Figure 44(a)) modes at $\lambda_1 = 1579.71\ nm$ and, $\lambda_2 = 1609.95\ nm$ (with Si refractive index $n_{si} = 3.46$). To separately estimate the Q_r and Q_w of these modes, the structure is simulated with (a) fifteen and (b) five PhC lattice periods in the mirror regions. Simulations suggest that the leakage power from the fifteen-period mirrors is negligible (i.e., $Q_w \to \infty$), and the estimated Qs of $Q_1 = Q_{r1} \approx 1.36 \times 10^6$ and $Q_2 = Q_{r2} \approx 3.77 \times 10^5$ for the first and the second modes, respectively, are mainly limited by the radiation loss (note that the material loss is neglected due to its negligible effect on Q at the selected wavelengths). Moreover, Qs of $Q_1 = Q_{w1} \approx 48000$ and $Q_2 = Q_{w2} \approx 3700$ (i.e., Q_s are limited only by the coupling loss to the input and output waveguides) are estimated for the first and the second modes, respectively, when the five-period mirrors are used. By comparing the values of Q_r and Q_w obtained for each mode, I conclude that under a practical design for achieving reasonable coupling to the input/output waveguides, the Q of each mode will not be limited by the radiation Q, and they will be defined by the coupling Q (i.e., Q_w). To complete the design of the structure, two focusing grating couplers are added on the input and output rib waveguides for out-of-plane coupling of the input and output of the overall device to the input laser and the output detector, respectively [129]. These gratings are designed using the conventional techniques and for the sole purpose of characterizing the device.

8.3 Fabrication

The PhC nanobeam resonator along with the input/output focusing grating couplers (designed to have a peak coupling efficiency at around 1600 *nm*) are fabricated on an SOI wafer with a 250 *nm* thick Si layer. A 110 *nm* layer of hydrogen silsesquioxane (6% HSQ from Dow Corning) is spin-coated on the sample as the resist, and the patterns are defined through electron-beam lithography (EBL). After developing the sample in 25% tetramethylammonium hydroxide (TMAH) at an elevated temperature of 40 °C, the device Si layer is etched with an etch-depth of 200 *nm* in an inductively-coupled-plasma (ICP) chamber. This step leaves a 50 *nm* pedestal on the sample, which is selectively removed around the grating coupler areas. The sample is then covered with 10 *nm* of silicon oxide (SiO_2) through atomic layer deposition. The metallurgical pn-junction in the middle of the nanobeam structure is formed by successive ion implantation steps to achieve concentrations of $\approx 6 \times 10^{17}\ cm^{-3}$ on the resonator region (75As+ and 49BF2+ species) and $\approx 10^{20}\ cm^{-3}$ on the contact regions. This level of doping increases the material loss in the Si layer to $\alpha = 3.35$ cm^{-1} at the telecommunication wavelength [46]. The drop in Q of the designed nanobeam resonator due to the additional material loss is estimated through the perturbation theory using the obtained mode profiles shown in Figure 44(c) [130], and the calculated values are ≈ 9000 and ≈ 3500 for the first and the second TE modes, respectively. The patterned polymethyl methacrylate (PMMA from MicroChem) resist (thickness ≈ 2 *μm*) is used as the implantation mask in all doping steps. In the next step, dopants are electrically activated by annealing the sample at 950 °C for 240 seconds in a rapid thermal processing (SSI RTP) system. For the metallization layer, titanium (as an adhesion layer) and copper are sputtered successively on another patterned layer of PMMA resist (thickness ≈ 3 *μm*) and lifted off with the aid of a sonication bath. The optical micrograph of the device along with the scanning electron micrograph (SEM) of the resonator region is shown in Figures 45(a) and 45(b), respectively. The nanobeam is connected to the feeding waveguide at both ends of the resonator.

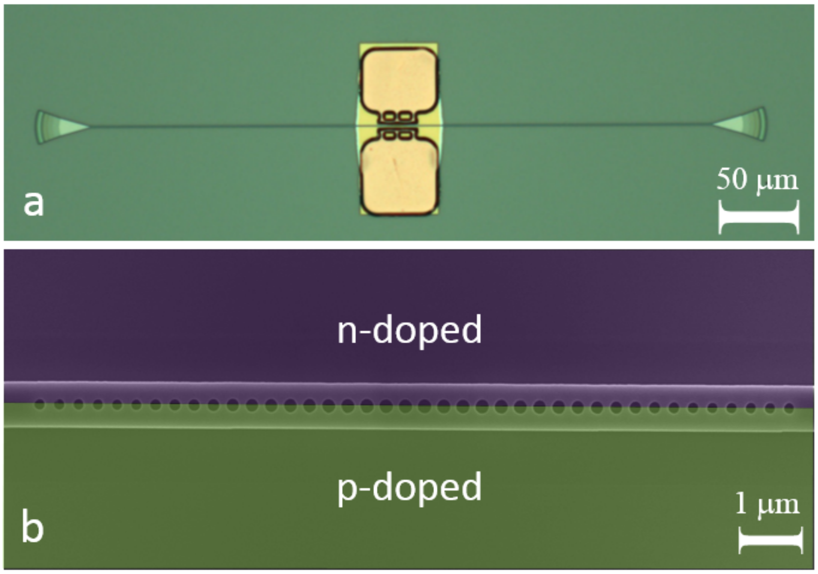

Figure 45: (a) Optical micrograph of the fabricated device showing the copper pads on a 50 *nm* thick pedestal around the PhC nanobeam resonator as well as the 400 *μm* long inline feeding waveguide along with the focusing grating couplers at the two ends. (b) False-colored SEM of the fabricated PhC nanobeam resonator (taken before metallization). The purple and green colors represent the n-type and p-type regions, respectively.

The focusing gratings at the two ends of the feeding waveguides facilitate the input/output coupling of light to/from the device. The optical field propagating inside the waveguide couples into and out of the PhC nanobeam resonator through the mirror regions at the two ends of the resonator.

8.4 Characterization

To characterize the device, the output light of a CW tunable laser (Agilent 81682A) is launched into a cleaved single mode fiber through an in-line polarization controller. The fiber is mounted on a stage equipped with XYZ micro-positioners as well as a rotation/tilt compensator. The fiber is then aligned so that its outcoming light is focused on the input grating coupler. Similarly, the output light from the chip is collected through the output grating coupler with a similar cleaved fiber and fed directly into a detector (Thorlabs PDB150C 800 $nm - 1700$ nm). The chip is placed on a temperature controlled stage with the temperature set at 25 °C. Figure 46 shows the normalized transmission spectrum of the device, which is obtained by sweeping the laser wavelength from 1510 nm to 1640 nm at the rate of 5 nm per second. To have a good signal-to-noise ratio, the output power of the laser is set to its maximum-over-sweep value, i.e., 354 μW. The measurement is repeated with the laser power set at a much lower level of 5 μW. Since the later measurement results in the same lineshape for both resonances, I conclude that the nonlinear loss sources have negligible effect on the measurement with the higher laser power, and all observed effects are due to linear phenomena. For normalization, the obtained transmission spectrum is divided to that of a reference device (fabricated on the same chip) that consists of similar grating couplers and waveguides with no PhC nanobeam resonator in the middle (with the same overall device length).

The two pronounced peaks in the collected spectrum in Figure 46 are related to the two supported resonant modes of the PhC nanobeam resonator. The first TE mode at 1598.8 *nm* features a loaded-Q (Q_L) of $\approx$ 8900. The second TE mode at 1627.3 *nm* is closer to the bandgap edge and exhibits a larger spatial extent along the resonator and consequently experiences a stronger coupling from and to the feeding waveguides (Figure 44).

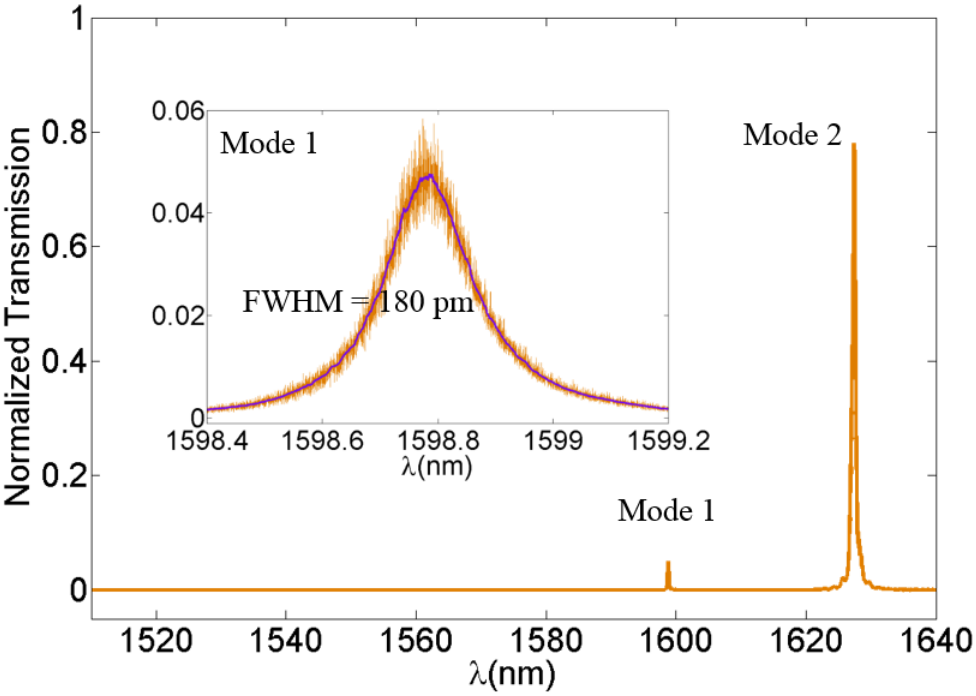

Figure 46: Normalized transmission spectrum of the PhC nanobeam resonator in Figure 45. The inset shows a closer look at the linewidth around the first mode. The designed photonic bandgap of the PhC mirrors covers the range 1469 $nm < \lambda <$ 1656 nm.

The measured Q_L for this mode is $\approx$ 3200. The actual resonance wavelengths are slightly higher than the simulated ones owing to the thin deposited silica on the sample. The measured transmission of the resonator at the first and second resonance wavelengths are 0.047 and 0.76, respectively. With the symmetric resonator-to-input/output waveguide coupling regions, the resonator transmission at resonance is given by $T(\omega_0) = (Q_L/Q_w)^2$ [130]. From this relation, the experimental Q_w values can readily be calculated to be 41000 and 3670 for the first and the second modes, respectively which are in good agreement with the predicted values from the FDTD simulations. A calibrated optical head power sensor (Agilent 81624A) is used to measure the actual power coupled into the input fiber and the power collected at the output fiber in the reference device. From such measurements, the sum of the coupling loss of the input grating coupler and the propagation loss in the feeding waveguide region is estimated to be $\zeta \approx 6.6\ dB$ at the first resonant wavelength (i.e., $1598.8\ nm$). This loss is of interest in the calculation of the optical power that enters the resonator input. The $E_c = (Q_w/\omega_0)P_{out}$ expression is then used to estimate the total stored electromagnetic energy in the resonator (E_c) for different laser output powers [130]. In this expression P_{out} is the waveguide output power (see Figure 44(a)) which is estimated by measuring the power in the output fiber of the actual device and normalizing it to the propagation losses (i.e., ζ). Plots in Figure 47 show the transmission spectrum of the device around the first resonant mode for different laser excitation powers with no reverse bias applied to the pn-junction (the corresponding resonator energies are provided in the legend). It is seen that for the applied laser power levels, the resonance wavelength and the lineshape are preserved. This observation suggests that the nonlinear absorption mechanisms are not present at zero reverse-bias.

To observe the effect of the applied reverse bias of the pn-junction device, the transmission spectrum of the device is monitored under different reverse-bias voltages, and the results are shown in Figure 47(b). In this measurement, the laser wavelength is swept from shorter to longer wavelengths. As shown in Figure 47(b), the Lorentzian lineshape of the resonance is no longer preserved for bias voltages larger than $22V$. The observed redshift in the resonance wavelength for smaller voltages (i.e., $V_r < 22V$) is attributed to the carrier dispersion property of Si, which is triggered by the depletion of the majority carriers in the p and n regions [46]. Once the applied bias voltage exceeds $22V$, the resonance linewidth becomes lopsided, and the resonance peak experiences an even bigger redshift; this is not explicable only through the carrier dispersion property of Si. As seen in Figure 47(b), the resonance lineshape in this regime broadens and features an abrupt jump on the right side (higher wavelength) of the peak. This behavior is known as the peak dragging which is directly linked to the bistability condition [131]. This characteristic can be explained by considering both the thermo-optic effect in Si ($dn_{si}/dT = 1.86 \times 10^{-4} K^{-1}$ [132]) and the Joule heating mechanism due to the induced photocurrent in the device. Once the laser wavelength reaches the vicinity of the resonance wavelength (from the left side) the optical field in the resonator generates a finite photocurrent. The associated dissipated electric power increases the device temperature, which in turn results in a small redshift in the resonance wavelength. This redshift in the resonance wavelength tends to reduce the optical field in the resonator and hence, it limits the photocurrent generation. As the laser wavelength is swept to longer wavelengths, the thermo-optic effect can no longer catch up with the Joule heating effect. Consequently, this negative feedback process turns into a positive one. The abrupt jump in the spectrum is where this condition manifests itself.

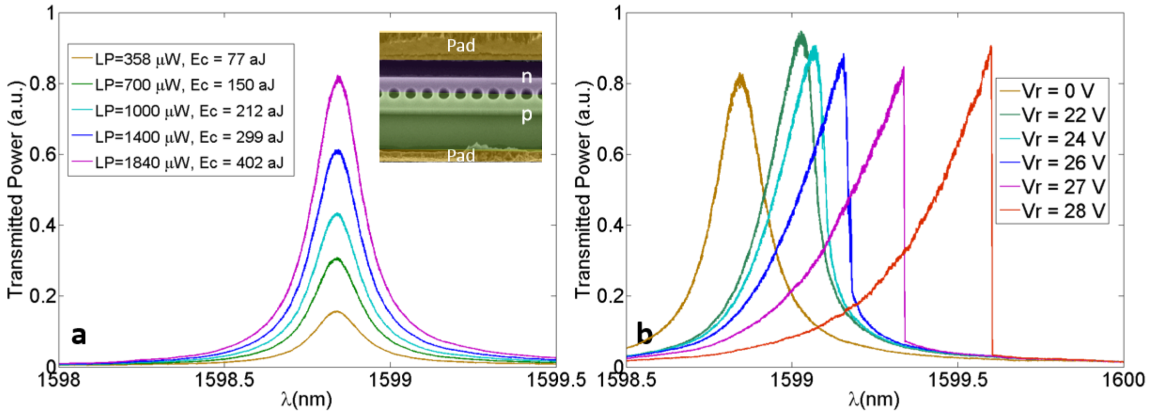

Figure 47: (a) Measured transmitted power spectrum of the nanobeam resonator at different laser output powers (PL) with the applied voltage of the pn-junction device kept fixed ($V_r = 0$), (b) Transmitted power spectrum of the nanobeam resonator at a fixed laser power ($P_L = 1.84\ mW$) with varying reverse bias applied to the pn-junction device.

I use a source measurement unit (SMU) (Keithley 4200-SCS) to measure the photocurrent generated in the pn-junction. In this experiment, the wavelength of the tunable laser is slowly swept (at a rate of 500 pm/s) from 1595 nm to 1605 nm. This range covers the first resonance wavelength of the nanobeam resonator. Different curves in Figure 48(a) show the measured leakage current of the device at various applied reverse-bias voltages as a function of the laser scanning wavelength. In this study, the output power of the laser is fixed at 1.84 mW (corresponding to 403 μW in the input waveguide).

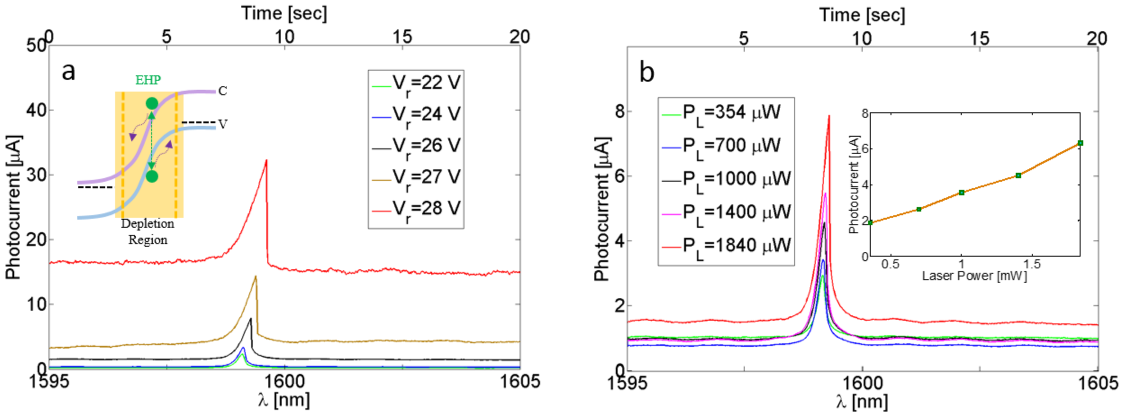

Figure 48: (a) Measured pn-junction leakage current in the resonator region as the laser wavelength is swept (the top and bottom horizontal axes are the sweeping time and the corresponding laser wavelength, respectively). In these measurements the laser power is kept fixed at $P_L = 1.84\ mW$. To clarify the speed of the wavelength sweep, the sweeping time is also shown in the figure. (b) Measured photocurrent generated for different laser powers (bias is kept fixed at $V_r = 22\ V$) as a function of the sweeping time. The inset shows the photocurrent jump versus the laser power (P_L).

As it can be clearly seen, the leakage current rises at the wavelengths closer to the resonance wavelength of the resonator because of the increased field density in the resonator. Application of higher reverse bias voltages widens the depletion region, which in turn modestly increases the photocarrier collection efficiency. In addition, the generated photocarriers experience a stronger driving force under higher electric fields. It is seen in Figure 48(a) that the generated photocurrent progressively increases from ≈ 1.9 μA to ≈ 16 μA as the reverse-bias voltage increases from 22 V

to 28 V. The leakage current (off-resonance) also rises with the reverse-bias voltage. The plots in Figure 48(b) show that the photocurrent increases in response to the successive increments in the laser power at a fixed reverse-bias voltage, i.e., $V_r = 22$ V. It is seen that by increasing the laser power from 354 μW to 1.84 mW, the photocurrent rises from ≈ 1.9 μA to ≈ 6.4 μA rather linearly (see the inset in Figure 48(b)). Combining the results in Figures 48(a) and 48(b), one can conclude that for higher optical powers, the bistability occurs at lower reverse voltages. The linear characteristic seen in the inset of Figure 48(b) suggests that the photocarriers are generated mainly through the linear absorption mechanisms. Note that the required input optical power (to achieve bistability) in the device can be reduced significantly by improving the photocarrier collection efficiency and using a resonator with higher Q.

8.5 Discussion

Although pure bulk Si has minimal linear absorption at telecommunication wavelengths, additional ion implantation, material defects, and also the mid gap surface states, e.g., at the Si-air or Si-SiO$_2$ interfaces, substantially contribute to the linear absorption of Si-based nanostructures [133, 134, 135, 136, 137]. Following the expressions in Appendix 1, the linear and nonlinear absorption rates can be estimated. Assuming a perfect collection of photocarriers, i.e., $\eta = 1$, the collective linear absorption rate is calculated to be $\gamma_L = 2.9 \times 10^{10}$ s^{-1} when the stored energy is $E_c = 402$ aJ (corresponding to 397 μW input waveguide power and the resonator Q of 8900). The TPA and FCA absorption rates are also evaluated to be $\gamma_{TPA} = 5.50 \times 10^7$ s^{-1} and $\gamma_{FCA} = 2.46 \times 10^7$ s^{-1} for the same stored energy (see Appendix 1). It is seen that the nonlinear absorption rates are much smaller than the collective linear absorption rate. This result is consistent with the experimental observations detailed in the characterization section. This confirms that the generated photocurrent in my experiments is mainly due to the linear absorption processes. It is worth noting that in principle, the photocarriers due to TPA can also contribute to the photocurrent (before non-radiative relaxation takes place). Such photocarriers can be generated in high-Q/low-mode-volume cavities at low input optical powers as shown in numerous studies [111, 112]. In such cases optical bistability can be achieved even at lower input optical powers once the structure is integrated with a similar reverse-biased pn-junction explained in the present work.

CHAPTER IX

EPILOGUE

9.1 Brief Summary of Contributions

My thesis has been mainly focused on the design, implementation, and characterization of a series of essential integrated photonic elements that are urgently needed for realization of complex integrated photonic systems on-chip using hybrid material platforms. As discussed throughout the chapters, the use of multiple heterogeneous materials can greatly enhance the optical functionality of the platform for photonic applications. The first part of my work was dedicated to the Si/SiO_2/SiN material platform. In this part, a wideband interlayer grating coupler featuring very low insertion loss for the aforementioned platform was demonstrated. The used methodology for this design is readily applicable to other types of multilayer platforms.

As the second major contribution of my research, I developed a resonance-based integrated electro-optic modulator on a multilayer material platform consisting of a stack of Si, SiO_2, and Si layers. The modulation mechanism is based on carrier accumulation on the Si layers. This device benefits from a very small footprint and exhibits modulation speeds in the 30 Gb/s range without sophisticated optimization. Up to now, this demonstrated speed is the record-high for this type of modulators. I further showed that modest optimization on the device can further increase the modulation data rate up to ≈ 60 Gb/s. This modulator can be self-trimmed up to 1 nm by applying a dc voltage (the device is capacitive and draws negligible current). This feature eliminates the need for power-hungry thermal-based trimming/tuning methods and hence, can substantially decrease the overall power consumption of the device. The demonstration of this modulator is only the first step in showing the potentials of this unique material platform, and a similar approach can be adopted for realization of other functional devices and subsystems (e.g., filters, routers, switches) with unprecedented performance and no need for power-hungry trimming techniques.

By utilizing the same Si/SiO_2/Si platform, I also demonstrated the first integrated field-programmable photonic device. This powerful yet simple-to-fabricate device allows for large-scale integration, which is compatible with the existing fabrication technology. This device opens up new possibilities for realization of functional photonic devices and systems featuring comparable functionalities to electronic FPGAs. As a simple example, I used this building block to demonstrate a field-programmable 2×2 optical switch.

Looking ahead, I also investigated the use of graphene in the hybrid material platform to address some of the shortcomings of Si and SiN, especially in achieving ultra-high speeds (beyond 100 GHz). My goal in this add-on part to my thesis was to show the unique capabilities of the graphene-based hybrid materials (rather than demonstrating the full system) to open up new areas of research in this field. For this purpose, in Chapter 6, light-matter interaction between the electrons on an atom-thick sheet of graphene and the optical field circulating in a silicon-based microdisk was explored. In the presented device, infrared light was modulated through electrostatic gating of the graphene sheet. This design is of great technological significance as it paves the way for development of chip-scale photonic devices for ultrafast electro-optical switching and modulation applications.

In the last part of my work, I demonstrated an optical bistable device in a Si-based integrated photonic platform comprising a rather low-Q photonic crystal nanobeam resonator with an embedded pn-junction. The bistable functionality of the proposed device relies on the interplay between the generated heat due to the photocurrent and the thermo-optic effect. This is in contrast to other Si-based bistable optical devices, which depend on heating through non-radiative relaxation of carriers (triggered by nonlinear TPA and FCA processes). I demonstrated that the generated photocurrent through linear absorption mechanisms is sufficient to achieve bistability. The proposed Joule-heating mechanism is particularly of interest as it permits the realization of optical bistability at comparatively low input optical powers. The proposed mechanism allows for design and implementation of all-optical processing systems and robust ultrahigh sensitive sensors at extremely low optical powers.

9.2 Future Directions

The material and device properties demonstrated in this thesis opens up several new fronts for performing cutting-edge research in the field of integrated nanophotonics. The achievable device performance in the hybrid material platforms is very encouraging for realization of integrated photonic systems for practical applications. With the goal of this research being a ground-breaking effort in demonstrating device capabilities of CMOS-compatible hybrid material platforms, there is still several possibilities to achieve higher speeds, lower power consumptions, lower operation power and more compact devices compared to the world-record performance measures demonstrated in this thesis. Some of the possibilities are as follows:

(a) It is rewarding to future optimize the geometrical dimensions of the interlayer grating coupler for better coupling efficiencies. To reduce the overall footprint of the device, the current methodology can be applied to optimize the device for shorter taper regions similar to the architecture of focusing grating couplers.

(b) The modulation depth, the insertion loss, and the power consumption of the electro-optic modulator demonstrated in this thesis can be highly enhanced. Such improvements can be achieved by using a multilayer platform featuring a higher optical quality. The use of fabrication techniques with higher precision can reduce the size of the device. Also modest optimization on the doping profiles can be beneficial both for the lower power consumption as well as the operational bandwidth. Other possibilities include the use of thin layers of high-k dielectrics (e.g., Al_2O_3) in place of SiO_2 as the buffer layer between the active Si layers of the hybrid material platform, undercutting of this oxide layer and infiltration with electro-optic polymers, and the use of graphene in place of Si.

(c) The design of the graphene-based modulator can be modified to achieve a better performance. In particular, adding a second graphene layer as the second electrode can significantly increase the operation bandwidth. Utilization of graphene layers with lower defect density and development of the transfer technique conducive to a lower residual contamination allows to take full advantage of the properties of an ideal graphene sheet. Similar to the electro-optic modulator device, the use of higher-Q microresonators (possibly on low-loss substrates such as SiN) greatly ameliorates the modulator specifications.

(d) The bistable device introduced in Chapter 8 is very promising for sensing applications. An external feedback circuit can be developed to stabilize the specifications of the device. The photonic device can also be optimized to reach bistability at considerably lower optical powers.

(e) By combining the photonic elements demonstrated in the dissertation, it is possible to develop a multi-channel modulator for dense wavelength division multiplexing (DWDM) or course wavelength division multiplexing (CWDM) applications (similar to the architecture shown in Figure 2). Each channel can support binary or other advance modulation formats such as QPSK. The demonstration of such intricate systems requires many optimization efforts at various levels, which can form interesting topic for future Ph.D. dissertations. Finally, the hybrid material platform is an excellent candidate for demonstration of the future RF-millimeter-wave/photonic information processing systems.

APPENDIX A

DRY-ETCH RECIPES

Table 4 summarizes the gas flow rates, the plasma DC bias, and the RF power used for the dry-etch process of SiN deposited through LPCVD. This recipe is used to etch photonic device in 400 *nm*-thick SiN substrates. Since ZEP is use as the mask, etch rate is measured for SiN as well as ZEP.

Table 4: Detailed parameters for LPCVD-deposited SiN.

Tool	Oxford RIE					
Gas type	CF_4	CHF_3	Ar	O_2	Cl_2	C_8F_8
Flow rate (*sccm*)	50	4	0	0	0	0
RF Power (W)	175					
DC Bias (V)	190					
Chamber pressure (Torr)	0.250					
SiN Etch Rate (nm/min)	≈ 40					
ZEP Etch Rate (nm/min)	≈ 20					

Table 5 summarizes the gas flow rates, the plasma DC bias, and the RF power used for the dry-etch process of thermally-grown SiO_2. This recipe is used to remove thin layers of thermal SiO_2 from the surface.

Table 5: Detailed parameters for thin thermally-grown SiO_2.

Tool	Oxford RIE					
Gas type	CF_4	CHF_3	Ar	O_2	Cl_2	C_8F_8
Flow rate (*sccm*)	0	24	15	0	0	0
RF Power (W)	200					
DC Bias (V)	420					
Chamber pressure (Torr)	0.035					
SiO_2 Etch Rate (nm/min)	≈ 25					

Table 6 summarizes the gas flow rates, the plasma DC bias, and the RF power used for the dry-etch process of crystalline Si. This recipe is used to etch photonic devices on Si substrates. HSQ is used as the mask. The etch rate is measured for Si, HSQ, and thermally-grown SiO_2.

Table 6: Detailed parameters for thin crystalline Si.

Tool	Plasma-therm ICP					
Gas type	CF_4	CHF_3	Ar	O_2	Cl_2	C_8F_8
Flow rate (*sccm*)	0	0	0	0	50	0
RF1 Power (W)	125					
RF2 Power (W)	75					
DC Bias (V)	460					
Chamber pressure (Torr)	-					
Si Etch Rate (*nm/min*)	$\approx 70 - 75$					
HSQ (*nm/min*)	≈ 16.8					
Thermal SiO_2 (*nm/min*)	≈ 11.6					

Table 7 summarizes the gas flow rates, the plasma DC bias, and the RF power used for dry-etch process of SiO_2 deposited through PECVD. This process is used to open up deep via holes in the PECVD SiO_2 cladding layer. In such processes, Cr can be used as a hard mask as well as an etch stop. Etch rates for SiO_2, Cr, Si, ZEP and PMMA are provided.

Table 7: Detailed parameters for thick PECVD-deposited SiO_2.

Tool	Plasma-therm ICP					
Gas type	CF_4	CHF_3	Ar	O_2	Cl_2	C_8F_8
Flow rate (*sccm*)	0	0	4	4	15	16
RF1 Power (W)	400					
RF2 Power (W)	400					
DC Bias (V)	800					
Chamber pressure (Torr)	-					
SiO_2 Etch Rate (*nm/min*)	≈ 260					
Cr (*nm/min*)	< 60					
Si (*nm/min*)	≈ 180					
ZEP (*nm/min*)	≈ 500					
PMMA (*nm/min*)	≈ 600					

APPENDIX B

TWO-PHOTON ABSORPTION AND FREE-CARRIER ABSORPTION EFFECTIVE MODE VOLUMES

The nonlinear absorption rates depend on the resonator mode profile ($E(r)$) as well as the stored energy, i.e., Ec. The TPA rate (γ_{TPA}) can be estimated through the following expressions [109]:

$$\begin{aligned}
\gamma_{TPA}(E_c) &= \Gamma_{TPA}\frac{\beta_{Si}c^2}{n_{Si}^2 V_{TPA}}E_c,\\
V_{TPA} &= \frac{\left(\int n^2(r)E^2(r)dr\right)^2}{\int n^4(r)E^4(r)dr},\\
\Gamma_{TPA} &= \frac{\int_{Si} n^4(r)E^4(r)dr}{\int n^4(r)E^4(r)dr}.
\end{aligned} \tag{31}$$

In Equation 31, $\beta_{Si} = 8.4 \times 10^{-12}\ mW^{-1}$ is the TPA coefficient of Si [8]. In Si with a reverse-biased pn-junction the effect of intrinsic free-carriers is minimal. However, the FCA due to the free carriers induced by TPA can be significant. Similarly I have the following expressions for FCA rate (γ_{FCA}) [109].

$$\begin{aligned}
\gamma_{FCA}(E_c) &= \Gamma_{FCA}\frac{\tau\sigma_{Si}\beta_{Si}c^3}{2n_{Si}^3\hbar\omega_0 V_{FCA}^2}E_c^2,\\
V_{FCA}^2 &= \frac{\left(\int n^2(r)E^2(r)dr\right)^3}{\int n^6(r)E^6(r)dr},\\
\Gamma_{FCA} &= \frac{\int_{Si} n^6(r)E^6(r)dr}{\int n^6(r)E^6(r)dr}.
\end{aligned} \tag{32}$$

In Equation 32, τ denotes the free-carrier lifetime, which strongly depends on the free-carrier density as well as the surface effects (for the purpose of my calculations, $\tau \approx 0.5 \times 10^{-9}\ s$ is assumed [110]), $\sigma_{Si} = 14.5 \times 10^{-22}\ m^2$ is the free-carrier cross section, and $\hbar\omega_0$ is the photon energy [46]. The field profiles obtained through the FDTD method are used to calculate the TPA and FCA effective mode volumes and the geometric coefficients in Equations 31 and 32 for the first resonant mode of the nanobeam resonator in Chapter 8 ($V_{FCA-M1} = 3.28(\lambda_1/n_{Si})^3$, $\Gamma_{FCA-M1} = 0.998$, $V_{TPA-M1} = 4.63(\lambda_1/n_{si})^3$, $\Gamma_{TPA-M1} = 0.992$).

REFERENCES

[1] "Cisco global cloud index: Forecast and methodology," tech. rep., 2012-2017.

[2] "The international technology roadmap for semiconductors wesite." `http://www.itrs.net/`. Accessed: 2015-04-30.

[3] A. V. Krishnamoorthy, K. W. Goossen, W. Jan, and X. Zheng, "Progress in low-power switched optical interconnects," *Selected Topics in Quantum Electronics*, vol. 17, no. 2, pp. 357–376, 2011.

[4] A. V. Krishnamoorthy, "Photonics-to-electronics integration for optical interconnects in the early 21st century," *Optoelectronics Letters*, vol. 2, no. 3, 2006.

[5] X. Zheng, J. K. Lexau, J. Bergey, J. E. Cunningham, R. Ho, R. Drost, and A. V. Krishnamoorthy, "Optical transceiver chips based on co-integration of capacitively coupled proximity interconnects and vcsels," *IEEE Photon. Tech. Lett.*, vol. 19, no. 7, pp. 453–455, 2007.

[6] D. Hopkins, A. Chow, R. Bosnyak, B. Coates, J. Ebergen, S. Fairbanks, J. Gainsley, R. Ho, J. Lexau, F. Liu, T. Ono, J. Schauer, I. Sutherland, and R. Drost, "Circuit techniques to enable 430 gb/s/mm/mm proximity communication," in *IEEE Int. Solid-State Circuits Conference*, pp. 368–369, 2007.

[7] Q. Lin, J. Zhang, G. Piredda, R. W. Boyd, P. M. Fauchet, and G. P. Agrawal, "Dispersion of silicon nonlinearities in the near infrared region," *Appl. Phys. Lett*, vol. 91, p. 021111, 2007.

[8] M. Dinu, F. Quochi, and H. Garcia, "Third-order nonlinearities in silicon at telecom wavelengths," *Appl. Phys. Lett*, vol. 82, p. 2954, 2003.

[9] K. Ikeda, R. E. Saperstein, N. Alic, and Y. Fainman, "Thermal and kerr nonlinear properties of plasma-deposited silicon nitride/ silicon dioxide waveguides," *Optics Express*, vol. 16, no. 17, p. 12987, 2008.

[10] A. Boskovic, S. V. Chernikov, J. R. Taylor, L. Gruner-Nielsen, and O. A. Levring, "Direct continuous-wave measurement of n2 in various types of telecommunication fiber at 1.55 μm," *Opt. Lett.*, vol. 21, no. 24, pp. 1966–1968, 1996.

[11] M. Borselli, T. Johnson, and O. Painter, "Beyond the rayleigh scattering limit in high-q silicon microdisks: theory and experiment," *Optics Express*, vol. 13, no. 5, pp. 1515–1530, 2005.

[12] M. Soltani, S. Yegnanarayanan, and A. Adibi, “Ultra-high q planar silicon microdisk resonators for chip-scale silicon photonics,” *Optics Express*, vol. 15, no. 8, pp. 4694–4704, 2007.

[13] J. F. Bauters, M. J. R. Heck, D. John, D. Dai, M. C. Tien, J. S. Barton, A. Leinse, R. G. Heideman, D. J. Blumenthal, and J. Bowers, “Ultra-low-loss high-aspect-ratio si3n4 waveguides,” *Optic Express*, vol. 19, no. 4, pp. 3163–3174, 2011.

[14] M.-C. Tien, J. F. Bauters, M. J. R. Heck, D. T. Spencer, D. J. Blumenthal, , and J. E. Bowers, “Ultra-high quality factor planar si3n4 ring resonators on si substrates,” *Optic Express*, vol. 19, no. 14, pp. 13551–13556, 2011.

[15] J. S. Levy, A. Gondarenko, M. A. Foster, A. C. Turner-Foster, A. L. Gaeta, and M. Lipson, “Cmos-compatible multiple-wavelength oscillator for on-chip optical interconnects,” *Nature Photonics*, vol. 4, pp. 37–40, 2010.

[16] J. D. Jackson, *Classical Electrodynamics.* John Wiley and Sons, Inc., 1998.

[17] J. B. Jager, V. Calvo, E. Delamadeleine, E. Hadji, P. No, T. Ricart, D. Bucci, and A. Morand, “High-q silica microcavities on a chip: From microtoroid to microsphere,” *Appl. Phys. Lett.*, vol. 99, no. 181123, 2011.

[18] “Laboratory for nanoscale optics.” `http://nano-optics.seas.harvard.edu/nanobeam.html`. Accessed: 2015-06-03.

[19] K. Hennessya, A. Badolatoa, P. Petroffa, and E. Hua, “Positioning photonic crystal cavities to single inas quantum dots,” *Photonics and Nanostructures - Fundamentals and Applications*, vol. 2, no. 2, pp. 65–72, 2004.

[20] E. S. Hosseini, S. Yegnanarayanan, A. H. Atabaki, M. Soltani, and A. Adibi, “Systematic design and fabrication of high-q single-mode pulley-coupled planar silicon nitride microdisk resonators at visible wavelengths,” vol. 18, no. 3, pp. 2127–2136, 2010.

[21] J. F. Bauters, M. L. Davenport, M. J. R. Heck, J. K. Doylend, A. Chen, A. W. Fang, and J. E. Bowers, “Silicon on ultra-low-loss waveguide photonic integration platform,” *Optic Express*, vol. 21, no. 1, pp. 544–555, 2013.

[22] Q. Li, A. A. Eftekhar, M. Sodagar, Z. Xia, A. H. Atabaki, and A. Adibi, “Vertical integration of high-q silicon nitride microresonators into silicon-on-insulator platform,” *Opt. Express*, vol. 21, no. 15, pp. 18236–18248, 2013.

[23] X. Zheng, J. E. Cunningham, I. Shubin, J. Simons, M. Asghari, D. Feng, H. Lei, D. Zheng, H. Liang, C. C. Kung, J. Luff, T. Sze, D. Cohen, and A. V. Krishnamoorthy, “Optical proximity communication using reflective mirrors,” *Opt. Express*, vol. 16, no. 19, pp. 15052–15058, 2008.

[24] D. C. Lee, D. Feng, C. C. Kung, J. Fong, W. Qian, X. Zheng, J. E. Cunningham, A. V. Krishnamoorthy, and M. Asghari, "Monolithic chip-to-chip wdm optical proximity coupler utilizing echelle grating multiplexer/demultiplexer integrated with micro mirrors built on soi platform," in *Photon. Soc. Summer Top. Meeting*, pp. 215–216, 2010.

[25] Y. Zhang, D. Kwong, X. Xu, A. Hosseini, S. Y. Yang, J. A. Rogers, and R. T. Chen, "On-chip intra-and inter-layer grating couplers for three-dimensional integration of silicon photonics integration of silicon photonics," *Appl. Phys. Lett*, vol. 102, no. 211109, 2013.

[26] J. Yao, I. Shubin, X. Zheng, G. Li, Y. Luo, H. Thacker, J. H. Lee, J. Bickford, K. Raj, J. E. Cunningham, and A. V. Krishnamoorthy, "Low loss optical interlayer coupling using reflector-enhanced grating couplers," in *2nd Int. Conf. Opt. Interconnects*, pp. 31–32, 2013.

[27] S. Bernab, C. Kopp, M. Volpert, J. Harduin, J. M. Fdli, and H. Ribot, "Chip-to-chip optical interconnections between stacked self-aligned soi photonic chips," *Opt. Express*, vol. 20, no. 7, pp. 7886–7894, 2012.

[28] M. Cabezn, I. Garcs, P. Kumar, A. Villafranca, J. Pozo, and A. Kamierczak, "Silicon-on-insulator chip-to-chip coupling via out-of-plane or vertical grating couplers," *Appl. Opt*, vol. 51, no. 34, pp. 8090–8094, 2012.

[29] J. H. Kang, Y. Atsumi, Y. Hayashi, J. Suzuki, Y. Kuno, T. Amemiya, N. Nishiyama, and S. Arai, "Amorphous-silicon inter-layer grating couplers with metal mirrors toward 3-d interconnection," *IEEE J. Sel. Topics Quantum Electron.*, vol. 20, no. 4, 2014.

[30] F. H. P. M. Habraken, ed., *LPCVD Silicon Nitride and Oxynitride Films: Material and Applications in Integrated Circuit Technology.* Springer, 1991.

[31] J. Cowley, *Diffraction physics.* Elsevier, 1995.

[32] D. Taillaert, P. Bienstman, and R. Baets, "Compact efficient broadband grating coupler for silicon-on-insulator waveguides," *Opt. let.*, vol. 29, no. 23, pp. 2749–2751, 2004.

[33] P. B. Johnson and R. W. Christy, "Optical constants of the noble metals," *Phys. Rev. B*, vol. 6, pp. 4370–4379, 1972.

[34] F. Kreith and M. Bohn, *Principles of heat transfer.* Harper and Row New York, 1986.

[35] D. Cahill, W. Ford, K. Goodson, G. Mahan, A. Majumdar, H. Maris, R. Merlin, and S. Phillpot, "Nanoscale thermal transport," *Journal of Applied Physics*, vol. 93, no. 793, 2003.

[36] S. T. Chu, W. Pan, S. Sato, T. Kaneko, B. E. Little, and Y. Kokubun, "Wavelength trimming of a microring resonator filter by means of a uv sensitive polymer overlay," *IEEE Photonics Technology Letters*, vol. 11, no. 6, 1999.

[37] S. Prorok, A. Y. Petrov, M. Eich, J. Luo, and A. K.-Y. Jen, "Trimming of high-q-factor silicon ring resonators by electron beam bleaching," *Optics Letters*, vol. 37, no. 15, pp. 3114–3116, 2012.

[38] C. J. Chen, J. Zheng, T. Gu, J. F. McMillan, M. Yu, G. Q. Lo, D. L. Kwong, and C. W. Wong, "Selective tuning of high-q silicon photonic crystal nanocavities via laser-assisted local oxidation," *Opt. Express*, vol. 19, no. 13, pp. 12480–12489, 2011.

[39] Y. Shen, I. B. Divliansky, D. N. Basov, and S. Mookherjea, "Electric-field-driven nano-oxidation trimming of silicon microrings and interferometers," *Opt. Lett.*, vol. 36, no. 14, pp. 2668–2670, 2011.

[40] T.-J. Wang, Y.-H. Huang, and H.-L. Chen, "Resonant-wavelength tuning of microring filters by oxygen plasma treatment," *IEEE Photonics Technology Letters*, vol. 17, no. 3, 2005.

[41] D. Barbier, M. Green, and S. J. Madden, "Waveguide fabrication for integrated optics by electron beam irradiation of silica," *IEEE Journal of Lightwave Technology*, vol. 9, no. 6, 1991.

[42] D. Zauner, J. Hiibner, K. Malone, and M. Kristensen, "Uv trimming of arrayed-waveguide grating wavelength division demultiplexers," *Electronics Letters*, vol. 34, no. 8, 1998.

[43] J. Schrauwen, D. V. Thourhout, and R. Baets, "Trimming of silicon ring resonator by electron beam induced compaction and strain," *Optics Express*, vol. 16, no. 6, pp. 3738–3743, 2008.

[44] J. Cai, Y. Ishikawa, and K. Wada, "Strain induced bandgap and refractive index variation of silicon," *Optics Express*, vol. 21, no. 6, pp. 7162–7170, 2013.

[45] P. Etchegoin, J. Kircher, and M. Cardona, "Elasto-optical constants of si," *Physical Review B*, vol. 47, no. 16, p. 10292, 1993.

[46] R. Soref and B. Bennett, "Electrooptical effects in silicon," *IEEE J. Quantum Electron.*, vol. 23, no. 1, pp. 123–129, 1987.

[47] Q. Xu, B. Schmidt, S. Pradhan, and M. Lipson, "Micrometre-scale silicon electro-optic modulator," *Nature*, vol. 435, pp. 325–327, 2005.

[48] D. J. Thomson, F. Y. Gardes, J.-M. Fedeli, S. Zlatanovic, Y. Hu, B. P. P. Kuo, E. Myslivets, N. Alic, S. Radic, G. Z. Mashanovich, and G. T. Reed, "50-gb/s silicon optical modulator," *Ieee Photonics Technology Letters*, vol. 24, no. 4, 2012.

[49] A. Liu, R. Jones, L. Liao, D. Samara-Rubio, D. Rubin, O. Cohen, R. Nicolaescu, and M. Paniccia, "A high-speed silicon optical modulator based on a metal-oxide-semiconductor capacitor," *Nature*, vol. 427, no. 6975, p. 615618, 2004.

[50] J. V. Campenhout, M. Pantouvaki, P. Verheyen, S. Selvaraja, G. Lepage, H. Yu, W. Lee, J. Wouters, D. Goossens, M. Moelants, W. Bogaerts, and P. Absil, "Low-voltage, low-loss, multi-gb/s silicon micro-ring modulator based on a mos capacitor," in *Optical Fiber Communication Conference, OSA Technical Digest (Optical Society of America)*, 2012.

[51] C. A. Barrios, V. R. Almeida, R. Panepucci, and M. Lipson, "Electrooptic modulation of silicon-on-insulator submicrometer-size waveguide devices," *J. Lightwave Technol.*, vol. 21, no. 10, pp. 2332–2339, 2003.

[52] F. Gardes, G. Reed, N. Emerson, and C. Png, "A sub-micron depletion-type photonic modulator in silicon on insulator," *Opt. Express*, vol. 13, no. 22, pp. 8845–8854, 2005.

[53] E. Timurdogan, C. M. Sorace-Agaskar, J. Sun, E. S. Hosseini, A. Biberman, and M. R. Watts, "An ultralow power athermal silicon modulator," *Nature Communication*, vol. 5, no. 4008, 2014.

[54] H. Moradinejad, A. H. Atabaki, A. H. Hosseinnia, A. A. Eftekhar, and A. Adibi, "Double-layer crystalline silicon on insulator material platform for integrated photonic applications," *IEEE Photonics Journal*, vol. 6, no. 6, 2014.

[55] M. Sodagar, R. Pourabolghasem, A. A. Eftekhar, and A. Adibi, "High-efficiency and wideband interlayer grating couplers in multilayer si/sio2/sin platform for 3d integration of optical functionalities," *Opt. Express*, vol. 22, no. 14, pp. 16767–16777, 2014.

[56] M. Sodagar, A. H. Hosseinnia, H. Moradinejad, A. H. Atabaki, A. A. Eftekhar, and A. Adibi, "Field-programmable optical devices based on resonance elimination," *Opt. Lett.*, vol. 39, no. 15, pp. 4545–4548, 2014.

[57] A. H. Atabaki, A. A. Eftekhar, M. Askari, and A. Adibi, "Accurate post-fabrication trimming of ultra-compact resonators on silicon," *Opt. Express*, vol. 21, no. 12, pp. 14139–14145, 2013.

[58] D. G. Rabus, M. Hamacher, U. Troppenz, and H. Heidrich, "High-q channel-dropping filters using ring resonators with integrated soas," *Ieee Photonisc Technology Letters*, vol. 14, no. 10, p. 2002, 2002.

[59] S. J. Choi, Z. Peng, Q. Yang, S. J. Choi, and P. Dapkus, "tunable microdisk resonator vertically coupled to bus waveguide using epitaxial regrowth and wafer bonding," *Applied Physics Letters*, vol. 84, no. 651, 2004.

[60] M. Sodagar, A. H. Hosseinnia, A. A. Eftekhar, and A. Adibi, "Multilayer platform for low-power/passive configurable photonic device," in *CLEO: OSA Technical Digest (online) (Optical Society of America)*, 2014.

[61] P. Dong, S. Liao, D. Feng, H. Liang, D. Zheng, R. Shafiiha, C.-C. Kung, W. Qian, G. Li, X. Zheng, A. V. Krishnamoorthy, and M. Asghari, "Low vpp, ultralow-energy, compact, high-speed silicon electro-optic modulator," *Optics Express*, vol. 17, no. 25, pp. 22484–22490, 2009.

[62] W. D. Sacher and J. K. S. Poon, "Dynamics of microring resonator modulators," *Optics Express*, vol. 16, no. 20, pp. 15741–15753, 2008.

[63] D. A. B. Miller, "Energy consumption in optical modulators for interconnects," *Opt. Express*, vol. 20, no. S2, pp. A293–A308, 2012.

[64] T. N. Theis and P. M. Solomon, "In quest of the next switch: prospects for greatly reduced power dissipation in a successor to the silicon field-effect transistor," in *Proc. IEEE*, vol. 98, 2010.

[65] U. Gsele and Q. Y. Tong, "Semiconductor wafer bonding," *Annu. Rev. Mater. Sci.*, vol. 28, pp. 215–241, 1998.

[66] H. Moradinejad, A. H. Atabaki, A. H. Hosseinia, A. A. Eftekhar, and A. Adibi, "High-q resonators on double-layer soi platform," in *IEEE Photonics Conference (IPC)*, pp. 430–431, 2013.

[67] B. G. Streetman and S. Banerjee, *Solid State Electronic Devices.* Prentice Hall, Inc., 2000.

[68] J.-H. Chen, C. Jang, S. Xiao, M. Ishigami, and M. S. Fuhrer, "Intrinsic and extrinsic performance limits of graphene devices on sio2," *Nature Nanotechnology*, vol. 3, pp. 206–209, 2008.

[69] S. V. Morozov, K. S. Novoselov, M. I. Katsnelson, F. Schedin, D. C. Elias, J. A. Jaszczak, and A. K. Geim, "Giant intrinsic carrier mobilities in graphene and its bilayer," *Phys. Rev. Lett.*, vol. 100, no. 016602, 2008.

[70] K. Bolotin, K. Sikes, Z. Jiang, M. Klima, G. Fudenberg, J. Hone, P. Kim, and H. Stormer, "Ultrahigh electron mobility in suspended graphene," *Solid State Communications*, vol. 146, no. 9, pp. 351–355, 2008.

[71] G. Pirruccio, L. M. Moreno, G. Lozano, and J. G. Rivas, "Coherent and broadband enhanced optical absorption in graphene," *ACS Nano*, vol. 7, no. 6, pp. 4810–4817, 2013.

[72] K. Tsakmakidis, "Coherent absorption in graphene," *Nature Materials*, vol. 12, no. 688, 2013.

[73] X. Gan, R.-J. Shiue, Y. Gao, K. F. Mak, X. Yao, L. Li, A. Szep, D. Walker, J. Hone, T. F. Heinz, and D. Englund, "High-contrast electrooptic modulation of a photonic crystal nanocavity by electrical gating of graphene," *Nano Lett.*, vol. 13, no. 2, pp. 691–696, 2013.

[74] A. Majumdar, J. Kim, J. Vuckovic, and F. Wang, "Electrical control of silicon photonic crystal cavity by graphene," *Nano Lett.*, vol. 13, no. 2, pp. 515–518, 2013.

[75] S. A. Mikhailov and K. Ziegler, "New electromagnetic mode in graphene," *Phys. Rev. Lett.*, vol. 99, no. 016803, 2007.

[76] E. V. Castro, H. Ochoa, M. I. Katsnelson, R. V. Gorbachev, D. C. Elias, K. S. Novoselov, A. K. Geim, and F. Guinea, "Limits on charge carrier mobility in suspended graphene due to flexural phonons," *Phys. Rev. Lett.*, vol. 105, no. 266601, 2010.

[77] M. Katsnelson and A. Geim, "Electron scattering on microscopic corrugations in graphene," *Phil. Trans. R. Soc. A*, vol. 366, no. 1863, 2008.

[78] J. C. Meyer, A. K. Geim, M. I. Katsnelson, K. S. Novoselov, T. J. Booth, and S. Roth, "The structure of suspended graphene sheets," *Nature*, vol. 446, no. 60, 2007.

[79] F. Schedin, A. K. Geim, S. V. Morozov, E. W. Hill, P. Blake, M. I. Katsnelson, and K. S. Novoselov, "Detection of individual gas molecules adsorbed on graphene," *Nature Mater.*, vol. 6, no. 652, 2007.

[80] T. O. Wehling, K. S. Novoselov, S. V. Morozov, E. E. Vdovin, M. I. Katsnelson, A. K. Geim, and A. I. Lichtenstein, "Molecular doping of graphene," *Nano Lett.*, vol. 8, no. 1, pp. 173–177, 2008.

[81] M. Auslender and M. I. Katsnelson, "Generalized kinetic equations for charge carriers in graphene," *Physical Review B*, vol. 76, no. 235425, 2007.

[82] M. I. Katsnelson, "Scattering of electrons in graphene by clusters of impurities," *Physical Review B*, vol. 79, no. 195426, 2009.

[83] K. M. McCreary, K. Pi, A. G. Swartz, W. Han, W. Bao, C. N. Lau, F. Guinea, M. I. Katsnelson, and R. K. Kawakami, "Effect of cluster formation on graphene mobility," *Physical Review B*, vol. 81, no. 115453, 2010.

[84] M. Caragiu and S. Finberg, "Alkali metal adsorption on graphite: a review," *Journal of Physics: Condensed Matter*, vol. 17, no. 35, 2005.

[85] T. O. Wehling, S. Yuan, A. I. Lichtenstein, A. K. Geim, , and M. I. Katsnelson, "Resonant scattering by realistic impurities in graphene," *Phys. Rev. Lett.*, vol. 105, no. 056802, 2010.

[86] S. Yuan, H. D. Raedt, and M. I. Katsnelson, “Modeling electronic structure and transport properties of graphene with resonant scattering centers,” *Physical Review B*, vol. 82, no. 115448, 2010.

[87] M. I. Katsnelson, “Scattering of charge carriers by point defects in bilayer graphene,” *Physical Review B*, vol. 76, no. 073411, 2007.

[88] “Material-advanced chemicals supplier.” `http://www.acsmaterial.com/`. Accessed: 2015-05-30.

[89] A. C. Ferrari, J. C. Meyer, V. Scardaci, C. Casiraghi, M. Lazzeri, F. Mauri, S. Piscanec, D. Jiang, K. S. Novoselov, S. Roth, and A. K. Geim, “Raman spectrum of graphene and graphene layers,” *Rev. Lett.*, vol. 97, no. 187401, 2006.

[90] A. Gupta, G. Chen, P. Joshi, S. Tadigadapa, and P. Eklund, “Raman scattering from high-frequency phonons in supported n-graphene layer films,” *Nano. Lett.*, vol. 6, no. 12, pp. 2667–2673, 2006.

[91] P. Lespade and A. Marchand, “Caracterisation de materiaux carbones par microspectrometrie raman,” *Carbon*, vol. 22, no. 4, pp. 375–385, 1984.

[92] Z. Ni, Y. Wang, T. Yu, and Z. Shen, “Raman spectroscopy and imaging of graphene,” *Phys. Rev. B*, vol. 77, no. 235403, 2008.

[93] M. Lafkioti, B. Krauss, T. Lohmann, U. Zschieschang, H. Klauk, K. v. Klitzing, and J. H. Smet, “Graphene on a hydrophobic substrate: Doping reduction and hysteresis suppression under ambient conditions,” *Nano Lett.*, vol. 10, no. 4, pp. 1149–1153, 2010.

[94] G. Kalon, Y. J. Shin, V. G. Truong, A. Kalitsov, and H. Yang, “The role of charge traps in inducing hysteresis: Capacitance-voltage measurements on top gated bilayer graphene,” *Applied Physics Letters*, vol. 99, no. 8, 2011.

[95] S. Ibrahim, N. K. Fontaine, S. S. Djordjevic, B. Guan, T. Su, S. Cheung, R. P. Scott, A. T. Pomerene, L. L. Seaford, C. M. Hill, S. Danziger, Z. Ding, K. Okamoto, and S. J. B. Yoo, “Demonstration of a fast-reconfigurable silicon cmos optical lattice filter,” *Optics Express*, vol. 19, no. 14, pp. 13245–13256, 2011.

[96] H.-Y. Ng, M. R. Wang, D. Li, X. Wang, J. Martinez, R. R. Panepucci, and K. Pathak, “1 × 4 wavelength recongurable photonic switch using thermally tuned microring resonators fabricated on silicon substrate,” *IEEE PTL*, vol. 19, no. 9, 2007.

[97] B. G. Lee, A. Biberman, J. Chan, and K. Bergman, “High-performance modulators and switches for silicon photonic networks-on-chip,” *IEEE J. Sel. Topics Quantum Electron.*, vol. 16, no. 1, p. 622, 2010.

[98] B. G. Lee, A. Biberman, N. Sherwood-Droz, C. B. Poitras, M. Lipson, and K. Bergman, "High-speed 2 × 2 switch for multiwavelength silicon-photonic networkson-chip," *J. Lightw. Technol.*, vol. 27, no. 14, pp. 2900–2907, 2009.

[99] P. Dong, S. F. Preble, and M. Lipson, "All-optical compact silicon comb switch," *Opt. Express*, vol. 15, no. 15, pp. 9600–9605, 2007.

[100] A. Biberman, H. L. R. Lira, K. Padmaraju, N. Ophir, J. Chan, M. Lipson, and K. Bergman, "Broadband silicon photonic electrooptic switch for photonic interconnection networks," *EEE Photon. Technol. Lett.*, vol. 23, no. 8, pp. 504–506, 2011.

[101] C. Pollock and M. Lipson, *Integrated Photonics.* Springer, 2004.

[102] H. Lee, N. J. Smith, C. G. Pantano, E. Furman, and M. T. Lanagan, "Dielectric breakdown of thinned baoal2o3b2o3sio2 glass," *J. Am. Ceram. Soc.*, vol. 93, no. 2346, 2010.

[103] J. S. Suehle and P. Chaparala, "Low electric field breakdown of thin sio2 films under static and dynamic stress," *IEEE Tronsaclions on Eleclron Devices*, vol. 44, pp. 801–808, 1997.

[104] J. Verweij and J. Klootwijk, "Dielectric breakdown i: A review of oxide breakdown," *Microelectronics Journal*, vol. 27, no. 7, pp. 611–622, 1996.

[105] A. E. Willner, S. Khaleghi, M. R. Chitgarha, and O. F. Yilmaz, "All-optical signal processing," *J. Lightw. Technol.*, vol. 32, no. 4, pp. 660–680, 2014.

[106] M. Dinu, F. Quochi, and H. Garcia, "Third-order nonlinearities in silicon at telecom wavelengths," *Appl. Phys. Lett.*, vol. 82, pp. 2954–2956, 2003.

[107] K. Ikeda, R. E. Saperstein, N. Alic, and Y. Fainman, "Thermal and kerr nonlinear properties of plasma-deposited silicon nitride/silicon dioxide waveguides," *Opt. Express*, vol. 16, no. 17, pp. 12987–12994, 2008.

[108] M. Soltani, S. Yegnanarayanan, Q. Li, A. A. Eftekhar, and A. Adibi, "Self-sustained gigahertz electronic oscillations in ultrahigh-q photonic microresonators," *Phys. Rev. A*, vol. 85, no. 053819, 2012.

[109] P. E. Barclay, K. Srinivasan, , and O. Painter, "Nonlinear response of silicon photonic crystal microresonators excited via an integrated waveguide and fiber taper," *Opt. Express*, vol. 13, no. 3, pp. 801–820, 2005.

[110] V. R. Almeida and M. Lipson, "Optical bistability on a silicon chip," *Opt. Lett.*, vol. 29, no. 20, pp. 2387–2389, 2004.

[111] L. D. Haret, T. Tanabe, E. Kuramochi, and M. Notomi, "Extremely low power optical bistability in silicon demonstrated using 1d photonic crystal nanocavity," *Opt. Express*, vol. 17, no. 23, pp. 21108–21117, 2009.

[112] M. Notomi, A. Shinya, S. Mitsugi, G. Kira, E. Kuramochi, and T. Tanabe, "Optical bistable switching action of si high-q photonic-crystal nanocavities," *Opt. Express*, vol. 13, no. 7, pp. 2678–2687, 2005.

[113] L. Jin, X. Fu, B. Yang, Y. Shi, and D. Dai, "Optical bistability in a high-q racetrack resonator based on small su-8 ridge waveguides," *Opt. Lett.*, vol. 38, no. 12, pp. 2134–2136, 2013.

[114] Q. Quan, I. B. Burgess, S. K. Y. Tang, D. L. Floyd, and M. Loncar, "High-q, low index-contrast polymeric photonic crystal nanobeam cavities," *Opt. Express*, vol. 19, no. 22, pp. 22191–22197, 2011.

[115] F. Ramiro-Manzano, N. Prtljaga, L. Pavesi, G. Pucker, and M. Ghulinyan, "Thermo-optical bistability with si nanocrystals in a whispering gallery mode resonator," *Opt. Lett.*, vol. 38, no. 18, pp. 3562–3565, 2013.

[116] T. Gu, M. Yu, D. L. Kwong, and C. W. Wong, "Molecular-absorption-induced thermal bistability in pecvd silicon nitride microring resonators," *Opt. Express*, vol. 22, no. 15, pp. 18412–18420, 2014.

[117] H. Crew, *General Physics: An Elementary Text-book for Colleges.* Macmillan Company, 1910.

[118] A. W. Poon, "wo-photon absorption photocurrent in p-i-n diode embedded silicon microdisk resonators," *Appl. Phys. Lett.*, vol. 96, no. 191106, 2010.

[119] R. Hayakawa, N. Ishikura, H. C. Nguyen, and T. Baba, "Two-photon-absorption photodiodes in si photonic-crystal slow-light waveguides," *Appl. Phys. Lett.*, vol. 102, no. 031114, 2013.

[120] Z. Yong, X. Chao, W. W. Jun, Z. Qiang, H. Y. Lei, Y. J. Yi, W. M. Hua, and J. X. Qing, "Photocurrent effect in reverse-biased p-n silicon waveguides in communication bands," *Chin. Phys. Lett.*, vol. 28, no. 7, p. 074216, 2011.

[121] H. Chen, X. Luo, and A. W. Poon, "Cavity-enhanced photocurrent generation by 1.55 μm wavelengths linear absorption in a p-i-n diode embedded silicon microring resonator," *Appl. Phys. Lett.*, vol. 95, no. 171111, 2009.

[122] Q. Quan, F. Vollmer, I. B. Burgess, P. B. Deotare, I. Frank, S. Tang, R. Illic, and M. Loncar, "Ultrasensitive on-chip photonic crystal nanobeam sensor using optical bistability," in *CLEO: Laser Applications to Photonic Applications, OSA Technical Digest (CD) (Optical Society of America)*, 2011.

[123] A. P. Gonzalez-Marcos, A. Hurtado, and J. Martin-Pereda, "Optical bistable devices as sensing elements," in *Proc. SPIE*, pp. 63–70, 2004.

[124] M. F. Yanik and S. Fan, "All-optical transistor action with bistable switching in a photonic crystal cross-waveguide geometry," *Opt. Lett.*, vol. 28, no. 24, pp. 2506–2508, 2003.

[125] T. Tanabe, M. Notomi, S. Mitsugi, A. Shinya, and E. Kuramochi, "Fast bistable all-optical switch and memory on a silicon photonic crystal on-chip," *Opt. Lett.*, vol. 30, no. 19, pp. 2575–2577, 2005.

[126] Q. Quan and M. Loncar, "Deterministic design of wavelength scale, ultra-high q photonic crystal nanobeam cavities," *Opt. Express*, vol. 19, no. 19, pp. 18529–18542, 2011.

[127] M. Miri, M. Sodagar, K. Mehrany, A. A. Eftekhar, A. Adibi, and B. Rashidian, "Design and fabrication of photonic crystal nano-beam resonator: transmission line model," *J. Lightw. Technol.*, vol. 32, no. 1, pp. 91–98, 2014.

[128] K. Srinivasan and O. Painter, "Momentum space design of high-q photonic crystal optical cavities," *Opt. Express*, vol. 10, no. 15, pp. 670–684, 2002.

[129] F. V. Laere, T. Claes, J. Schrauwen, S. Scheerlinck, W. Bogaerts, D. Taillaert, L. OFaolain, D. V. Thourhout, and R. Baets, "Compact focusing grating couplers for silicon-on-insulator integrated circuits," *IEEE Photon. Technol. Lett.*, vol. 19, no. 23, p. 1919, 2007.

[130] J. D. Joannopoulos, S. G. Johnson, J. N. Winn, and R. D. Meade, *Photonic crystals: molding the flow of light.* 2008.

[131] E. Abraham and S. D. Smith, "Optical bistability and related devices," *Rep. Prog. Phys.*, vol. 45, 1982.

[132] G. Cocorullo and I. Rendina, "Thermo-optical modulation at 1.5 μm in silicon etalon," *Electron. Lett.*, vol. 28, no. 1, pp. 83–85.

[133] A. J. Reddy, J. V. Chan, T. A. Burr, R. Mo, C. P. Wade, C. E. D. Chidsey, J. Michel, and L. C. Kimerling, "Defect states at silicon surfaces," *Phys. B*, vol. 273, pp. 468–472, 1999.

[134] M. Borselli, T. J. Johnson, and O. Painter, "Accurate measurement of scattering and absorption loss in microphotonic devices," *Opt. Lett.*, vol. 32, no. 20, pp. 2954–2956, 2007.

[135] M. Borselli, T. J. Johnson, C. P. Michael, M. D. Henry, and O. Painter, "Surface encapsulation for low-loss silicon photonics," *Appl. Phys. Lett.*, vol. 91, no. 131117, 2007.

[136] M. Borselli, T. J. Johnson, and O. Painter, "Measuring the role of surface chemistry in silicon microphotonics," *Appl. Phys. Lett.*, vol. 88, no. 131114, 2006.

[137] T. Baehr-Jones, M. Hochberg, and A. Scherer, "Photodetection in silicon beyond the band edge with surface states," *Opt. Express*, vol. 16, no. 3, pp. 1659–1668, 2008.